Universidade de Aveiro
Ano 2019-2020

Departamento de Química

DANIEL ANTÓNIO CUNHA PEREIRA

UM ESTUDO INTEGRADO DAS INTERFACES DE INTERAÇÃO DA PROTEÍNA ADAPTADORA 2 EM SISTEMAS BASEADOS EM BIOMEMBRANAS

AN INTEGRATED STUDY OF ADAPTOR PROTEIN 2 INTERACTION INTERFACES IN BIOINSPIRED MEMBRANE-BASED SYSTEMS

Universidade de Aveiro
Ano 2019-2020

Departamento de Química

DANIEL ANTÓNIO CUNHA PEREIRA

UM ESTUDO INTEGRADO DAS INTERFACES DE INTERAÇÃO DA PROTEÍNA ADAPTADORA 2 EM SISTEMAS BASEADOS EM BIOMEMBRANAS

AN INTEGRATED STUDY OF ADAPTOR PROTEIN 2 INTERACTION INTERFACES IN BIOINSPIRED MEMBRANE-BASED SYSTEMS

Dissertação apresentada à Universidade de Aveiro para cumprimento dos requisitos necessários à obtenção do grau de Mestre em Bioquímica, realizada sob a orientação científica do Doutor Ildefonso Marín Montesinos, Investigador em CICECO – Instituto de Materiais de Aveiro, Departamento de Química da Universidade de Aveiro e coorientação científica do Doutor Armando Maestro, Investigador e co-responsável pelo reflectómetro *FIGARO* em Large Scale Structures Group, Instituto Laue-Langevin, Grenoble - França.

Ever tried. Ever failed. No matter. Try again. Fail again. Fail better.

- SAMUEL BECKETT

o júri

presidente

Professor Doutor Francisco Amado
Professor Associado com Agregação do Departamento de Química da Universidade de Aveiro

Doutor Ildefonso Marín Montesinos
Investigador Doutorado do grupo CICECO–Instituto de Materiais de Aveiro da Universidade de Aveiro

Professor Doutor Eduardo Guzmán Solís
Professor Auxiliar do Departamento de Química Física da Universidad Complutense de Madrid

acknowledgments

One year has passed and now it is time to thank everybody that, directly or indirectly, contributed to the success of this work.

First, I would like to thank my dear friend Carlos Bornes who has introduced me to this project and the possibility to work abroad. Without you, perhaps, none of this would come together. I am very grateful for all the help and advice during these months.

Next, I would like to thank my supervisors:

To Dr. Ildefonso Marín Montesinos, I would like to thank for all the ceaseless support, all the scientific discussions, all the teaching and guidance. Thanks to you I was able to visit two countries, France and Germany, enhance my knowledge and expertise, create a network of scientific contacts and develop myself into a better scientist. You provided me with all the tools necessary to carry with this work, always keeping a close relationship as a mentor and friend.

To Dr. Armando Maestro, I would like to express my sincere gratitude for welcoming me in a foreign country and introducing me to a whole new field which I was not acquainted. I am grateful for all the guidance provided, for the willingness to hear and discuss new ideas and for the opportunity to explore my own ideas. Your passion for science is truly polarizing and kept me motivated during these moths.

I would like to thank also to Javier and Andreas for welcoming me in Institut Laue-Langevin and introducing me to the beautiful city of Grenoble. Both of you were much more than office mates or lab partners. You were close friends that helped me feel like if I was at home, always available to help in any sort of way. Without both of you, this experience would not have been the same. And for that, I am truly thankful!

I would like to thank Dr. Luís Mafra for all the discussions and advice provided during this work. Undoubtedly, your contributions were essential to improve the quality of this work.

Finally, but not least important, I would like to thank my parents, sister, girlfriend and friends. All of you were a key aspect of the success of this work. Your amazing support and kind words kept me going during all these months, especially when I was far from home.

This work has been a shared effort and I can only thank everybody that cross paths with me during this journey.

It was, truly, an amazing experience!

My sincere thank you !

palavras-chave

Endocitose mediada por clatrina, proteína adaptadora 2, PIP2, TGN38, CD4, biomiméticos de membrana, abordagem baseada em várias técnicas , QCM-D

resumo

A endocitose desempenha um papel central em muitos processos essenciais para a vida celular, incluindo a captação de nutrientes, sinalização celular e transporte membranar. Processos endocíticos disfuncionais estão associados a condições fisiopatológicas como a doença de Alzheimer, cancro e infeções virais. A endocitose mediada pela clatrina (CME) é a principal via endocítica para a incorporação de uma vasta gama de moléculas. Embora muitos aspetos da CME sejam bem compreendidos e estudados, algumas questões ainda precisam de ser abordadas e exploradas em maior detalhe. Este trabalho teve como objetivo estudar as etapas iniciais da CME, particularmente a triagem e seleção das moléculas carga, e a ancoragem da proteína adaptadora 2 (AP2) na membrana plasmática. Neste sentido, foi implementada uma abordagem simplista onde o sistema foi reduzido aos seus componentes fundamentais: membrana lipídicas enriquecidas em PIP2, AP2 e moléculas carga (TGN38 e CD4). Para caracterizar completamente este sistema, é proposta uma abordagem baseada em várias técnicas, que inclui RMN de estado sólido e técnicas sensíveis a superfícies.

Neste trabalho, diferentes sistemas miméticos de biomembranas foram produzidos e caracterizados por elipsometria, dispersão de neutrões a pequeno ângulo (SANS) e microbalança de cristal de quartzo com monitorização da dissipação (QCM-D). As contribuições viscoelásticas da incorporação dos vários pontos de ancoragem na bicamada lipídica suportada (SLB) foram monitorizadas por QCM-D e mostraram efeitos reduzidos para PIP2, enquanto que os efeitos observados para a incorporação das moléculas carga foram bastante mais pronunciados. Os resultados apresentados nesta dissertação revelaram que a proteína AP2 se consegue ligar a SLBs funcionalizadas com moléculas carga, tanto TGN38 como CD4, na ausência de lípidos PIP2. Estas observações sugerem que AP2 pode ter diferentes mecanismos de ancoragem de acordo com os pontos de ligação disponíveis na superfície da membrana.

keywords

Clathrin-mediated endocytosis, adaptor protein 2, PIP2, TGN38, CD4, membrane biomimetics, multi-technique based-approach, QCM-D

abstract

Endocytosis plays a central role in many essential processes for the cell life, including uptake of nutrients, cell signaling and membrane trafficking. Dysfunctional endocytic processes are linked to some physiopathological conditions like Alzheimer's disease, cancer and viral infections. Clathrin-mediated endocytosis (CME) is the main endocytic pathway for the incorporation of a wide variety of molecules. Although many aspects of CME are well understood, some questions still need to be addressed and further explored. This research aimed to provide insight into the early steps of CME pathways, particularly, the sorting and cargo selection, and anchoring of adaptor protein 2 (AP2) into the membrane. To achieve this a simplistic approach was implemented, where the system was reduced into its most fundamental components: PIP2-enriched membranes, AP2 and cargo molecules (TGN38 and CD4). To fully characterize the system a multi-technique based-approach comprising solid-state NMR and surface-sensitive techniques is proposed.

In this work, different membrane biomimetic systems were produced and characterized by ellipsometry, small-angle neutron scattering (SANS) and quartz crystal microbalance with dissipation monitoring (QCM-D). The viscoelastic contributions of the incorporation of the different anchoring points into the supported lipid bilayer (SLB) were monitored by QCM-D and shown tender effects for PIP2, while more pronounced effects were observed for the incorporation of cargo molecules. New results presented in this work revealed that AP2 could bind into SLBs functionalized with cargo molecules, both TGN38 and CD4, in the absence of PIP2 lipids. These observations suggest that AP2 might have different binding mechanisms according to the anchoring points available at the surface of the membrane.

List of Contents

List of Figures

List of Tables

List of Abbreviations

AFM	Atomic force microscopy
AOI	Angle of incidence
APP	Amyloid precursor protein
AP2	Adaptor protein 2
CCP	Clathrin coated pit
CCV	Clathrin coated vesicles
CME	Clathrin-mediated endocytosis
DLS	Dynamic light scattering
DOPC	1,2-dioleoyl-sn-glycero-3-phosphocholine
DOPE	1,2-dioleoyl-sn-glycero-3-phosphoethanolamine
DPPC	1,2-dipalmitoyl-sn-glycero-3-phosphocholine
DPPE	1,2-dipalmitoyl-sn-glycero-3-phosphoethanolamine
GUV	Giant unilamellar vesicle
LB	Langmuir-Blodgett deposition
LS	Langmuir-Schaefer deposition
LUV	Large unilamellar vesicle
MLV	Multilamellar vesicle
PdI	Polydispersity index
PI(3,4)P2	Phosphatidylinositol 3,4-bisphosphate
PI(4,5)P2	Phosphatidylinositol 4,5-bisphosphate
PIP2	Phosphatidylinositol 4,5-bisphosphate
QCM	Quartz crystal microbalance
QCM-D	Quartz crystal microbalance with dissipation monitoring
SANS	Small-angle neutron scattering
SAXS	Small-angle x-ray scattering
SLB	Supported lipid bilayer
ssNMR	Solid-state nuclear magnetic resonance
SUV	Small unilamellar vesicle
UV	Unilamellar vesicle

1

Motivation and Objectives

1. Motivation and Objectives

1.1. Motivation to investigate the endocytosis processes

Cells contain plasmatic membranes that are semi-permeable, allowing the diffusion of specific compounds, *i.e.* small molecules and ions, through them. Nevertheless, this diffusion movement from the extracellular domain into the cytoplasmatic domain is only possible to small molecules. In the case of larger and bulky materials, such as hormones, nutrients, proteins, even full cells and microorganisms, cells use *bulk transport mechanisms* [1,2]. In eukaryotes, the bulk transport mechanisms are comprised by endocytosis and exocytosis.

Endocytosis plays a central role in many essential processes for the cell life. Endocytic internalization pathways are organized into three main categories: phagocytosis, pinocytosis and receptor-mediated endocytosis [1,2]. Even though each of these types of endocytosis has slight differences, all of them share a common trait where the plasma membrane of the cell invaginates the target ligand-molecule undergoing internalization by formation of a lipid vesicle around it [1].

Clathrin-mediated endocytosis (CME), a type of receptor-mediated endocytosis, plays an important role regulating the plasmatic membrane homeostasis and signal transduction, with the ability to recognize specific cargo molecules to be packed inside clathrin-coated vesicles (CCV) and internalized into the cytoplasmatic domain [3]. Due to its central role in the cell life processes, CME has well-known implications in some of the diseases responsible for the higher number of mortality and morbidity [4–6], *e.g.* cancer, Alzheimer's disease and viral entry (i.e. Hepatitis C, Influenza A, vesicular stomatitis virus or members from the coronavirus family such MHV, MERS-CoV, SARS-CoV and SARS-CoV-2).

Considering the major role that CME plays in some of the most basic necessities of the cell, together with its contributions for the development of physiopathological conditions, becomes clear the necessity to better understand how the endocytic machinery act together, driving the internalization of molecules forward. New insights and information about the molecular and atomic organization of the CME pathway can potentially lead to breakthroughs in the development of new biomedical advances and new treatment techniques.

1.2. General aim and particular goals of this work

Considering the points mentioned above, it is crucial to understand how this endocytic pathway works at the molecular levels to develop drugs and treatments that can effectively tackle pathologies related to CME. However, it is important to be fully aware of the high degree of complexity of this pathway, comprising multiple proteins (more than 50 different ones) acting together in a highly coordinated way [7]. Additionally, the majority of key steps of this pathway occur in particular locations at the plasmatic membrane level [3].

The overall features of many aspects of the CME are relatively well understood, *i.e.* the endocytic machinery and the timeline where they interplay with each other to drive the internalization forward is relatively well understood. However, some extremely important questions remain to be answered. Specifically, how the different endocytic machinery acts together in such a coordinated way to produce CCV, the importance of the lipid composition in the formation of the clathrin-coated pits (CCP) and the atomistic resolution of the binding sites of different actors into the scaffold proteins in native-like environments, represent some of the main questions that still need to be addressed.

The general aim of this work focuses on understanding the early steps of CME pathways, particularly, the sorting and cargo selection, and anchoring of adaptor protein 2 (AP2) into the membrane. To address these issues regarding the high degree of complexity of CME pathway, a simplistic approach is used where the system is reduced to its fundamental components *i.e.* PIP2-enriched membranes, AP2 and cargo molecules (TGN38 and CD4).

To achieve the general aim of the work, three main goals have been defined:

1. The atomic-level characterization of the interaction interfaces between the AP2, the second most abundant protein acting on CME, with PIP2 lipids and cargo molecules TGN38 and CD4, embedded in plasmatic membrane-mimetic models.
2. Study of the binding mechanisms of Adaptor Protein 2 into the plasmatic membrane and its dependence on the different membrane anchoring points.
3. The validation of a multi-technique based-approach, comprised of surface-sensitive techniques in combination with solid-state NMR, as a powerful tool to provide a more complete and comprehensive picture of the protein-protein and lipid-protein interaction networks. The combination of these techniques can provide valuable information

necessary for an atomic-resolved characterization, mechanistic characterization and imaging characterization, and lead to an improved understanding of the CME pathway.

Due to the current COVID19 pandemic that recently spread all over the world, the work originally planned was highly affected. Rigid social restrictions were applied, both on Institut Laue-Langevin and on the University of Aveiro, and the access to laboratories and scientific instruments was highly regulated preventing the full performance of the proposed multi-technique approach (Section 2.3). Thereby, the majority of the work produced during the author's internship on Institut Laue-Langevin (from November until early March), and presented across this work, is mainly comprised by QCM-D, ellipsometry and small-angle neutron scattering (SANS) analyses.

2

Introduction

2. Introduction

Endocytosis is the active transport mechanism used by eukaryotic cells to internalize materials from the extracellular to the intracellular domain, i.e. the movement of cellular materials from outside the cell into their cytoplasm. In this cellular mechanism, small vesicles, with size ranging from 60 to 120 nm, are created from the invagination of the plasmatic membrane. These vesicles are responsible for the transportation of materials that cannot permeate themselves through the plasma membrane, e.g. macromolecules like nutrients, growth factors or membrane proteins such as receptors, ion channels and transporters. In fact, these trafficking pathways play an essential role in the regulation of cell communication and signalling processes since these materials are important players in a vast range of physiological processes including cell migration and adhesion, receptor signalling, signal transduction, nutrient uptake, among others [3,8,9]. This fine-tune that regulates the composition of the membrane layers is achieved by the balance between endocytosis and exocytosis.

During the years, different types of endocytic pathways have been described in the literature. Endocytosis can be divided into three main categories: phagocytosis, pinocytosis and receptor-mediated endocytosis [1]. Phagocytosis, also known as "cellular eating", is the type of endocytosis utilized by the cell to internalize large macromolecules or in some cases full cells. In mammals, phagocytosis is executed by specialized cells e.g. macrophages or neutrophils. On the other hand, pinocytosis, also known as "cellular drinking", is responsible for the engulfing of fluids and dissolved nutrients from the extracellular domain to the cytoplasmatic domain. Finally, receptor-mediated endocytosis is a selective type of endocytic pathway, where the molecules to be internalized bind to their specific receptor protein located on the surface of the cell membrane [1,10].

Dysfunctional endocytic processes are linked to some types of physiopathological conditions like Alzheimer's disease, atherosclerosis and cancer [1,11–13]. Additionally, multiple viruses, *e.g.* Influenza A, MERS-CoV, SARS-CoV and SARS-CoV-2, have been reported to hijack endocytic mechanisms to enter the cell [14–19]. A better understanding of the mechanisms ruling the endocytic pathways could potentially lead to a dramatic development of new biomedical advances and new treatments to fight pathological conditions arising from

these dysfunctional endocytic pathways or opportunistic viruses that use endocytosis for viral entry.

Across this work, only one type of endocytic pathway will be approached and explored in detail. Clathrin-mediated endocytosis pathways (CME), a type of receptor-mediated endocytosis, will be addressed with special emphasis in its early steps. Detailed information about other types of endocytosis are not provided here and can be found elsewhere [1,2,10,11,20,21].

2.1. Clathrin-Mediated Endocytosis

The clathrin-mediated endocytosis (CME) is an endocytic pathway crucial to cell basic functions and is used by all known eukaryotic cells [12]. This cellular mechanism is fundamental in processes such as neurotransmission, signal transduction and regulation of the plasmatic membrane homeostasis. The clathrin-mediated endocytosis earned his name after one of his key actors – the clathrin protein. Clathrin is the main protein involved in CME pathways and plays a major role in the formation of the rounded endocytic vesicles [1,12]. During this process, clathrin forms a lattice-like coat around the plasmatic membrane, forcing it to warp until a clathrin-coated vesicle (CCV) is formed. Inside the CCV, some specific molecules are internalized from the plasmatic membrane surface (outer leaflet) into the cytoplasmatic domain [11]. One of the key features of this endocytic pathway is its versatility, allowing the recognition and internalization of a broad variety of different molecules inside the CCV [3].

The clathrin-mediated endocytosis is a highly regulated process that follows a strict set of steps in order to internalize molecules (*figure 1*). The first step of the endocytic event, *initiation*, takes place when a ligand is specifically recognized by the endocytic cargoes present at the surface of the membrane, in a preformed endocytic site. The next step, *cargo recruitment*, is started right after ligand-recognition and it is characterized by the progressive recruitment of cargoes. The cargoes will act as an anchoring point for clathrin-adaptor proteins and scaffold proteins. This recruitment of the endocytic machinery components, and clathrin, gives rise to the *membrane bending* step, where a small, and gradually deeper, invagination on the plasmatic membrane, called clathrin-coated pit (CCP), is formed. The ongoing clathrin-polymerization of the CCP eventually gives rise to the almost complete CCV and therefore to the next step in the CME, the *scission*. During the *scission* step, a

group of scission protein interact with both the CCV and plasmatic membrane in order to separate them. After scission, the newly formed CCV is released in the cytoplasm. The last step of the CME is the *uncoating* of the CCV, where the internalized clathrin-coated vesicle is stripped out of their endocytic machinery proteins, which are recycled for new endocytic events. The newly formed vesicle is released from the inside of the CCV and is free to be transported further within the cell [3,10,22].

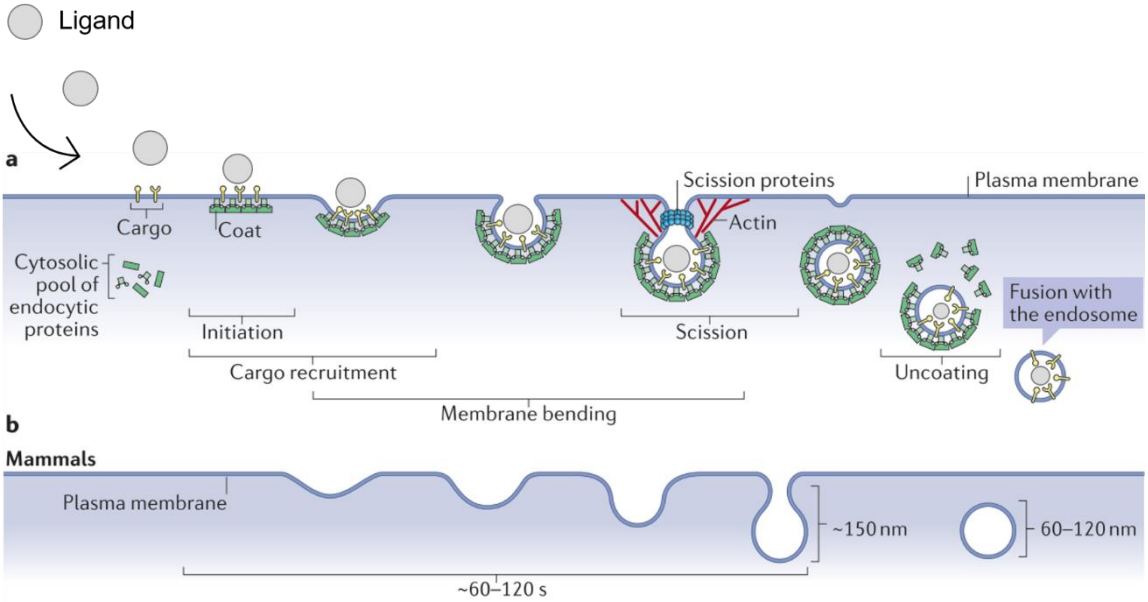

Figure 1 – Clathrin-mediated endocytosis: a) Schematic representation of the different steps in the assembly and disassembly of the clathrin-coated pits (CCP) and clathrin-coated vesicles (CCV) during the CME internalization pathway. b) Plasma membrane shape and dynamical changes during the different steps of the CME. The newly formed vesicles, released from the interior of the CCV, vary in diameter from 60 up to 120nm. Adapted from [3].

During the formation of the clathrin-coated vesicles, an extensive group of proteins acts together in a highly organized and regulated way. While only clathrin was mentioned above, more than 50 different proteins, that play a role in the different steps of the CME, have been described in the literature [7,12]. In this work, only clathrin and adaptor protein 2 (AP2) are considered and will be explored in detail under the next sections.

2.1.1. Endocytic Machinery

The clathrin-mediated endocytosis requires a wide network of adaptor and accessory proteins to accomplish the internalization of cargo molecules. Also, phosphatidylinositol lipids play a major role on the CME. While phosphatidylinositol 4,5-bisphosphate (PI(4,5)P2) is crucially involved in the early steps of the endocytic pathways (*initiation* and *membrane bending* steps), phosphatidylinositol 3,4-bisphosphate (PI(3,4)P2) role only takes

place in a latter phase, reaching maximum levels during the *scission* step and gradually decreasing after the CCV formation [3,10,22]. In this work, we aim to deeply simplify the endocytic system, hence only the basic components of the pathway will be studied, *i.e.* clathrin, adaptor protein 2 (AP2), cargo molecules (TGN38 and CD4) and phosphatidylinositol 4,5-bisphosphate (PI(4,5)P2). In the next sections, all the above components will be explored in detail. For a matter of simplicity, from this point forward, phosphatidylinositol 4,5-bisphosphate (PI(4,5)P2) will be addressed as PIP2.

2.1.1.1. Phosphatidylinositol 4,5-bisphosphate

A large number of clathrin-mediated endocytic proteins selectively interact with phosphatidylinositol lipids. Amongst the different isoforms of phosphoinositides, phosphatidylinositol 4,5-bisphosphate (PIP2) seems to be crucial to the CME initiation and cargo recruitment. In fact, almost half of the protein machineries of CME have specific domains to bind to PIP2 [7]. These lipids are located in the inner leaflet of the plasmatic membrane with their head groups oriented to the center of the cell [23,24].

Evidences seem to point that the presence of PIP2 is essential to the CME dynamics, especially during the endocytic initiation. In fact, some studies have shown that the CCP assembly and CCV formation/uncoating are disrupted when PIP2 levels are changed [25]. Similarly, different researches have shown that the acute depletion of PIP2, either by a phosphatase or by inhibition of production through butanol, results in an almost complete loss of CCV [26,27].

Even though some aspects of the phosphoinositides contributions in the CME have already been addressed in great detail, such as the dynamic conversion of phosphoinositides during CME endocytic traffic [28] or the dependence of phosphoinositides in the progression of the various steps of the endocytic event [3,7], others aspects still need further clarifications. One example of this is highlighted by the lack of atomic-resolved characterization studies of the interaction interfaces between AP2 and PIP2 embedded in bioinspired membrane-based systems. Additionally, from a mechanistic point of view, further studies are necessary to shed light into the interaction between AP2 and PIP2 lipids, during the docking of AP2 into the membrane. Both these points constitute aims that this work intends to address.

2.1.1.2. Adaptor Protein 2

The adaptor protein 2 (AP2) is a member of the heterotetrameric adaptor protein family and has a pivotal function in the formation of CCV. This protein is formed by two large subunits of ~110kDa, α and β2, a medium subunit of ~50kDa, μ2, and a small subunit of ~17kDa, σ2 [29]. The subunits of the AP2 form a large globular structure with two projecting appendages called "ears". These subunits contain domains for the recognition of clathrin, PIP2, and cargoes [30]. In fact, studies have suggested that the AP2 complex is only activated when PIP2-enriched areas are present in the plasmatic membrane. The binding of AP2 to PIP2-enriched areas allow the selection and recognition of cargoes to be internalized [31]. Therefore, the crucial role played by the AP2 arises from his ability to bind to the plasmatic membrane, specifically on PIP2-enriched areas, recognize cargo molecules and mediate the assembly of the clathrin into the endocytic complex.

The majority of the transmembrane proteins are selected to internalization through the recognition of specific short and linear amino-acids motifs (previously referred as cargoes) present in the cytoplasmatic domain. AP2 has the capacity to recognize two of the most commonly found internalization signals, the tyrosine-based motif and acidic dileucine motif [30,32]. The tyrosine-based motif pocket, often represented as YxxΦ, is accommodated in the μ2 subunit while the acidic dileucine motif, [DE]xxxL[LI], is found on the boundary of α-σ2 subunits. TGN38 and CD4, the cargo molecules used throughout this work, are recognized through YxxΦ (Φ is an amino acid with a large hydrophobic side chain) and [DE]xxxL[LI] internalization signals, respectively [33].

The heterotetramers of AP2 can adopt two different conformations: one closed (or locked) and an open conformation (*figure 2*). In the closed conformation, adopted in the absence of membrane interaction *i.e.* binding of PIP2, the binding sites for the tyrosine and dileucine recognition motifs are blocked by the β2 subunit. The conformational change from the locked state to the open state is favoured when AP2 is recruited to the plasmatic membrane, specifically PIP2-enriched areas. The binding of PIP2 on α and β2 subunits causes a change in the position of C-μ2, which also binds to PIP2. The C-μ2 subunit changes its position, originally accommodated in the core of the protein, to the proximity of the membrane surface where it binds to a third PIP2. Both the rearrangement of C-μ2 and binding to PIP2 triggers a conformational change on AP2, into the open state [33,34]. The structural changes on AP2 allow β2 subunit to move into a more "relaxed" position. This

small movement of β2 uncovers the tyrosine and dileucine motif-binding sites and therefore allow the transmembrane cargoes internalization signals to be recognized by AP2. Additionally, the conformational change that AP2 undergoes during this process is also equally important to reveal the β2 binding site of clathrin which, similarly to the cargoes recognition signals, is hidden during the close-state conformation [34]. AP2's conformational modifications are considered a defence mechanism to selectively activate the protein at the cytoplasmatic membrane level and prevent inappropriate recognition of cargo molecules in other membranes *e.g.* Golgi apparatus [30].

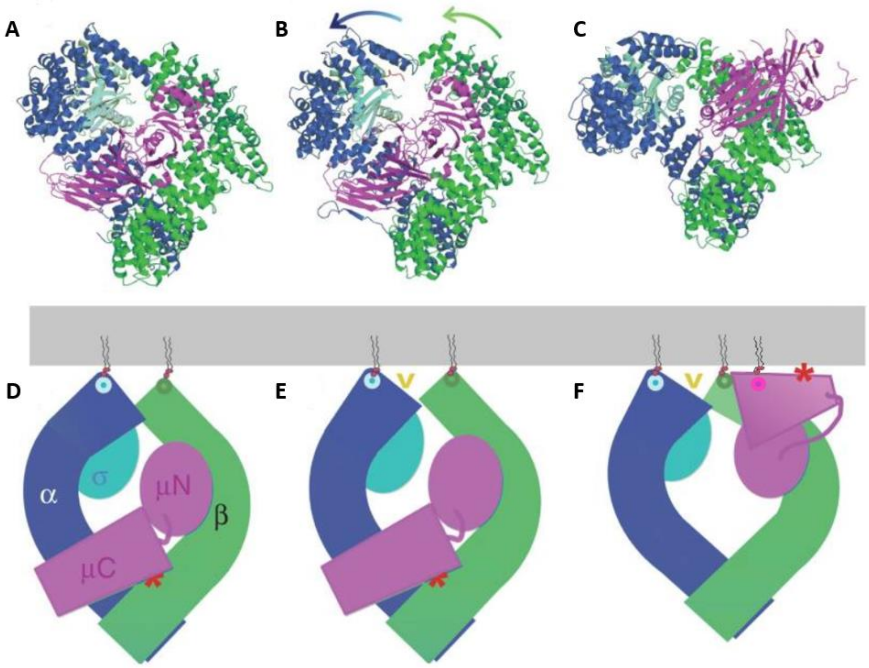

Figure 2 – Adaptor protein 2 conformational structure dynamics: A-C) Ribbon representation of the heterotetramic AP2 structure in the closed conformation (A), unlatched state (B) and open conformation (C). D-F) Schematic illustration of the A-C conformational states. In the closed conformation, A and D, AP2 binds to PIP2 through α and β2 subunits, the binding sites of dileucine and tyrosine motifs are blocked by the β2 subunit. The unlatched conformation, B and E, is characterize by in intermediate orientation between the close and open state. This conformational structure was trapped by crystal packing. Curiously, this AP2 unlatched orientation only has one of the cargo-binding sites accessible. The open conformation, C and F, is connected to the plasmatic membrane through PIP2 on α, β2 and C-μ2 subunits. The rearrangement of the C-μ2 and β2 subunits free the cargo binding sites recognition pockets. The yellow **v** represents the [DE]xxxL[LI] motif binding site and the red * represents the YxxΦ. Adapted from [22].

During the last two decades, David J. Owen and collaborators provided some of the major contributions leading to a refined understanding of CME pathways from an atomic and molecular point of view. Their work collection, mainly achieved through x-ray crystallography, comprises the full characterization of all the subunits of AP2 [35], characterization of AP2 with cargo molecules [30,32] and the postulation of the actual model of

AP2 conformational change [33]. Nevertheless, all these studies where carried out in the absence of the natural lipid environment provided by the plasmatic membrane. Therefore, further studies with membrane-mimetic systems are necessary to complement the already established work.

2.1.1.3. Clathrin

Clathrin is the major protein involved in the CME pathways and the basic unit of the CCV. The clathrin structure comprises three heavy chains of ~190kDa and another three light chains ~25kDa connected to a central hub (also known as *tripod*) forming a triskelion-like shape, as shown in *figure 3a* [3,22,36,37].

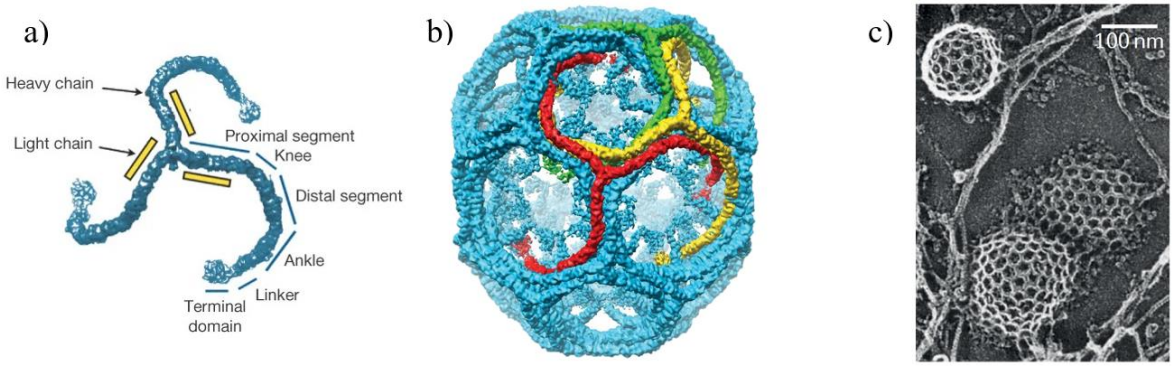

Figure 3 – Clathrin: a) Schematic representation of the clathrin triskelion. The different sections and names that compose the heavy chain are presented. Light chains are colored in yellow. b) The clathrin cage structure of the CCV comprised of hexagonal and pentagonal lattices of 36 clathrin molecules is displayed. Light chains not shown. c) Cryo-electron microscopy observation of the assembly of clathrin-coated vesicles of different sizes and shapes. Adapted from [3,36].

The clathrin protein has the ability to polymerize and build a polygonal lattice structure, therefore, forming the clathrin-coated vesicles in the CME pathways (*figure 3b*). The polymerization of the clathrin arises from the interaction between different clathrin molecules [36]. Clathrin polygonal structures are comprised of hexagonal and pentagonal lattices, that can form CCV with different sizes and curvatures [3,22], as shown in *figure 3c*.

Is important to emphasize that clathrin has no native membrane binding capacities and therefore needs scaffold proteins in order to bound to the plasmatic membrane. The binding between clathrin and scaffold proteins, such as adaptor protein 2, is achieved through the N-terminal domain of the triskelions. Clathrin heavy chain N-terminal comprises a linear amino acid sequence motif with the LΦxΦ[DE] consensus sequence, commonly called

"clathrin-box" [22,30]. The clathrin-box sequence is recognized by AP2, through a projecting appendage in the β2 subunit, when the open conformation is adopted [38].

2.1.2. Clathrin-Mediated Endocytic Pathways

The clathrin-mediated endocytic pathway is composed of a series of sequential steps highly regulated such as initiation, cargo recruitment, membrane bending, scission and uncoating [12]. In this work, special attention is given to the early steps of the CME pathways, specifically the initiation of the endocytic events and cargoes selection. In this section, the steps mentioned above will be addressed and explored in detail. The later stages of CME pathway are not featured on this section, and further information can be found elsewhere [1,2,12,22,39].

The first step of the CME pathways is the initiation of the endocytic event by the crowding of the first endocytic machinery in the proximity of the plasmatic membrane. The initiation of the endocytic site arises from an event often called "nucleation". Traditionally, according to the canonical CME interpretation, it was believed that the formation of the original coated pit requires the binding of AP2 to PIP2-enriched areas in the plasmatic membrane by random Brownian motion. Contrary to this notion, recent studies suggest that a complex nucleation module is formed comprised of different types of accessory proteins, e.g. FCHO1/2, Eps15, Eps15R and intersectins1 and 2 [3,12,22]. The accessory proteins of the nucleation module seem to bind to AP2, after recognition of PIP2-enriched areas, increasing the stability of the interaction between AP2 and the membrane and therefore avoiding that the clathrin-coated pit fails to maturate and collapse [22,39]. Moreover, the initiation sites, in some cases, seems to be precisely placed in the same areas of the plasmatic membrane or in specific regions of cells [3]. This feature of the CME might imply that specific areas of the plasma membrane have the ability to concentrate PIP2 or endocytic cargoes, therefore precisely picking the place where the initiation of the endocytic event takes place. However, it is important to highlight that is still not fully understood if cargo molecules are essential to the formation of the endocytic site or if they are just recruited after the latter is already formed.

After the initiation of the endocytic events and the assembly of the adaptor and accessory proteins into the endocytic complex, the next step of CME pathways, *cargo recruitment*, takes place. The interaction of AP2 with PIP2 causes a major conformational

change in the former, allowing it to adopt his open state. This conformational change is characterized by the uncovering of the cargo recognition motifs and the clathrin binding site on the β2 appendage. Recently, Owen and coworkers have shown that the binding of clathrin and the phosphorylation of AP2's μ2-Thr156 residue have a major role on the stabilization of the AP2 conformation before cargo recognition. These events promote a correct conformational change, essential for an efficient cargo selection [40]. An effective cargo selection seems to be crucial to the maturation of CCP into a fully functional CCV. Some studies point that a sort of "cargo checkpoint" happens before the maturation of the CCP into CCV, where a threshold of cargo molecules must be achieved in order to successfully accomplish the CCV formation. If the threshold is not achieved, abortion of the endocytic site could happen or alternatively the maturation of the CCP can be delayed, in order to allow recruitment of additional cargo molecules [3]. Additionally, it was shown recently that the recognition of the tyrosine-based motif cargoes modulates an efficient allosteric activation of AP2 on the membrane, contrasting to the little effects observed on the acidic dileucine motifs [34].

Many aspects of these two initial steps of CME are not fully understood *e.g.* the role of the cargoes in the endocytic sites, the influence of lipid composition in the formation of the CCP or the hierarchy of the interaction of the different membrane anchoring points with AP2, are some examples that require further clarifications. One of the aims of this work addresses one of these points and covers the clarification of the binding mechanisms of AP2 into the plasmatic membrane and its dependence on the different membrane anchoring points.

2.1.3. Clathrin-Mediated Endocytosis and disease

Malfunctioning in the endocytic machinery have been related to multiple pathologies and impaired health [4,5,41]. The first observations that suggested a relation between endocytic pathways and physiopathological conditions go back to the 1970s, in specific, to the groundbreaking work of Michael Brown and Joseph Goldstein [42]. In a series of revolutionary reports, that earn them The Nobel Prize in Physiology and Medicine latter in 1985, they paved the way to a better understanding of the mechanisms underlying the regulation of the cholesterol metabolism and treatment of diseases caused by the elevated cholesterol levels in the blood [6,42]. Their findings led to the proposal of the receptor-mediated endocytosis

model [6,43]. This work is impressive in many ways. First, it completely changed the way membrane trafficking was thought-of, since until then it was largely believed that macromolecules enter cells through nonspecific means [43]. Second, the postulated model still stands today, with concepts like *"high-affinity receptors"*, *"cargo selection"* and *"recycling pathways"*, introduced more than 40 years ago, currently still being mentioned in the field-related literature. Third, the work performed with Despota's cells was crucial to prove that dysfunctional endocytic machinery is directly related to physiopathological conditions, *e.g.* hypercholesterolemia, in the case of Despota's [42].

The work of Brown and Goldstein laid the ground for the development of a completely new field of research, receptor-mediated endocytosis. Since then, more than 40 years later, much more is known about the different types of receptor-mediated endocytic pathways and the implications of abnormalities in these pathways in the development of diseases. Even though many diseases have been linked to endocytic pathways, in this section special attention is focused on the relation between CME and Alzheimer's disease, cancer and viral infections, since these type of diseases are major challenges for humankind nowadays [4].

The relationship between CME and Alzheimer's disease has been widely explored and multiple genetic studies have related altered expression levels and variants of endocytic machinery with higher risk of developing Alzheimer's disease, *e.g.* clathrin assembly lymphoid-myeloid leukaemia gene (commonly referred as CALM) [44,45], AP2 [46], synaptojanin [47]. Additionally, the endocytic trafficking of the amyloid precursor protein (APP) also plays a major role in the development of Alzheimer's disease [13]. APP cellular location is a major determinant to its processing and, therefore, to the production of its amyloidogenic (Aβ peptide) or nonamyloidogenic cleavage product. The processing route that gives rise to the amyloidogenic product takes place after APP's uptake through CME, while the nonamyloidogenic processing occurs in the plasmatic membrane [6,48].

Cancer and CME relationship is associated with the altered signalling exhibited by cancer cells, a key aspect is some of its characteristic properties such as proliferation, angiogenesis or migration [49]. In fact, cancer cells take advantage of impaired endocytic trafficking, through optimized signalling pathways, to enhance the aberrant cellular growth and invasion potential. One example of this feature is the capacity of cancer cells to hijack the endocytic pathways avoiding degradation of receptors and recycling them to the cell

surface, therefore, maintaining signalling. Many oncogenic key receptors undergo into this recycling pathway *e.g.* epidermal growth factor receptor (EGFR) [50,51] or integrins [52–54].

The viral attachment and entry into the host cell, key steps on viral infections, are intrinsically connected to endocytic internalization pathways [19]. Even though viruses seem to be optimized to hijack specific routes that suit their shape and form (large viruses are internalized through phagocytosis while smaller and elongated viruses use micropinocytosis [15]), the most common endocytic pathway for viral entry is the clathrin-mediated endocytosis, mediating the entry of many viruses *e.g.* SARS-CoV, MERS-CoV, Influenza A and Hepatitis C [15–19]. The interaction of viruses with CME is widely dependent on the type of virus and its specificities, with receptor proteins and internalization mechanisms changing from virus to virus. For instance, while some viruses have the ability to induce de novo formation of CCP, others use preformed CCP [19]. Analogously, the surface receptor molecules are also widely dependent on the type of viruses, with some virus using proteins (*e.g.* integrins), while others use polysaccharides (*e.g.* glycosaminoglycans), and others can use both [19]. Despite these variations, multiple endocytic inhibitors proven its efficiency, decreasing viral entry [18]. Concerning SARS-CoV-2, research moves fast and many works are under development to identify an effective treatment to fight the virus and help to stop the ongoing pandemic. Indeed, a recent publication has shown that chloroquine can inhibit SARS-CoV-2 viral entry in VeroE6 cell, in-vitro, by increasing the endosomal pH and preventing the formation of the late endosome [18,55]. New insights about the entry mechanisms and possible implications at the endocytic pathways of this newly identify virus need further investigations. Nevertheless, it is likely that SARS-CoV-2 share similar endocytic processing with its predecessor SARS-CoV, which is known to use CME pathways [16,17].

2.2. Cell Membrane simulation: Biomimetic Membrane systems

Biological membranes are crucial and play an essential role in cellular life. This structures act as a selective barrier between the extracellular and intracellular domain, therefore ensuring homeostasis, material uptake, energy regulation, cellular signalization and molecular recognition [56]. The plasmatic membrane is a complex structure composed of a wide variety of constituents, such as glycerophospholipids, sphingolipids and sterols, proteins and carbohydrates. The recreation of the membrane environment, *in vitro*, is achieved through biomimetic membrane systems. Membrane mimetics are especially

attractive in biological studies due to their capacity to recreate *in-vitro* an accurate representation of the membrane environment felt *in-vivo*. This mimicking capability enable the performance of more rigorous studies on membrane-dependent processes since these membrane-mimetic systems create native-like environments that closely resemble the natural environment [57,58].

Many types of biomimetics membranes have been developed through the years, embracing a wide range of applications [57–59]. For many applications, these membrane mimetics allow the simplification of the studied system, they are cheaper and fairly easy to produce, they offer good reproducibility and they are more stable, compared to *in-vivo* options [57–59]. In addition, many of the biomimetic models are suitable for characterization with surface-sensitive techniques and NMR, *e.g.* supported lipid bilayers, liposomes or micelles. Nevertheless, special care should be taken when picking the components of these models since misleading observations can happen due to oversimplification of the overall system.

Across this work, two membrane-based models were employed *i.e.* lipid vesicles (also known as liposomes) and supported lipid bilayers (SLBs). In this section, a general overview of these models is provided, where the models are briefly described and some of the main advantages and disadvantages of each model are highlighted. Additional information regarding other types of membrane mimetic models can be found elsewhere [57,58,60].

2.2.1. Lipid vesicles

Liposomal vesicles are often used to study different plasmatic membrane processes like phase behaviour, membrane fusion, molecular recognition and cell adhesion to name a few. Liposomes are classified into two types: multilamellar vesicles (MLVs) and unilamellar vesicles (UVs), as shown in *figure 4*. A further categorization distinguishes the different types of unilamellar vesicles in: giant unilamellar vesicles (GUVs), >1μm; large unilamellar vesicles (LUVs), 100-1000nm; and small unilamellar vesicles (SUVs), <100nm [61].

Originally discovered by Bangham and Horne, multilamellar vesicles are spontaneously formed when a dry phospholipid film is hydrated [62]. Multilamellar vesicle exhibit an onion-like structure with multiple phospholipid bilayers wrapped around each other, with the outer bilayer enveloping the next inner layer. Indeed, the preparation of

liposomal vesicles is quick and easy to achieve because they assemble spontaneously into a vesicle shape in the presence of water. Phospholipids are amphipathic molecules and when in contact with water, they rearrange themselves in a way that effectively minimizes the interactions between their hydrophobic tails with water, leading to the formation of liposomal vesicles [60,61]. To achieve this, the phospholipids orient themselves into circular bilayer sections, each bilayer comprised by two phospholipid layers oriented with head-tails-tails-head, where the hydrophilic heads of phospholipids are pointing outwards and in contact with the bulk, while their hydrophobic tails are protected from water interaction in the inner section of the bilayer [63].

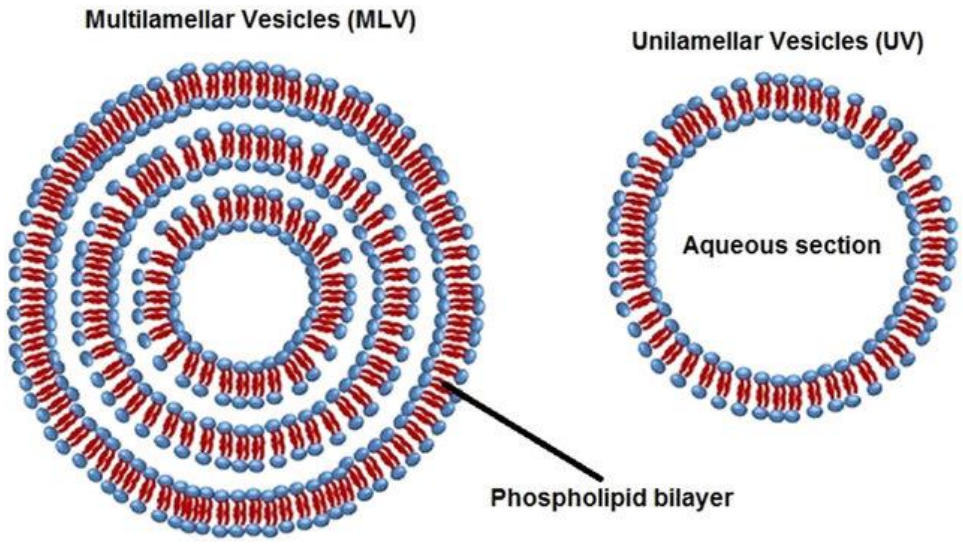

Figure 4: Schematic representation of both types of liposomal vesicles, multilamellar vesicles (MLV) and unilamellar vesicles (UV). Multilamellar vesicles (left), formed through hydration of a dry lipid film, exhibit an onion-like structure with multiple phospholipid bilayers, each one gradually enveloping the next inner layer. Unilamellar vesicles (right) are formed by a single phospholipid bilayer, with sizes ranging from ~30nm up to >1μm. Adapted from [64]

Even though liposomal vesicles are formed spontaneously when dry lipid films are hydrated, most applications rely on unilamellar vesicles (UVs) instead of the spontaneously formed multilamellar vesicles (MLVs). The lamellarity and size profiles of the liposomes can be adjusted by a group of well-known techniques fully described in the bibliography. The production of these systems (LUVs or SUVs) demands energy to produce them, since they have higher free energies. Generally, they are generated by techniques such as extrusion or sonication [60]. Additionally, liposome-based models are quite versatile enabling several experimental set-ups since these vesicles can be analyzed dispersed in solution, *e.g* small-angle neutron scattering (SANS), small-angle x-ray scattering (SAXS), dynamic light

scattering (DLS) and static light scattering (SLS), or pelletized in a semisolid state, *e.g.* solid-state nuclear magnetic resonance (ssNMR).

The main limitation of this biomimetic model lays on the lack of capacity to replicate the membrane asymmetry of each leaflet. Additionally, the final liposomal solution can have a different composition from the initial lipid mixture prepared during the vesicle formulation [60]. The phase behaviour, and therefore the stability of the formed vesicles, is highly dependent on the type and ratio of lipid used in the vesicle formulation [65].

2.2.2. Supported lipid bilayers

The supported lipid bilayers (SLBs) are biomimetic membrane models characterized by a continuous lipid bilayer deposited into a solid substrate [56,57,60]. The solid substrates should be smooth, extremely clean and hydrophilic. Generally, these solid substrates are made of glass, mica or silicon oxide. SLB models provide a set of characteristics that make them widely attractive, especially when comparing them to lipid monolayers models which are comprised of only one phospholipid layer, oversimplifying the experimental conditions [57]. Additionally, since these membranes are assembled into solid support, they are easily characterized by surface-sensitive techniques such as AFM, ellipsometry, quartz crystal microbalance with dissipation monitoring (QCM-D), neutron and X-ray reflectivity [60].

Several methods to produce SLBs have been described; however, the two main methods are the widely used Langmuir deposition techniques and vesicle fusion.

The first method to produce SLBs, through Langmuir deposition techniques, consists of a two-step process. In the first step, a lipid monolayer in the air-water interface is transferred to the hydrophilic surface of a functionalized solid substrate [66]. The transfer process of the lipid monolayer into the solid substrate is achieved through the movement of the solid substrate, vertically oriented, out of the Langmuir trough, as illustrated in *figure 5a*. The lipid monolayer, previously prepared, is adsorbed into the hydrophilic surface of the solid substrate, with the lipid heads oriented to the substrate and tails oriented in the opposite direction [57]. After the formation of the first monolayer on the solid substrate a similar process is performed in the step-two. In the second step, the same solid substrate is placed horizontally (parallel to the air-water interface) and dipped into the subphase, therefore, adsorbing the second monolayer and forming a supported lipid bilayer [56,60,66]. The final structure is comprised of two lipid monolayers, as represented in *figure 5b*. The formation

of the lipid bilayer, through the assembly of two monolayers, is achieved by Langmuir-Blodgett depositions (LB, first monolayer) and Langmuir-Schaefer (LS, second monolayer), as previously described. The main advantage of this technique is the possibility to produce both symmetric and asymmetric bilayers while keeping an accurate control of the overall composition of each leaflet [57]. Additionally, SLBs produced through Langmuir deposition techniques are highly homogenous, both in coverage and thickness.

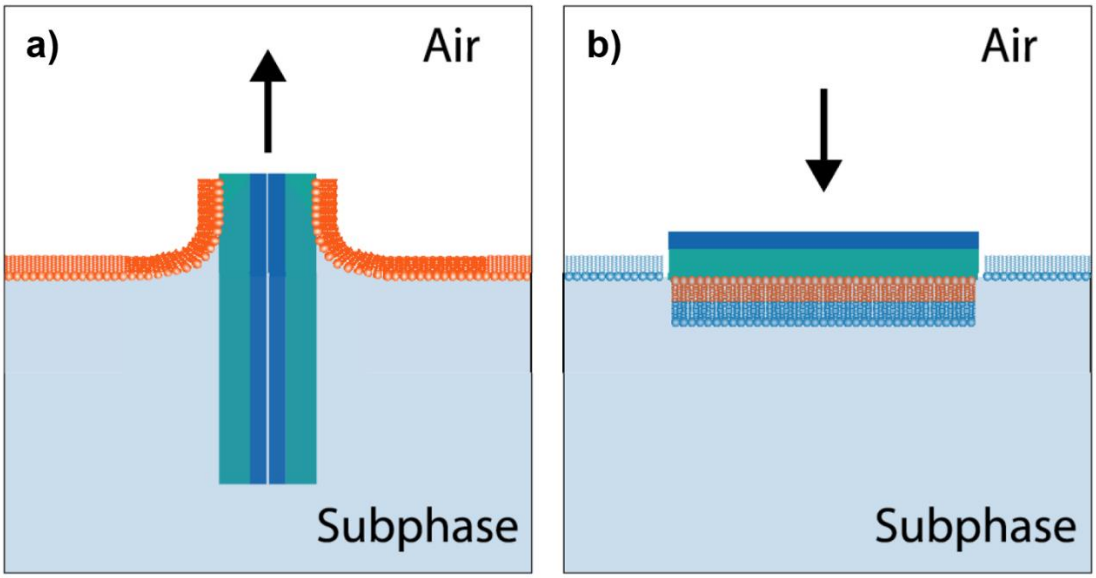

Figure 5: Langmuir deposition techniques: a) Langmuir-Blodgett deposition; b) Langmuir-Schaefer deposition. The main differences between both deposition techniques lay in the substrate orientation, relative to the air-water interface, and the direction of the movement. One should highlight that the combination of these deposition techniques allows the production of both symmetric and asymmetric bilayers. In the example presented in this picture, an asymmetric bilayer is assembled with two different leaflets, orange and blue. Adapted from [67]

The second method to produce SLBs is through vesicle fusion into a solid substrate. This method involves the adsorption and fusion of SUVs into a functionalized solid substrate. The lipid polar head groups are adsorbed on the hydrophilic surface of a functionalized solid support, which creates deformations that are translated in the flattening of some vesicle zones. The instability arising from this flattening will trigger the vesicle rupture [60]. The rupture and fusion of the vesicles on the surface give rise to a final supported lipid bilayer. One major advantage of this methodology is the possibility to prepare supported lipid bilayers in microfluid chambers, therefore, allowing the possibility to flow biological assemblies *e.g.* proteins or carbohydrates and study their interaction with the bilayer [61]. Additionally, this method is fairly simple which make it widely attractive. Nevertheless, this method has some limitations compared to Langmuir depositions. First, it

is not possible to produce asymmetric bilayers neither precisely control the overall composition of the bilayer, since liposomes final concentration can have slight deviations from the prepared initial lipid mixture. Second, this procedure needs to be carried at temperatures above the liquid phase transition what can be difficult to achieve for some lipid mixtures. Third, the final supported bilayer produced through this method is more prone to have defects like holes, kinks or patches with vesicles trapped in between the planar bilayer.

Indeed, the formation of lipid bilayers in solid substrates poses as an attractive biomimetic model capable of providing stability and robustness to the lipid layers. Nevertheless, the supported lipid bilayer has some limitations arising from the solid substrate itself since the lipid bilayer and the solid substrate are separated through an ultrathin water layer with 10-20 Å of thickness [56]. For instance, this small separation can lead to immobility of transmembrane proteins or repulsive disruption of surface binding proteins through defects within the SLB [56,57].

2.3. Multi-technique approach to characterize interaction in CME

Endocytic pathways exhibit a complex nature with multiple actors playing along in a highly coordinated choreography [22]. In many ways, the recreation of these complex pathways *in-vitro* is challenging. One of the main challenges of these systems concerns the interaction of the endocytic proteins with the plasmatic membrane and its constituents. This complexity gives rise to numerous analytical problems. For instance, the atomic characterization of many proteins involved in CME, together with the characterization of their binding sites for cargo molecules, have already been addressed by X-ray crystallography [29,30,32,33,40]. Even though this technique has proven to give valuable insights into the overall understating of the atomic structure and interactions between the endocytic machinery, they rely on an immobilized state of proteins. Additionally, these studies are carried out in the absence of the lipid environment of the plasmatic membrane due to difficulties to obtain good quality crystalline samples, induced by the intrinsic heterogeneity of the system. In fact, no atomic characterization studies of endocytic proteins embedded in the membrane have been reported in bibliography. These limitations highlight the necessity to address this problem with a fine-tuned approach embracing different analytical techniques capable of providing detailed information about dynamical and inter/intramolecular

interactions of the endocytic machinery in the presence of the lipid environment of the plasmatic membrane.

The combination of different analytical techniques provides a more complete and comprehensive understanding of the protein-protein and lipid-protein interaction network. This approach is attractive not only because it allows one to obtain relevant and complementary data but also to overcome the limitations of a single-technique approach. Additionally, the utilization of different methodologies and techniques enable cross-validation and cross-fertilization of data sets, procedures and findings. Therefore, the combination of different techniques renders an optimized experimental strategy capable of providing valuable data, supporting and complementing other characterization techniques, such as X-ray crystallography.

The proposed multi-technique approach of this work, to address the interaction between AP2, PIP2 lipids and cargo molecules embedded in the plasmatic membrane, is comprised by ssNMR, neutron scattering, QCM-D, AFM imaging and ellipsometry. The combination of MAS-DNP (magic-angle-spinning dynamic nuclear polarization) and ssNMR can provide a very detailed atomic characterization of the lipid-protein and protein-protein interactions. Additionally, neutron scattering techniques, such as neutron reflectometry and small-angle neutron scattering (SANS), can provide structural information of the overall lipid-protein complex, with very high spatial resolution. Lastly, AFM, QCM-D and ellipsometry can provide information regarding the dynamics and kinetics, with very high temporal resolution. The combination of these analytical techniques can provide a very in-depth image of AP2 interaction interfaces with PIP2-lipids and cargo molecules in all aspects. Moreover, this approach may give a detailed analysis of the binding mechanisms of AP2 into the plasmatic membrane and its dependence on the different membrane anchoring points. Certainly, the encompassing of the different methodologies will provide a better all-around understanding of the CME from a functional and structural point of view.

In this section, a detailed description of QCM-D basics and theory is presented. Additionally, a brief overview over ellipsometry and SANS is also provided. No information is provided regarding the remaining techniques proposed in the multi-technique approach since no analysis were performed, as described above (Section 1.2).

2.3.1. Quartz crystal microbalance

The quartz crystal microbalance (QCM) is a gravimetric technique based on acoustic waves generated by an oscillating piezoelectric quartz crystal. The basic principle of QCM relies on quartz inherent property of piezoelectricity, which means that when an appropriate voltage is applied the crystal structure of the quartz will experience successive expansions and contractions, *i.e.* the quartz crystal will oscillate at a defined frequency [68,69]. The frequency of the quartz oscillations is sensitive to small amounts of mass therefore, frequency changes are monitored to quantify the mass adsorbed on the quartz crystal surface. This nondestructive technique is a highly sensitive mass balance, with the capacity to perform real-time measurements from microgram up to nanogram mass changes in the interfacial adlayers.

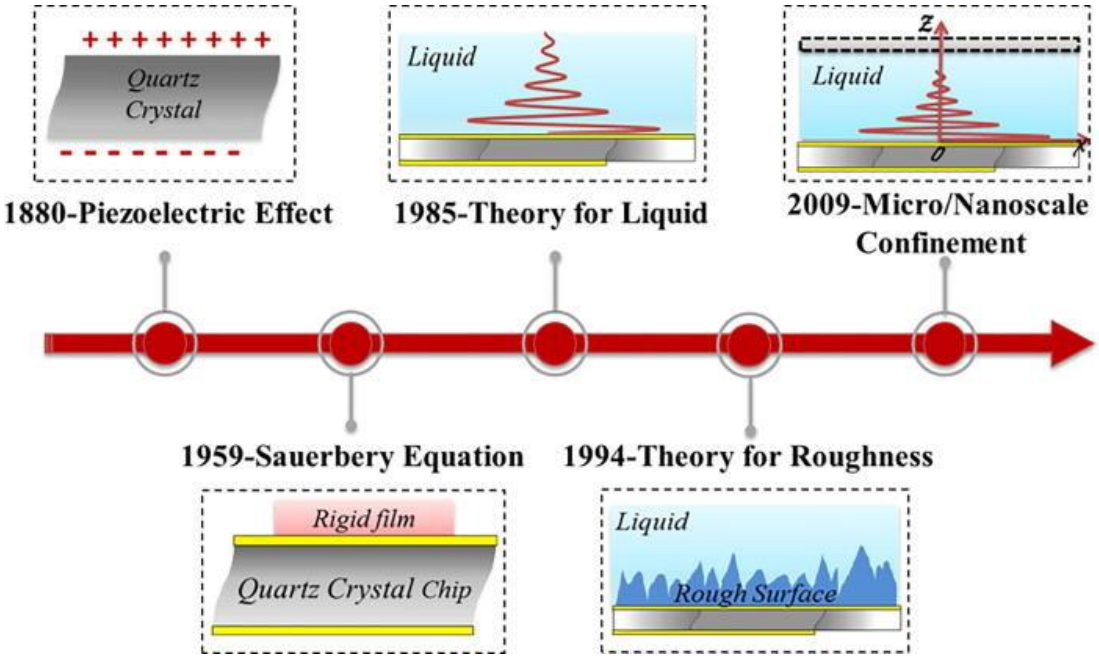

Figure 6: Schematic representation of history evolution of quartz crystal microbalance technology. Reprinted from [70].

The QCM became widely used in labs as a mass balance after the work of Günter Sauerbrey, in 1959, showing a linear relationship between the frequency change of the oscillating crystal and the mass adsorbed on its surface [71]. Since then, QCM was used almost exclusively under vacuum or gaseous environments. Roughly 20 years later, it was shown that QCM principle, piezoelectricity of the quartz crystal, could also be applied in liquid environments [72–74]. One of the main advantages that emerged from this breakthrough was

the possibility to perform experiments in microfluid chambers (used on this work) which helped to revolutionize this technique, dramatically expanding its applications to new areas like biosensors, rheology and biology [68,70].

The possibility of performing experiments in microfluid chambers make this technique suitable to study and monitor in real-time the formation of SLBs through vesicle fusion [75,76]. Additionally, the sequential construction of adsorbed multilayers enables the possibility to study the adsorption of proteins into the previously formed bilayer, functionalized with recognition sites [77–79]. These characteristics are very attractive for the scope of this work since they provide a direct way to monitor the interaction between macromolecules in a native-like lipid environment.

2.3.1.1. Quartz crystal: a piezoelectric resonator

The principal component of the QCM equipment is the quartz crystal chip. Quartz minerals exhibit a group of properties such as piezoelectricity, high natural abundance, easy production, and good thermodynamic stability, which make this type of minerals the most suitable candidate for QCM applications [80,81].

The quartz sensor utilized in modern QCM equipment's is an AT-cut quartz crystal sandwiched between two electrodes. These electrodes are commonly made of gold; however, its materials can widely vary according to the desired application. The AT-cut, represented in *figure 7*, is performed at a specific 35.25º relative to the z-axis [81]. This type of processing of the quartz crystal is essential to assure that the sensor has good stability, *i.e.* low-temperature coefficients and a pure shear mode of oscillation [81].

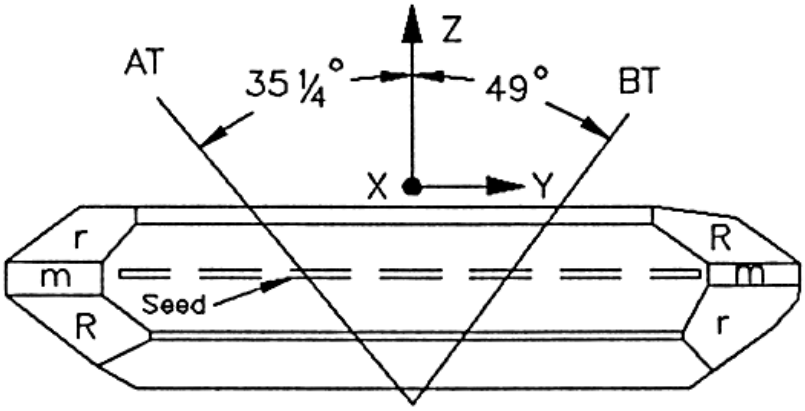

Figure 7: Schematic representation of the AT-cut performed in the quartz crystal to obtain a stable quartz chip for QCM applications. The orientation of the cut is intrinsically related to the sensors frequency-temperature properties 80.

The AT-cut quartz sensor, due to its piezoelectric properties, will oscillate in a pure thickness-shear-mode when an alternating current (AC) voltage is applied with a frequency close to the resonant frequency (f_0) of the crystal. The deformation felt by the crystal is characterized by successive expansions and contractions in an anti-parallel mode, *i.e.* the two surfaces of the crystal will deform in opposite directions, as illustrated in *figure 8*. The fundamental resonant frequency (f_0) of a quartz crystal can be calculated from *equation 1*:

$$f_0 = {}^{v_q}/_{2t_q} \quad (1)$$

where υ_q is the wave velocity in the quartz plate (*3336 m/s*, for a 5 MHz sensor) and t_q is the thickness of the quartz plate [68,82]. From *equation 1*, one can observe that the fundamental resonant frequency is inversely proportional to the crystal thickness. In fact, the resonant frequency and the crystal thickness are intimately related to the sensitivity and usability of the sensor, respectively. Typically, the commercial chips are 5 MHz sensors with a thickness of approximately 330 µm. This type of sensors is widely used because they combine a good signal-to-noise ratio with a good surface area for QCM applications.

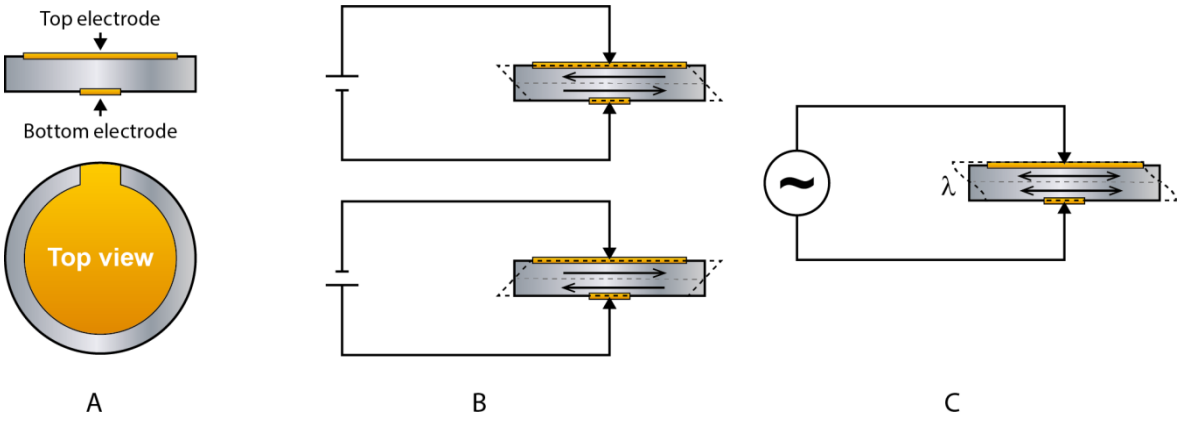

Figure 8: QCM quartz sensor: A) Schematic illustration of the side and top view of a typical QCM sensor. The surface area available for experiments is represented in the top view in yellow. Commercial suppliers provide a wide range of sensor with different surface modifications e.g. aluminium oxide, biotin, cellulose, copper, gold, his-tag, iron oxide, egg yolk, silicon dioxide, amongst many others. B) The application of voltage with a frequency near the fundamental resonant frequency of the crystal will make the quartz deform in an anti-parallel mode of vibration. C) The application of an AC voltage will make the crystal oscillate in successive expansions and contractions. Reprinted from [83].

2.3.1.2. Sauerbrey equation: mass sensitivity and limitation

As mentioned before, the groundbreaking work of Günter Sauerbrey, in 1959, allowed the development and establishment of QCM technology as a sensitive mass balance

[71]. Sauerbrey demonstrated that the frequency changes of the oscillating crystal (Δf) was linearly related with the mass adsorbed on its surface (Δm), as expressed in *equation 2* (widely known as *Sauerbrey equation*):

$$\Delta m = \frac{C}{n}\Delta f \quad (2)$$

where *n* is the harmonic number and *C* is a constant that is related to the fundamental properties of the quartz crystal used and can be calculated from *equation 3*:

$$C = \frac{t_q \times \rho_q}{f_0} \quad (3)$$

where ρ_q is the density of the quartz and f_0 is the fundamental resonant frequency of the quartz crystal [68]. For a common 5 MHz sensor at room temperature, C has a value of approximately -17.7 ng/(cm^2.Hz) [68,69]. In this case, the physical meaning of C is that for each 17.7 ng/cm^2 of mass adsorbed on the crystal surface a 1 Hz frequency shift will be observed.

Is important to stress that, in order to apply correctly the Sauerbrey equation, some assumptions need to be fulfilled: first, the added mass should be small compared to the mass of the quartz sensor; second, the mass should be rigidly adsorbed to the surface of the sensor; third, the mass should be homogenously distributed over the surface of the sensor [68,69].

Sauerbrey equation has being used over the years. Later, around 1980, it was shown that QCM could also be applied under liquid environments [72–74]. Shortly after, it was observed that the interfacial adlayers under these conditions, viscoelastic films, did not follow the underlying assumptions behind Sauerbrey relation. The cumulative effects of the hydration, trapped water between the adsorbed films, and the softening of the adlayers contributed to the damping of the resonator oscillations. In many cases, the damping of the deposited films becomes so large that the linear relationship between the frequency and mass is lost [69,82]. These observations forced the QCM field to adapt and find a way to track the viscoelastic properties of the adsorbed films and create new theoretical models that could describe the behavior of these viscoelastic films.

2.3.1.3. QCM with energy dissipation monitoring

The introduction of QCM in liquids created the necessity to introduce dissipation (*D*) as an additional factor in order to quantify viscoelastic properties. Two main approaches were proposed to address the dissipation: the first approach is based on monitoring the decay of the quartz after a rapid excitation close to its resonant frequency [84]; the second approach

is based on the monitoring of the impedance [85]. Only the former method will be approach and explored in detail in this text since it became the standard method for the commercial QCM-D equipments. The impedance-based approach has been described in detail in numerous reviews [81,85].

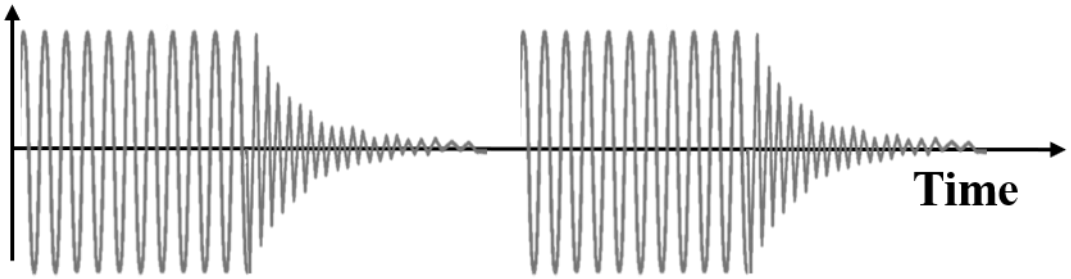

Figure 9: Representation of the oscillation amplitude sequences observed during a QCM-D experiment, as proposed by Kasemo and collaborators [84]. First, a rapid excitation is applied through a driving voltage with a frequency close to the quartz resonant frequency. Next, the driving voltage is switched off and the amplitude of the oscillator will decay freely in time as an exponentially dampened sinusoidal.

The basic principle of the methodology, proposed by Kasemo and collaborator, relies on periodically turning on and off the driving power supplied to the sensor. First, the quartz sensor is excited, by applying a driving voltage, with a frequency close to the quartz resonant frequency. Afterwards, the driving voltage is turned off and the amplitude of the free oscillator will decay, according to the properties of the oscillator and the medium in contact with the sensor, *figure 9*. As described by Kasemo and collaborators, the oscillator amplitude decays exponentially in time when the driving voltage is switched off [84], as expressed in *equation 4*:

$$A(t) = A_0 e^{t/\tau} \sin(2\pi f t + \alpha) \quad (4)$$

where A(t) is the amplitude of oscillation at time t, A_0 is the amplitude at t=0, τ is the decay time constant, f is the output frequency and α is the phase angle. The decay of the freely oscillating resonator is then fitted to the exponentially dampened sinusoidal wave (*equation 4*) to extract the output frequency (f). The output frequency is the difference between the quartz fundamental resonant frequency (f_0) and a constant reference frequency (f_r), as expressed in *equation 5*:

$$f = f_0 - f_r \quad (5)$$

From *equation 4* one can directly extract the output frequency that is then used to extract the energy dissipation, D, as expressed in *equation 6*:

$$D = \frac{1}{\pi f \tau} \quad (6)$$

The energy dissipation, a dimensionless quantity, can also be expressed as in *equation 7*:

$$D = \frac{1}{Q} = \frac{E_{Dissipated}}{2\pi E_{Stored}} \quad (7)$$

where Q is a quality factor, $E_{Dissipated}$ is the energy dissipated and E_{Stored} is the energy stored during a complete oscillatory cycle. The values of D reflect the physical nature of the interfacial adlayer on the sensor surface, with larger values of D indicating the formation of a soft and/or swollen film while small values of D indicate a rigid and dense film [69,82].

Through the application of the method developed by Kasemo and collaborators, it is possible to monitor, simultaneously, variations of f (Δf) and D (ΔD) over time [84]. Additionally, the QCM-D approach described above allows the acquisition of f and D at multiple harmonics (n=3,5,7,9..) of the resonant frequency in succession, with a time-resolution of millisecond [68]. The acquisition of multiple harmonics is essential to extract meaningful information, *e.g.* mass, thickness, density and viscosity, from the raw data through the application of suitable theoretical models (Section 2.3.1.4).

2.3.1.4. Viscoelastic modeling

The damping of the resonator oscillations and, the consequent loss of linearity from the Sauerbrey equation in liquid environments forced the development of new theoretical models to describe accurately the behaviour of viscoelastic films. In viscoelastic conditions, the frequency and dissipation responses are intrinsically dependent on the film mechanical properties such as density, viscosity, thickness and shear modulus (or elasticity) [82,86].

Voinova and coworkers proposed, in 1999, that the simplest way to consider the mechanical properties of viscoelastic films is to introduce shear viscosity coefficient, η, and shear elasticity modulus, μ, within the Maxwell's or Voigt's model [86]. The former model is applied for polymer solutions that exhibit a liquid-like behaviour, while the Voigt's model (also known as the Kelvin-Voigt model) is applied for polymers that conserve their shape and do not flow *e.g.* supported lipid bilayers. In this work, only a Voigt-based model will be approach and described, however detailed information about Maxwell's model can be found in the bibliography [87].

From Voinova description of the continuum mechanic behaviour of films at the fluid-solid interface, the mechanical properties of viscoelastic materials are related to the energy stored and energy loss trough dissipation processes, i.e. these properties are related to the amplitude of the stress applied and the relaxation processes of the material. While the

experimental condition influences the amplitude of the stress applied to the material, the relaxation rates are an inherent property of materials [86]. The viscoelastic film, surrounded by a bulk Newtonian fluid under no-slip conditions is characterized by a complex shear modulus (G), as expressed in *equation 8*:

$$G = G' + iG'' = \mu_f + i2\pi f\eta_f = \mu_f(1 + i2\pi f\tau_f) \quad (8)$$

where G′ is the storage modulus and G″ is the loss modulus, μ_f is the elastic shear modulus, η_f is the shear viscosity and τ_f is the intrinsic relaxation time of the film [69,82,86]. One can calculate the relaxation time of a given film trough the ratio between η_f and μ_f, as expressed in *equation 9*:

$$\tau_f = {\eta_f}/{\mu_f} \quad (9)$$

Under these conditions, the values of Δf and ΔD can then be obtained through *equation 10* and *equation 11*, respectively:

$$\Delta f \approx -\frac{1}{2\pi\rho_q t_q}\left\{\frac{\eta_l}{\delta_l} + \sum_{f=1,2}\left[t_f\rho_f\omega - 2t_f\left(\frac{\eta_l}{\delta_l}\right)^2\frac{\eta_f\omega^2}{\mu_f^2+\omega^2\eta_f^2}\right]\right\} \quad (10)$$

$$\Delta D \approx \frac{1}{2\pi f\rho_q t_q}\left\{\frac{\eta_l}{\delta_l} + \sum_{f=1,2}\left[2t_f\left(\frac{\eta_l}{\delta_l}\right)^2\frac{\mu_f\omega}{\mu_f^2+\omega^2\eta_f^2}\right]\right\} \quad (11)$$

where ρ_q and t_q are the density and thickness of the quartz crystal sensor, η_l and δ_l are the density of the liquid and viscous penetration depth of the shear wave in the bulk liquid, ω is the angular frequency of the oscillation and t_f, ρ_f, μ_f and η_f are the thickness, density, shear elastic modulus and shear viscosity of the adsorbed film [69,82,86]. From this model, physical parameters such as the hydrodynamic thickness, shear viscosity and shear modulus can be calculated through the fitting of Δf and ΔD, obtained at different overtones, over a period of time.

2.3.2. Ellipsometry

Ellipsometry is an optical technique used for the characterization of physical properties of materials, surfaces and interfaces. This technique is a powerful tool for probing relevant parameters of materials such as refractive index, thickness and roughness.

The basic principle for ellipsometric analysis is based on Fresnel reflection equations [88]. In this technique, a monochromatic polarized light beam is shined into a medium and the change of polarization in the reflected wave is recorded through an analyzer. These

polarization changes can be measured through the ratio between the complex reflection coefficients, as represented in *equation 12* [88,89],

$$\rho = {R_p}/{R_s} = tan\Psi\, e^{i\Delta} \quad (12)$$

where R_p and R_s are the complex Fresnel reflection coefficients for the polarized light parallel and perpendicular to the plane of incidence, respectively. Ellipsometry data is expressed through the ellipsometric angles Δ and Ψ, as expressed in *equation 12*. The ellipsometric angles provide information regarding the amplitude changes, Ψ, and phase changes, Δ, between the incident and reflected beam [89,90].

Ellipsometric measurements offer a wide variety of attractive capabilities. This method is non-invasive, fast and automated. Additionally, since it is based on the ratio of two values this method is highly accurate and reproducible, without the need to introduce reference materials [89,90]. Since the measurements of Δ and Ψ are highly accurate, ellipsometry can resolve thickness changes down to the sub-Å scale [88].

Ellipsometry is an indirect method meaning that the experimental data provided from the measurement of the ellipsometric angles, Δ and Ψ, does not provide direct information about the material properties. Optic models, accurately describing the experimental set-up, must be built and the modelled generated data is compared with the experimental data. The parameters (*e.g.* thickness, refractive index) of the optic models are then optimized until the fitting between experimental and modelled data is maximized. In this sense, the accuracy of the data provided by ellipsometry is directly dependent on how faithfully the optical models describe the optical properties of the experimental sample.

Ellipsometry is commonly used in lipidic membrane systems to address many relevant aspects such as phase morphologies and transitions [91,92], properties and kinetics of SLBs formation [93,94], protein-lipid interactions [95] and receptor-ligand interactions [96,97].

2.3.3. Small-Angle Neutron Scattering

The small-angle scattering of radiation comprises a widely range of techniques often used in the analysis of disperse particles, with application in areas like polymers, colloids or biological macromolecules, to name a few. These scattering phenomena can be performed with light, X-ray or neutrons, and all describe the scattering of radiation from a particle [98]. The theoretical description of the scattering theory will not be addressed in this topic and

can be found in many textbooks [99,100]. In this topic, the features of small-angle neutron scattering (SANS) and its advantages in the study of biological systems will be addressed.

In SANS experiments a beam of neutrons is shined into a sample and the incoming neutrons are elastically scattered when they interact with the sample, which can be a liquid (aqueous solutions) or a solid (crystals or powders) [99]. During the elastic scattering, the total kinetic energy of the scattered neutrons is conserved and its direction of propagation is shifted. The shifted neutrons are then registered in a detector giving rise to a scattering pattern. The resulting scattering patterns are then modelled and useful information about shape, size and orientation can be extracted [99,100].

Even though the small-angle scattering of x-ray and neutron share identical principles, these two types of small-angle scattering techniques are fundamentally different due to the properties of the neutrons and photons shined during SANS and SAXS analysis, respectively. The interaction of neutrons and photons with matter is inherently distinct. While neutrons are scattered by interaction with the nuclei, in SAXS the photons interact with the electronic cloud of the nuclei [100]. In fact, one of the main advantages of SANS arises from the different scattering cross-sections of elements, with the most prominent difference being observed between hydrogen and its deuterium isotope. The scattering length of these two elements is quite distinctive which enables the possibility of contrast variations [101].

Indeed, the contrast is a very important property in any scattering experiment and is responsible for distinguishing the material from the matrix where the former is inserted. In SANS, the contrast is produced by mixing components with different scattering length densities (SLD or ρ), often achieved by replacing one atom by one of its isotopes [102]. The most used contrast variation is performed with hydrogen and deuterium. Contrast variations have many applications [103] *e.g.* deuterium substitution can provide valuable information about hydrogens which are not "visible" to x-rays; specific match points (ratios of H2O and D2O) can be set to eliminate the presence of some constituents of the sample (e.g. DNA or proteins).

SANS has been used to study different aspects of bioinspired membrane-based systems such as characterization of liposome formulations[104] and protein-liposome interaction [105].

3

Materials and Methods

3. Materials and Methods

3.1. Materials

3.1.1. Lipids

Across this work different biomimetic models were built in order to recreate an environment similar to the natural lipid environment of the plasmatic membrane. *Table 1* contains the lipids used throughout this work with their respective molecular weights. They were supplied by Avanti Polar Lipids Inc. (Alabaster, USA) and, stored at a temperature below -20 ºC until utilization. All the lipids were used as received without no further purifications since their products already have a purity higher than 99%. The lipids, in powder, were then dissolved in chloroform ($CHCl_3$) until a final concentration of 1,0 mg/mL was reached and stored on the freezer, at a temperature below -20 ºC, after each use. *Figure 10* shows the molecular structures of these lipids.

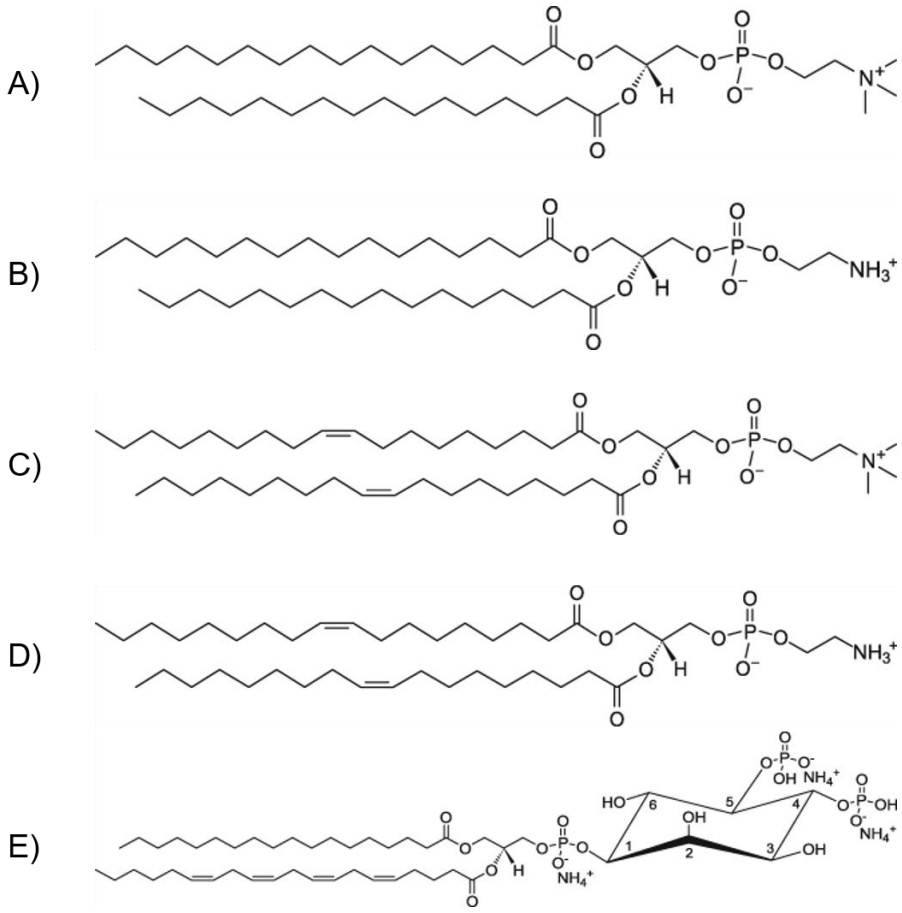

Figure 10: Molecular structure of the natural lipids used to build the biomimetic systems employed across this work: A) DPPC; B) DPPE; C) DOPC; D) DOPE; E) PIP2.

Table 1: Summary table compiling lipid name, commonly abbreviation and molecular weight of each of the lipids used across this work. The molecular structure of the lipids listed below is shown in *figure 10*.

Lipid name	Commonly known as	Molecular Weight, g/mol
1,2-dipalmitoyl-sn-glycero-3-phosphocholine	DPPC	734.039
1,2-dipalmitoyl-sn-glycero-3-phosphoethanolamine	DPPE	691.959
1,2-dioleoyl-sn-glycero-3-phosphocholine	DOPC	786.113
1,2-dioleoyl-sn-glycero-3-phosphoethanolamine	DOPE	744.034
L-α-phosphatidylinositol-4,5-bisphosphate	PIP2	1096.385

3.1.2. Cargo Molecules

The cargo molecules, TGN38 and CD4 (*table 2*), were kindly provided by Dr. David J. Owen from the University of Cambridge. A brief description of the synthesis process is provided here and more detailed information can be found elsewhere [31–33,38,40].

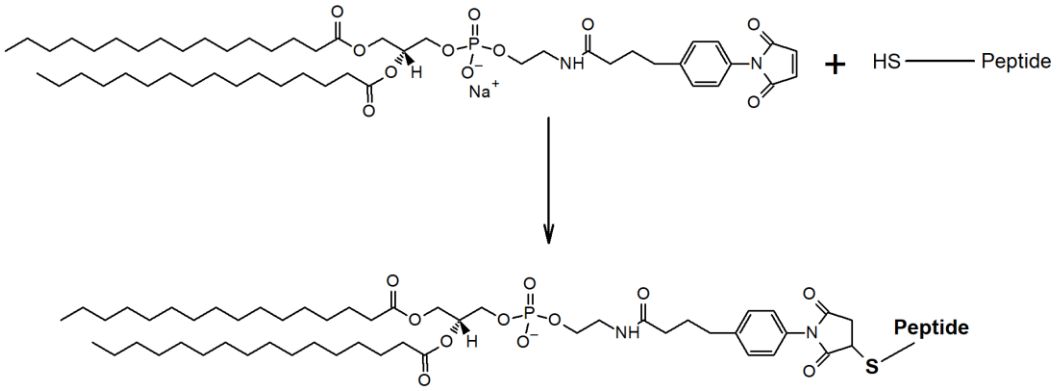

Figure 11: Schematic representation of the synthesis route in the conjugation of a peptide sequence with a synthetic lipid. The conjugation is achieved through the reaction of the cysteine, present in the N-terminus, with the maleimide group of 16:0 MPB PE lipid.

Peptides sequences, containing the sorting recognition motifs from the cytoplasmatic tails of TGN38 and phosphorylated CD4, were synthesized with a cysteine moiety in the amino-terminal. The quality of the produced peptides was evaluated with mass spectrometry and reverse-phase chromatography. After reaching the quality criteria desired for the peptides, a conjugation reaction was performed to covalently tag the peptides to a synthetic lipid, 1,2-Dipalmitoyl-sn-Glycero-3-Phosphoethanolamine-N-[4-(p-maleimidophenyl) butyramide] commonly known as 16:0 MPB PE, as represented in *figure 11*. The bioconjugation was achieved through a Thiol-Maleimide Michael addition reaction, where

the cysteine moiety, present in the N-terminus, was covalently attached to the maleimide group of 16:0 MPB PE lipid. The final solutions of the lipopeptide were collected after extraction, dried under nitrogen, resuspended in chloroform:methanol (2:1) and stored at -20 ºC.

Table 2: Peptide sequences of TGN38 and CD4. The peptides, containing the sorting recognition motifs, were tagged with a synthetic lipid, 16:0 MPB PE. The respective molecular weight of each peptide, before and after conjugation with the synthetic lipid, is presented. * Represents the phosphorylated residue of CD4.

Cargo	Aminoacid sequence	Peptide Molecular Weight, g/mol	Conjugated (Lipid+Peptide) Molecular Weight, g/mol
TGN38	CKVTRRPKASDYQRL	1821,1	2776,3
CD4	CHRRRQAERM[S*]QIKRLLSEK	2526,0	3481,2

3.1.3. Adaptor Protein 2

The AP2 protein (*table 3*) used across this work were kindly provided by Dr. David J. Owen from the University of Cambridge. Detailed description of the synthesis and purification processes can be found elsewhere [35,106,107].

Table 3: Table summarizing different components of AP2 with the respective structure PDB ID. AP2 conformations, open and close, have already been atomically characterized (mutant AP2-core) by X-ray crystallography. Additionally, the atomic characterization of both α- and β2-adaptin appendages has also been addressed through X-ray crystallography. The structures PDB ID and respective molecular weights are presented. Nevertheless, it is important to stress that the atomic characterization of full-length AP2 has not yet been performed, due to difficulties in growing good quality crystals. The overall weight of full-length AP2 was considered as described in the bibliography [29]. The total weight of AP2 full length is comprised by the AP2-core, α- and β2-adaptin appendages and the polypeptide chains connecting the AP2-core with each of the adaptin appendages. *AP2 full length represents the AP2 expressed with core together with α and β2-adaptin appendages.

Protein	PDB Entry	Molecular Weight, kDa
AP2-Core : Open	2XA7	205
AP2-Core : Close	2VGL	203
β2-Adaptin Appendage	1E42	29,06
α-Adaptin Appendage	1B9K	26,99
AP2 full length *	x	287

The AP2 used on this work was expressed with its core and with both α and β2-adaptin appendages (or ears). Reports found on bibliography also use a mutant version of AP2, called AP2-core [32,33]. In fact, both proteins are very similar and their only difference is

that the AP2-core does not have the α and β2-adaptin appendages. Despite this, both proteins possess the specific AA sequence motifs that interact with PIP2, TGN38 and CD4.

3.1.4. Buffer solutions

Throughout this work, two different buffer solutions were used: HKM and HKT buffer. The same principles were followed to prepare both buffers. First, all the materials (*e.g.* glass bottles, volumetric flask and glass beakers) used during the preparation were thoroughly cleaned with deionized water and detergent. Then the respective chemicals composing each buffer were weighted and mixed. After homogenization of the solution, the pH was measured and carefully set to its target value. The buffer solution was then filtered, into a previously cleaned glass bottle, through a commercial vacuum filtration system. To finalize, the buffer was sonicated with controlled temperature, in order to avoid heating, and then isolated with parafilm and kept in the fridge at 4 ºC until utilization. HKM buffer was 25 mM HEPES, 5 mM Magnesium Acetate ($Mg(CH_3COO)_2$) $4H_2O$, 125 mM Potassium Acetate (CH_3CO_2K) and 1 mM DL-Dithiothreitol (DTT). HKT buffer was 25 mM HEPES, 125 mM Potassium Acetate (CH_3CO_2K) and 1 mM DL-Dithiothreitol (DTT). The pH of these buffer solutions was adjusted to pH ~ 7.20 ± 0.05 .

3.1.5. Silicon wafer cleaning and functionalization

The unused silicon wafers were cut with a pen-style scribe, equipped with a diamond tip, in squared shapes of 4 cm^2. For the cleaning, the cut squares were placed in a 3D printed support inside a beaker. The silicon squares were then sonicated for 10 min. with acetone, ethanol, water and ethanol, sequentially. The sensors were then dried under a continuous stream of nitrogen.

For the functionalization, the silicon squares were placed in the UV-ozone cleaner (ProCleaner™ Plus, BioForce Nanosciences, USA) for 30 minutes.

The cleaning and functionalization of the silicon squares were always performed right before the Langmuir depositions.

3.2. Methods

3.2.1. Liposome Preparation

The liposomes were prepared according to the thin film hydration protocol [108]. The lipids, previously dissolved in chloroform, were aliquoted and mixed into a glass vial,

according to the desired molecular ratios (*table 4*). The volatile solvent was evaporated under a continuous stream of argon, forming a uniform thin dry lipid film on the glass vial walls. The glass vials were left on the vacuum pump overnight (~10-12 h) to ensure evaporation of any remaining solvent. The resulting lipid film was hydrated overnight at room temperature with end-over-end rotation in a mixture of water:buffer (8:2). The hydration step leads to the formation of MLVs, with nonhomogeneous size and lamellarity distribution.

Since the size and lamellarity profiles of the newly-formed liposomes were not homogenous and uniform, additional processing was necessary to achieve a uniform and monodisperse unilamellar liposomes. The liposome solution containing MLVs was subjected to 5-10 successive freeze-thaw cycles with liquid nitrogen and ice, respectively. Next, the vesicle solution was tip sonicated (Sonopuls HD 2200, Bandelin, Germany), with a titanium probe (MS73 with microtip of 3 mm), for 15-20 min. with repeated on/off pulses of 2 s and 3 s, respectively, and power amplitude of 20%. The tip sonication was performed with the glass vial, containing the sample, embedded into an ice bed to avoid heating. The vesicle solution was then manually extruded through a commercial mini extruder kit (Avanti Polar Lipids, Alabama, USA) assembled with a polycarbonate membrane (Whatman Inc., Clifton, NJ) with 100 nm pore size. To obtain monodisperse LUVs with size ranging 100 nm, the extrusion cycles were repeated 15-25 times.

Table 4: Lipid composition, in molar percentages, of the different liposome vesicles used for the formation of SLBs and study of AP2 binding.

Lipid Mixtures	DOPC	DOPE	PIP2	TGN38	CD4
DOPC:DOPE	80,0	20,0	-	-	-
DOPC:DOPE:PIP2	70	20,0	10,0	-	-
DOPC:DOPE:TGN38	76,5	20,0	-	3,5	-
DOPC:DOPE:CD4	76,5	20,0	-	-	3,5
DOPC:DOPE:PIP2:CD4	66,5	20,0	10,0	3,5	-
DOPC:DOPE:PIP2:TGN38	66,5	20,0	10,0	-	3,5

The size of the lipid vesicles solution was monitored through dynamic light scattering (Zetasizer Nano ZS90, Malvern Instruments, U.K.). The measurements were performed with the temperature set at 20 ºC and the scattering angle at 90º. All the studies were performed with vesicles which exhibited monodisperse size distribution and a diameter ranging 100 nm.

Throughout the development of this work, different variations of this method were used in order to overcome unexpected aggregation phenomena (*Appendix B*) or to optimize the time/quality of preparation of the liposomes (*Appendix C*).

3.2.2. Langmuir Blodget/Schaefer Deposition

A Langmuir-Blodget trough (NIMA 611, Nima Technology Coventry, U.K.) was used to assemble all the SLBs samples produced, across this work, through LB/LS depositions. The NIMA 611 trough and barriers, available at Institut Laue-Langevin, are built with PTFE material. This highly hydrophobic polymer prevents any lipid molecules to get attached either to the surface of the trough or the compression barriers. Additionally, this material is suitable to be cleaned with volatile solvents, removing any debris or contaminants from the trough surface.

Before starting the experiments, the trough surface and barriers were meticulously cleaned. The cleaning process is extremely important and should be carried with the utmost caution since any debris or contamination on the surface of the trough can lead to incorrect surface pressure readings. The trough was first wetted with deionized water, followed by a scrub with a tissue moisturized with soap. Next, the trough was completely filled and emptied, sequentially, with deionized water to remove the soap. Then the through was scrubbed with a tissue moisturized with ethanol followed by a water wash. The same steps were performed for chloroform and ethanol, again. After carefully washing the trough with deionized water to remove any remaining solvents, the trough was filled with deionized water as the final subphase. The same steps, described above, were executed to clean the barriers.

Once all the components were cleaned and properly assembled, the solid substrate (previously cleaned) was dipped into the subphase with its functionalized surface oriented parallel to the barriers. The lipid solution in chloroform was spread in the air-water interface with an appropriate Hamilton syringe. After spreading the lipids, the system was left to rest for 20-30 minutes, while chloroform evaporated. The surface pressure was then targeted to 35 mN/m and the compression speed set to 10 cm^2/min. The barriers gradually compressed the newly-formed lipid monolayer until the target surface pressure of 35 mN/m was achieved. Once the target surface pressure of 35 mN/m was achieved, the system was left to rest for 10 minutes and then the barriers were slowly opened, decompressing the monolayer.

A new target surface pressure of 30 mN/m was set and the barrier compressed the monolayer until this value was achieved. All the LB/LS depositions presented in this work were performed at 30 mN/m.

The LB deposition was performed by moving upward the solid substrate with a constant speed of 3 mm/min. Simultaneously, the surface pressure was kept constant at 30 mN/m, to assure a homogenous adherent layer. Once the upward movement of the solid substrate was completed, the first lipid monolayer was deposited into the solid surface, with the lipid heads pointing into the surface of the silicon block. For the second monolayer, a similar procedure was executed (LS deposition). First, the surface pressure was set to a constant value of 30 mN/m. Next, the solid support, previously functionalized with the first monolayer, was assembled into a home-built manual dipping mechanism. Contrary to the LB deposition, in LS deposition the solid support is oriented with its surface parallel to the air-water interface. Since this mechanism is manually operated, the silicon block had to be precisely aligned with the air-water interface. Then the silicon was carefully moved into the lipid monolayer at the air-water interface by gently unscrewing the manual dipping mechanism. The bilayer is formed when the solid support meets the monolayer spread at the air-water interface. The solid substrate was then laid in a special holding cell, previously placed underneath the subphase.

3.2.3. QCM-D

The QCM-D measurements were performed in the commercial Q-Sense E4 Instrument (Q-Sense, Biolin Scientific AB, Sweden). All the measurements were performed with a 5 MHz quartz sensor coated with SiO_2, identified by the reference QSX 303 (Q-Sense, Biolin Scientific AB, Sweden).

Before starting the experiments, the SiO_2 sensors were thoroughly cleaned. The sensors were placed in the sensor holder provided by Biolin Scientific and then placed inside a glass beaker. The sensors were then sonicated during 10 min. with chloroform, acetone, ethanol and water, sequentially. The sensors were then dried under a gentle stream of nitrogen and placed in the UV-ozone cleaner (ProCleaner™ Plus, BioForce Nanosciences, USA) for 20 minutes. After surface oxidation, the sensors were rinsed with water and dried under a smooth nitrogen stream. Once the crystals were cleaned, they were immediately assembled inside the flow module. Special care was taken while placing the sensors on the

flow module, assuring that the electrodes were correctly placed and the O-ring sealing was tight.

After the assembling of each sensor on the respective flow module, the peristaltic pump (Multichannel Peristaltic Pump IPC-N 4, Ismatec, Switzerland) was turned on with pure ethanol, followed by water for 10 min. each at a rate of 0.5 mL/min. This step was performed to clean all the tubings from any possible debris or contaminants. Once properly cleaned, the pump flow rate was changed to 0.1 mL/min and the buffer was added while the fundamental frequency (n=1) and six overtones (n=3,5,7,9,11 and 13) were recorded at 20 ºC. The system was left equilibrating until a stable baseline was recorded *i.e.* until the frequency and dissipation levelled-off and kept a constant signal for at least 5 minutes. After measuring a stable baseline, a 0.1 mg/mL solution of monodisperse unilamellar vesicles with size ranging 100 nm was loaded into the flow module at a rate of 0.1 mL/min, while Δf and ΔD were recorded in real-time. The flow was stopped and the vesicles were left incubating for 20-40 minutes, allowing the fusion process between the vesicles and SiO_2 sensor to occur. After the formation of SLB and plateau of the signals, the buffer was flowed through the system to differentiate between the mass that is "strongly" coupled to the sensor and the partially or weakly bound material, washing out the last one. The same procedure was performed for the protein analysis, first loading the protein and, after stabilization of the signal, washing the system with the buffer to remove any excess or uncoupled material.

The QCM-D data was acquired with the software Q-Soft401 (version 2.6.1, Q-Sense, Biolin Scientific AB, Sweden) and data was analysed with Q-Tools3 (version 3.0.10, Q-Sense, Biolin Scientific AB, Sweden). The QCM-D data presented across this work was normalized to the response of a 5 MHz sensor (f_n/n and D_n/n). The overtone n = 3 was chosen as a representative overtone in all presented QCM-D plots.

3.2.4. Ellipsometry

The ellipsometer measurements presented across this work were performed on a Picometer Light ellipsometer (Beaglehole Instruments, Kelburn, New Zealand). The ellipsometer, available at Institut Laue Langevin, is equipped with a He-Ne laser with λ = 632 nm. This instrument is able to perform two different types of measurement: variable angle of incidence (AOI), from 35º - 90º; and fixed angle over-time. All the measurements carried out in this work were perform with variable angle of incidence.

The silicon blocks functionalized with the lipid bilayer, through LB/LS deposition, were analysed by ellipsometry. Two different set-ups were explored. In the first experimental set-up, lipid monolayers were measured in the air, while in the second lipid bilayers were measured, with the help of optic guides, in a special cell filled with deionized water. For the first experimental set-up, the AOI was set to 40º - 85º and the ellipsometric angles Psi (ψ) and Delta (Δ) were recorded with a step of 0.5º. For the second experimental set-up, the AOI was set to 35º - 63º and the ellipsometric angles Psi (ψ) and Delta (Δ) were recorded, with the custom-made optic guides installed, with a step of 0.5º.

The data analysis was performed with slab models built following the same principles as described by Maestro and collaborators [109].

3.2.5. Small-Angle Neutron Scattering

The SANS measurements were performed at the D11 instrument, available at the Institut Laue-Langevin, Grenoble, France. The analyzed samples were placed inside a circular quartz cell with 1mm thickness. The data was recorded with sample to detector distances of 1.4 m, 8 m and 39 m, neutrons wavelength of 4.5 Å and a constant temperature of 25 ºC. This choice of parameters allowed data collection over a Q-range between 0.0017 Å and 0.59 Å.

The data plot and analysis were performed with the software SasView (version 4.2.2).

4

Results and Discussion

4. Results and Discussion

4.1. Ellipsometric characterization of Langmuir supported films

Langmuir supported lipid monolayers and bilayers were produced as described in Section 3.2.2. The lipid composition of the Langmuir supported films was constituted by DPPC and DPPE lipids (*figure 10*, Section 3.1.1). These lipids were employed as an alternative to DOPC and DOPE lipids used for liposome formulation, due to their unsaturated aliphatic chains which are known to be less susceptible to oxidation or hydrolysis phenomena.

The ellipsometric characterization of the Langmuir supported films was carried out envisioning two main aims: sample preparation characterization and protein adsorption characterization.

The first aim of ellipsometric characterization (*sample preparation characterization*) was assessing the viability of SLBs, produced by LB/LS deposition techniques, for ssNMR studies. Solid-state NMR studies of proteins often rely on extended stacks of oriented bilayers, prepared by vesicle fusion on mechanical supports [110,111]. As described before (Section 2.2.2), LB/LS deposition techniques offer a set of appealing characteristics, in comparison with vesicle fusion, for the production of SLBs.

The second aim (*protein adsorption characterization*) was using ellipsometric characterization of AP2 adsorption and binding into SLBs to complement the observations from QCM-D (Section 4.3).

The ellipsometric characterization of the Langmuir supported films was achieved by means of two different experimental set-ups: air-silicon interface, for monolayer measurements; water-silicon interface, for bilayer measurements.

4.1.1. Air-silicon interface: supported lipid monolayers

The ellipsometric angles Δ and Ψ were acquired as a function of the angle of incidence (AOI). The angle range was set between 40 – 85º, with a step increment of 0.5º. Prior to any measurement, the silicon wafers were thoroughly cleaned and functionalized as described in Section 3.1.5. The average thickness for the SiO_2 layer of the silicon support post-cleaning and post-functionalization is presented in *figure S1 – Appendix A*. Since the functionalized silicon support exhibited a SiO_2 layer thickness variance of approximately ±

2 Å, the measurements of the monolayer were performed together with "naked" silicon supports as a control for the SiO_2 layer thickness. Both silicon support, for monolayer and control, were extracted from the same bulk silicon wafer. The cleaning and functionalization steps were performed simultaneously on each silicon supports, to maximize the homogeneity between them. This rationale was kept across all measurements.

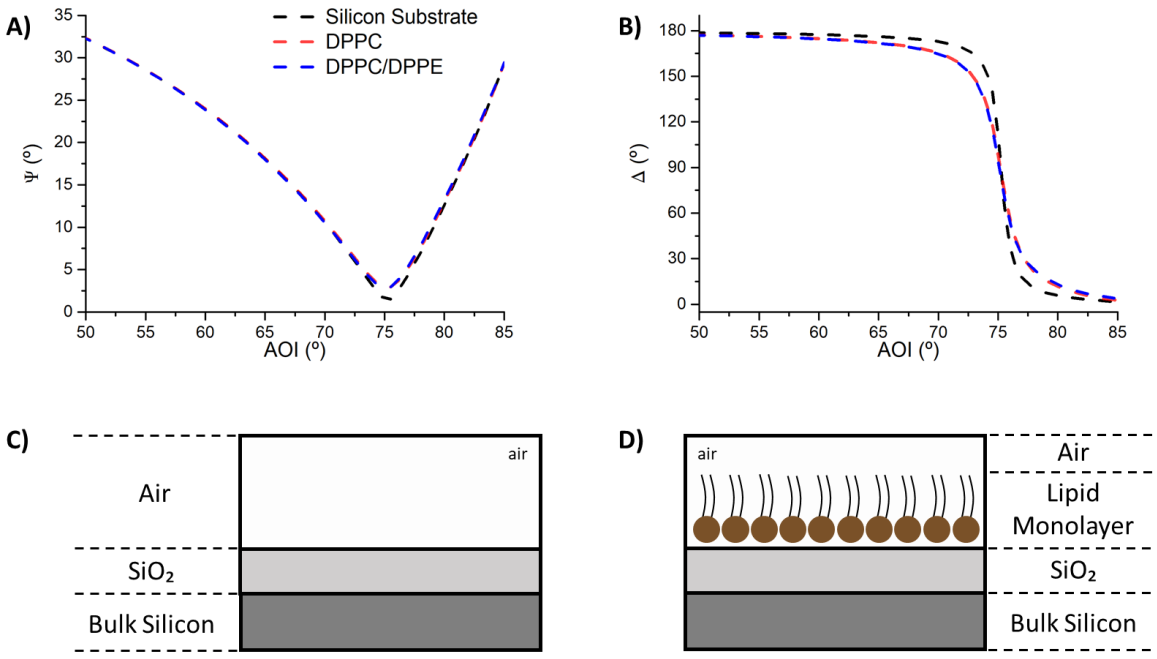

Figure 12: Experimental data acquired for Ψ (A) and Δ (B) in function of the angle of incidence (AOI). From the comparison of both ellipsometric angles vs. AOI, Δ clearly exhibits higher sensitivity to film changes than Ψ. The higher sensitivity to film changes occurs near the Brewster angle which for the case of air-silicon interface occurs approximately at 75.5°. In the bottom section of the image, a schematic representation of the optic models used for calculation of SiO_2 layers thickness (C) and lipid monolayer thickness (D) is shown.

The experimental ellipsometric angles acquired in function of the angle of incidence (AOI) are presented in *figure 12A,B*. From the comparison of the plots *Ψ vs. AOI* and *Δ vs. AOI* one can observe a clear sensitivity discrepancy to film changes between both ellipsometric angles. In fact, Δ exhibits a higher sensitivity to film changes compared to Ψ. This phenomenon is often observed in the ultrathin film regimen [91,112]. Under these conditions, almost no detectable changes are observed on the ellipsometric angle Ψ due to the small thicknesses of the films in comparison to the light beam wavelength. Nevertheless, the sensitivity of the ellipsometric measurement can be significantly increased by precisely choosing the angle of incidence [112]. Indeed, the sensitivity to changes in the adsorbed film is dramatically increased in the regions close to the Brewster angle, which for the air-silicon

interface occurs approximately at 75.5º. The recorded data shows clear differences in the plotted ellipsometric angles between the functionalized silicon substrate and for the lipid monolayers. These differences are attributed to the presence of the lipid monolayer which increases the overall thickness of the whole complex. On the other hand, since both monolayers share very similar optical properties and thicknesses, the overall trend of both is very identical. Despite the ellipsometric plotted angles for both monolayers seem to overlap, they carry a cumulative angle variance of 56.6º in the case of Δ and 11.7º in Ψ, which is translated in a mean-variance of 0.6º and 0.1º for each point recorded, respectively. This variance highlights the presence of different optical properties and/or thicknesses among both monolayers.

As previously described in Section 2.3.2, ellipsometry is not a direct method and, therefore, optic models need to be built to extract the structural properties of the film analysed. The optic models used for the Langmuir supported monolayers are shown in *figure 12C* and *12D*. The models were created as a three and four slab models. The three-slab model (figure 12C) created to estimate the thickness of the SiO_2 layer in the bare silicon support, was composed of three layers: the environment, *air*; the "adsorbed" film, *SiO_2*; and the substrate, *bulk silicon*. In this model, the environment and substrate were treated as a continuum ($d = \infty$) with n = 1 for air, and n = 3,8815 and k = 0,0195 for the bulk silicon substrate [113], where n and k represent the refractive index and the extinction coefficient respectively. The refractive index of the SiO_2 layer was considered n = 1,457 [114]. For the four-slab model an additional layer was included to account for the lipid monolayers. The same approach described before was applied for this model, with the only difference being that the SiO_2 layer was fitted with the thickness calculated from the three-slab model (*figure 12C*).

As described before, bare silicon wafers were measured to estimate the thickness of the SiO_2 layers on the silicon wafers used for the Langmuir deposition of DPPC and DPPC/DPPE monolayers. The determined SiO_2 layer thickness on the silicon wafers for the Langmuir deposition of DPPC and DPPC/DPPE monolayers was 24.7 Å and 23.1 Å, respectively. These values were then integrated into the four-slab model.

In the ultrathin film regimen, both the refractive index and thickness are entangled parameters and, therefore, impossible to be calculated simultaneously. As a rule of thumb, it is considered that these parameters can only be estimated together for film thicknesses

bigger than 15 Å [115], which is 5 to 6-fold bigger than the thicknesses expected for lipid monolayers. However, this limitation can be overcome if one of these two parameters (refractive index or thickness) is known beforehand or determined by alternative methods. Kienle and collaborators reported the determination of the refractive index for DPPC and DPPE monolayers produced by Langmuir-Blodgett on mica and measured by multiple-beam interferometry in dry air [116]. In this report, the refractive index was determined 1.485 ± 0.007 for DPPE monolayers and 1.478 ± 0.006 for DPPC monolayers. For the DPPC monolayer the refractive index considered in the four-slab model was the same as reported by Kienle and collaborators, while for the DPPC/DPPE monolayer the refractive index considered was 1.480 due to the 8:2 mol ratio of DPPC:DPPE used for the monolayer production.

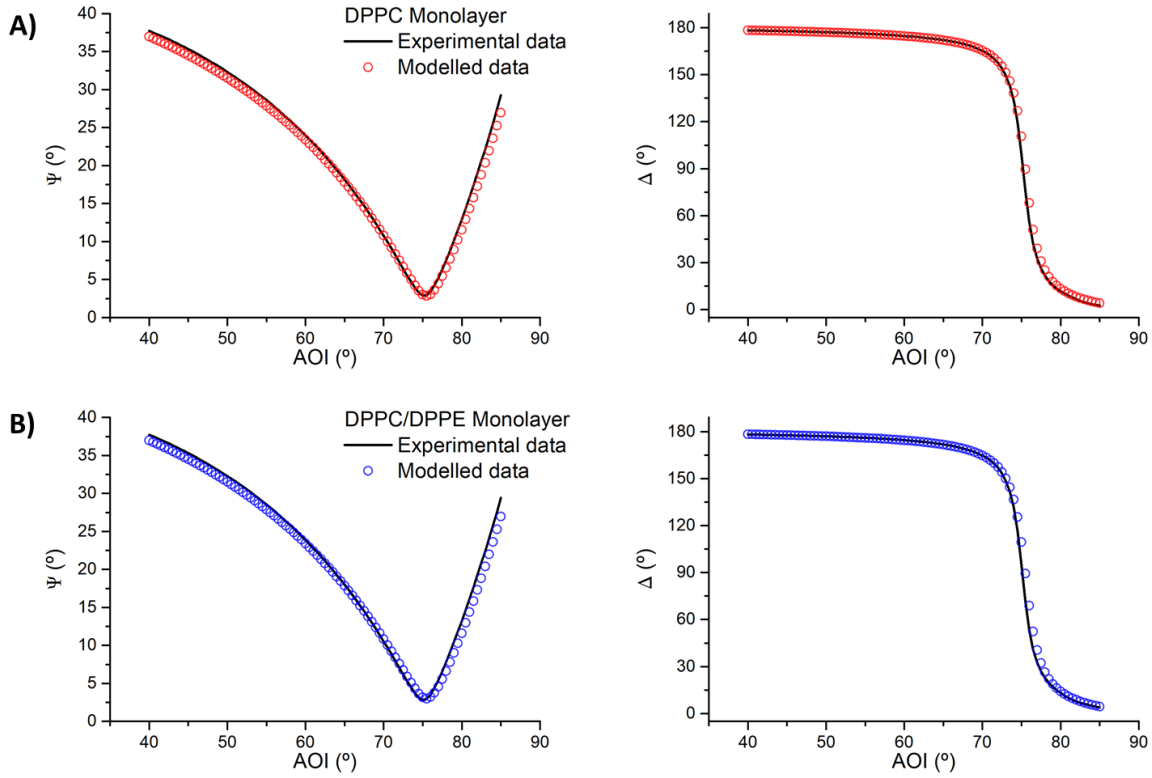

Figure 13: Experimental and modelled data for DPPC (A) and DPPC/DDPE monolayer (B). The experimental ellipsometric data are shown as solid black lines and the modelled data is shown as coloured circle dots. The overall fitting between the experimental and modelled data is rather good, with MSE of 2.4 and 3.5 for the DPPC and DPPC/DPPE monolayer, respectively. The calculated thicknesses for DPPC and DPPC/DPPE monolayers were 24.8 Å and 25.9 Å, respectively.

The modelled and experimental data for the Langmuir supported monolayers is presented in *figure 13*. The fitting between the modelled (circle dots) and experimental data (solid line) is good with a χ_R^2 of 9.6 for DPPC monolayer and 13.9 for DPPC/DPPE

monolayer. Additionally, the MSE factor (a quality estimator often used in ellipsometry) was 2.4 and 3.5 for DPPC and DPPC/DPPE monolayers, respectively, which is indicative that the models are suitable and accurately translate the experimental data [88]. From the four-slab model, the determined thickness for the DPPC lipid monolayer was 24.8 Å and 25.9 Å for the DPPC/DPPE monolayer.

The calculated thicknesses obtained for the lipid monolayers are relatively higher than those reported by Kienle and collaborators, which were found to be 23.9 ± 0.5 Å for DPPC monolayers and 25.5 ± 0.6 Å for DPPE monolayers in dry air. Both experiments, described here and performed by Kienle and coworkers, were performed in highly similar conditions with the two main differences being the surface pressure and solid support used for the Langmuir-Blodgett deposition. Even though the experiments carried by Kienle and collaborators were performed with a relatively higher surface pressure of 45 mN/m, compared to the 30 mN/m of this work, this fact alone does not explain the difference of thicknesses observed since higher surface pressures lead to higher molecular packing and increased thicknesses. Indeed, these thickness differences are likely to be dependent on the solid support and respective hydration layer between the lipid heads and substrate. A similar study performed with DPPC monolayers supported in silicon substrate at 30 mN/m reported a thickness of 25 Å, which is consistent with the value presented in this work for DPPC monolayers [117].

The increased thickness of DPPC/DPPE monolayer, compared to DPPC monolayer, is concordant with the expected results. DPPC lipids are known to assume a tilted position in the monolayer structure and, therefore, exhibit shorter monolayer thicknesses [109]. On the other hand, DPPE lipids yield monolayers with higher structural organization due to their increased molecular packing, giving rise to thicker lipid monolayers [116]. Even though the DPPC/DPPE monolayer used is only composed by 20% of DPPE lipids (molar percentage), it is rationalized that the mixing of DPPC and DPPE lipids in the same monolayer leads to an increased packing density (see *figure S2 – Appendix A*) and increased monolayer thickness compared to DPPC monolayer.

While the reported values on this work are in good agreement with other results presented in the bibliography, it is important to emphasize that only one point of the surface was evaluated. Indeed, this is a major limitation of these measurements because the lack of repetitions can lead to misleading results due to surface inhomogeneities.

4.1.2. Water-silicon interface: supported lipid bilayers

In order to measure the thickness of SLBs produced through Langmuir deposition techniques a similar approach was employed. Since SLBs need to be measured in a hydrated environment [118], the experimental set-up was slightly customized to provide the capability to perform the ellipsometric measurements in-situ. Optic guides were installed to drive the incident beam directly to the water-silicon interface to avoid the reflection at the liquid/air interface. The SLB was placed in a 3D printed support cell full of water as illustrated in *figure 14*.

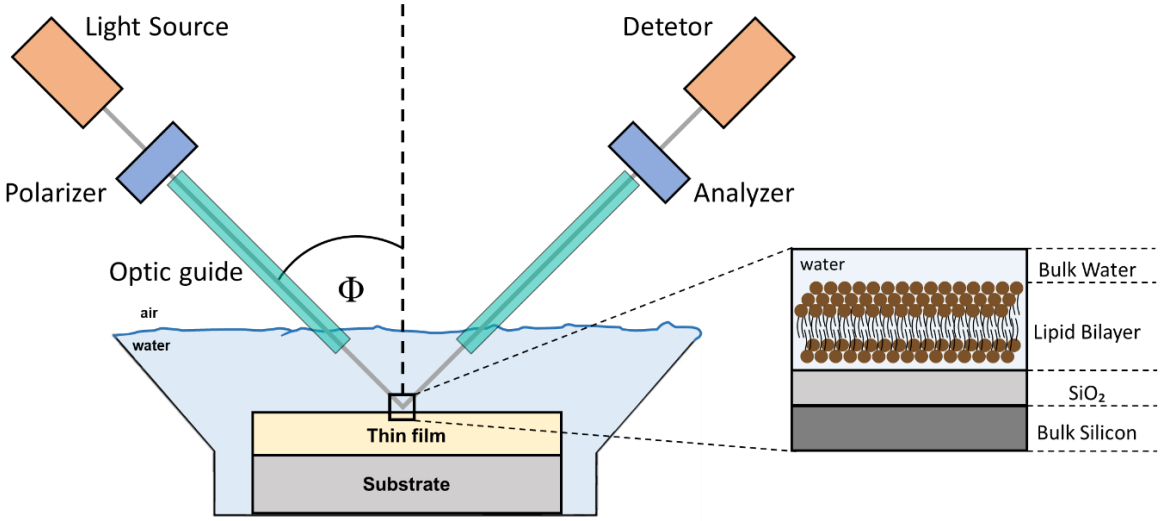

Figure 14: Schematic representation of the experimental set-up used for the water silicon interface measurements (left) and the respective four-slab optic model built to extract the structural properties of the SLB film (right). For the experimental set-up, shown on left, optic guides (green) were installed coupled to the arms of the ellipsometer and place underneath the water to avoid any reflection of the light beam from the air-water interface.

All the measurements performed on SLB under this experimental set-up were unsuccessful. The main reason for this arises from geometrical constraints induced by the walls of the 3D printed cell. Under this experimental set-up the arms of the ellipsometer, with the coupled optic guides, can only cover the limited range of AOI between 35 – 63º. At the water-silicon interface, the Brewster angle occurs approximately at 71.1º. Therefore, all the measurements performed under this experimental set-up missed the zone where the ellipsometric angles (mainly Δ) are more sensitive to changes in the surface film. The measurements were performed on three different SLBs comprised of DPPC/DPPE (8:2 molar ratio) to access the viability of the set-up. The calculated thicknesses of these SLBs were 17.4, 23.9 and 78.9 Å, highly displaying the inaccuracy of the measurement under this experimental set-up (*figure 15*). Additionally, considering that the Langmuir-Schaefer

mechanism available at Institut Laue-Langevin is manually operated, both for the alignment and dipping of the substrate, the likelihood to occur defective depositions is much higher compared to automated equipments. Indeed, this kind of faulty depositions can lead to thickness measurements analogous to the ones observed here.

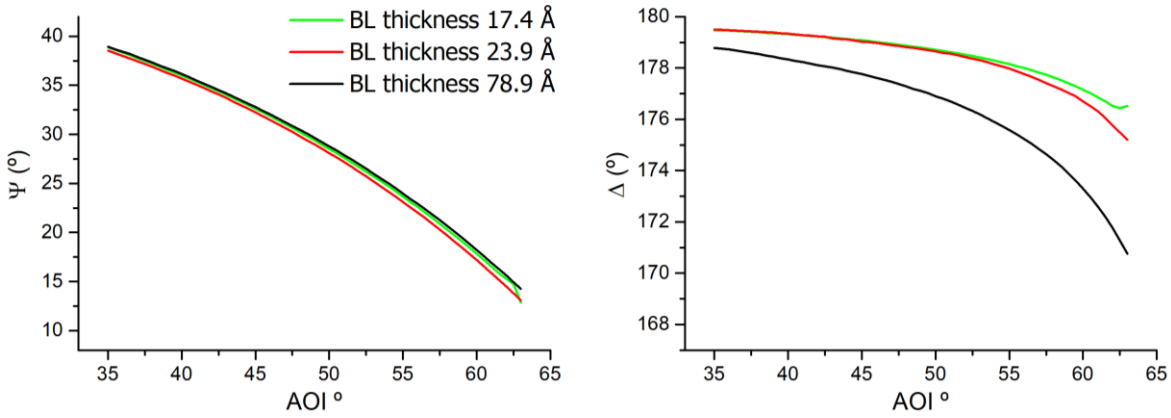

Figure 15: Experimental data acquired for three different SLBs comprised of DPPC/DPPE (8:2 molar). All the SLBs were produced following the same experimental conditions. The calculated thicknesses for these DPPC/DPPE bilayers were 17.4, 23.9 and 78.9 Å.

Even though these measurements were unsuccessful, this experimental set-up can still be useful. One possibility to overcome these limitations can be easily achieved by changing the substrate to glass [119] or mica [120]. Since both these materials have much lower refractive index than silicon, the Brewster angle for these interfaces is achieved roughly around 50º which perfectly fits the requirements for this experimental set-up. Another possibility to overcome these limitations is attainable by designing a better suited wet cell. Some ellipsometry characterization studies of SLBs supported on silicon wafers inside wet cells can be found in bibliography [91,97].

Although some ellipsometric characterizations of SLBs produced by Langmuir deposition were attempted here without success, it is important to mention that some samples were produced with the intent to be analyzed by ssNMR to evaluate its viability for sample preparation. However, due to the COVID19 pandemic, these samples were not analyzed. Ellipsometry might be the appropriate tool to access the SLB film quality before ssNMR analysis however these aspects deserve future work.

While the ellipsometric characterization of the monolayers preparations (Section 4.1.1) rendered good results which are corroborating previous observations, the characterization of supported bilayers was not successful and therefore no further analyses, either with PIP2, cargoes or protein, were attempted. Nevertheless, future efforts should be

done to troubleshoot the limitations stated in this section and implement ellipsometric characterization into protein adsorption studies, directly complementing observations from QCM-D (Section 4.3). Together, QCM-D and ellipsometry can provide information on both hydrated and dry mass, therefore, unravelling a much more comprehensive description of these protein adsorption processes.

4.2. Small-angle neutron scattering results

The small-angle neutron scattering data was acquired in D11 beam line, at Institut Laue-Langevin, during a test-day. For this measurement six samples were analyzed, four liposome solutions with and without proteins and two control solutions with proteins dissolved in buffer. The liposome solutions were comprised of: 1. DOPC:DOPE (7:3, molar); 2. DOPC:DOPE:PIP2 (7:2:1, molar); 3. DOPC:DOPE:PIP2 + AP2; 4. DOPC:DOPE:PIP2 + AP2 + Clathrin. The other two solutions were used as control with AP2 and AP2 + Clathrin proteins dissolved in D2O HKM buffer. The described sample scheme was chosen in a way to address the structural details of the insertion of PIP2 into simple liposomes and study the anchoring dynamics of AP2 into the membrane. Additionally, clathrin was also added as a preliminary test.

The scattering data was merged, and the residual background intensity was subtracted, by extracting the slope from the Porod's plot ($Q^4I(Q)$vs Q^4). *Figure 16* and *figure 17* shows the scattering curves of the different liposome batches analysed. A qualitative analysis of these curves shows clear differences between the plots with and without proteins, *figure 17* and *figure 16* respectively. From the features of the plotted scattering data, one can observe that all samples exhibit a small peak approximately at Q=0.095 $Å^{-1}$ which is indicative of multilamellar contributions. The q-range of this peak is in good agreement with previous SANS reports of multilamellar vesicles [104,121]. Additionally, the lack of plateau zones at low-Q is indicative that the vesicles are too large to capture their overall dimensions over the Q-range used on this measurement. Curiously, these observations are much more dramatic in the samples containing both liposomes and proteins, *figure 17*. Another feature of these scattering curves is highlighted at high-Q values, where all the samples prepared with PIP2 show a characteristic behaviour which is not observed in the vesicle sample prepared without PIP2 lipids (*figure 16*, blue). At higher Q-values, the information provided

probes the organization and structure of the bilayer. Therefore, this characteristic behaviour observed at high-Q values is likely caused by the presence of the PIP2.

The scattering data was then fitted in SasView 4.2.2 software. Despite trying many models, which account for different shapes and sizes of the liposomes and liposome/protein complexes, no good fit was achieved for the full Q-range of the analyzed samples. A partial fit was performed, with satisfactory results, for the high-Q section of the vesicles without PIP2 lipids (*figure 16*, top), as shown in *figure 18*.

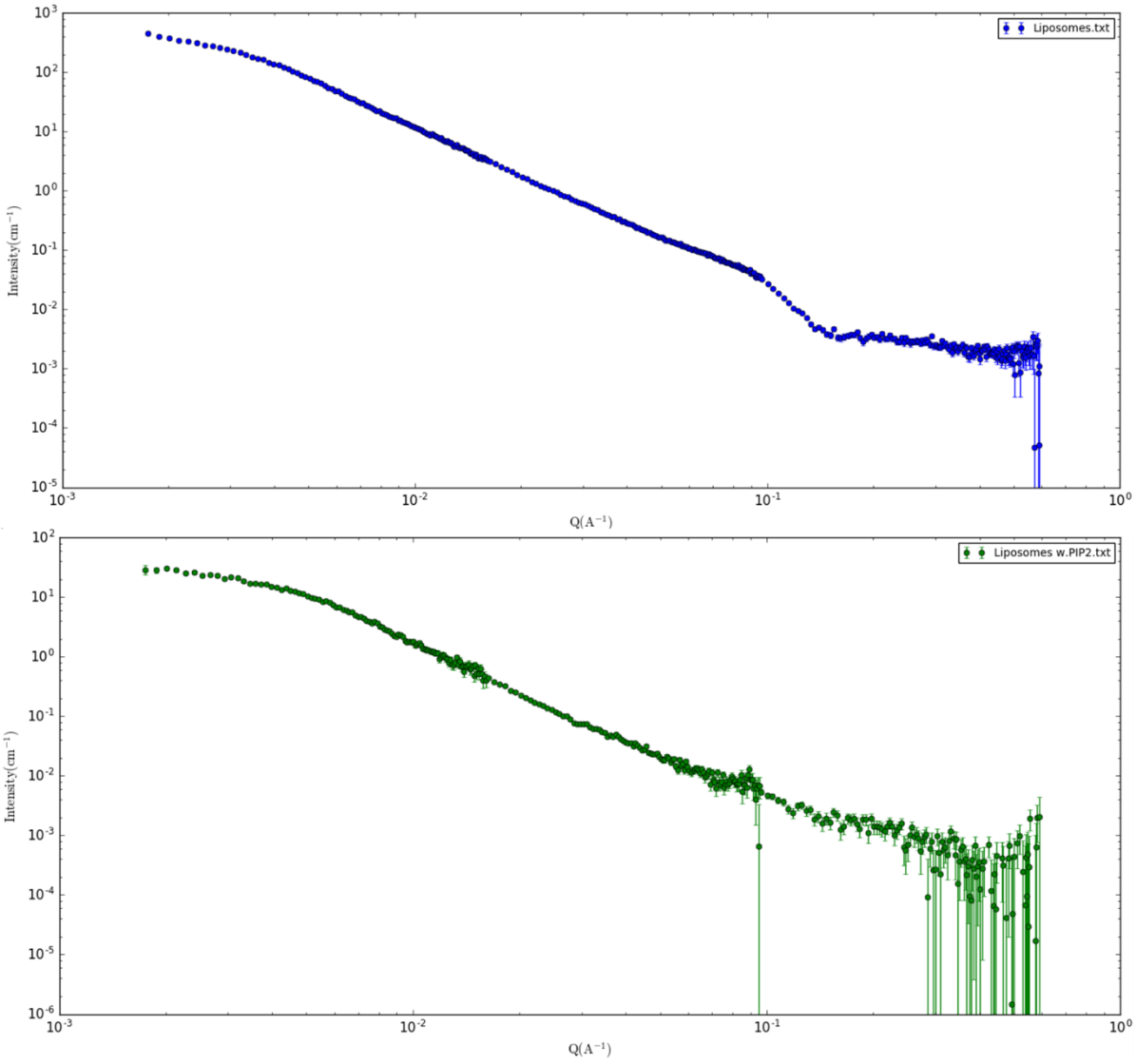

Figure 16: Measured scattering curves of liposomes prepared with (bottom, green) and without (top, blue) PIP2 lipids. Both liposome vesicle solutions were prepared in the same way with the only difference being the presence of PIP2. For the top image, the liposome composition was DOPC:DOPE (7:3 molar); for the bottom, image the liposome composition was DOPC:DOPE:PIP2 (7:2:1 molar).

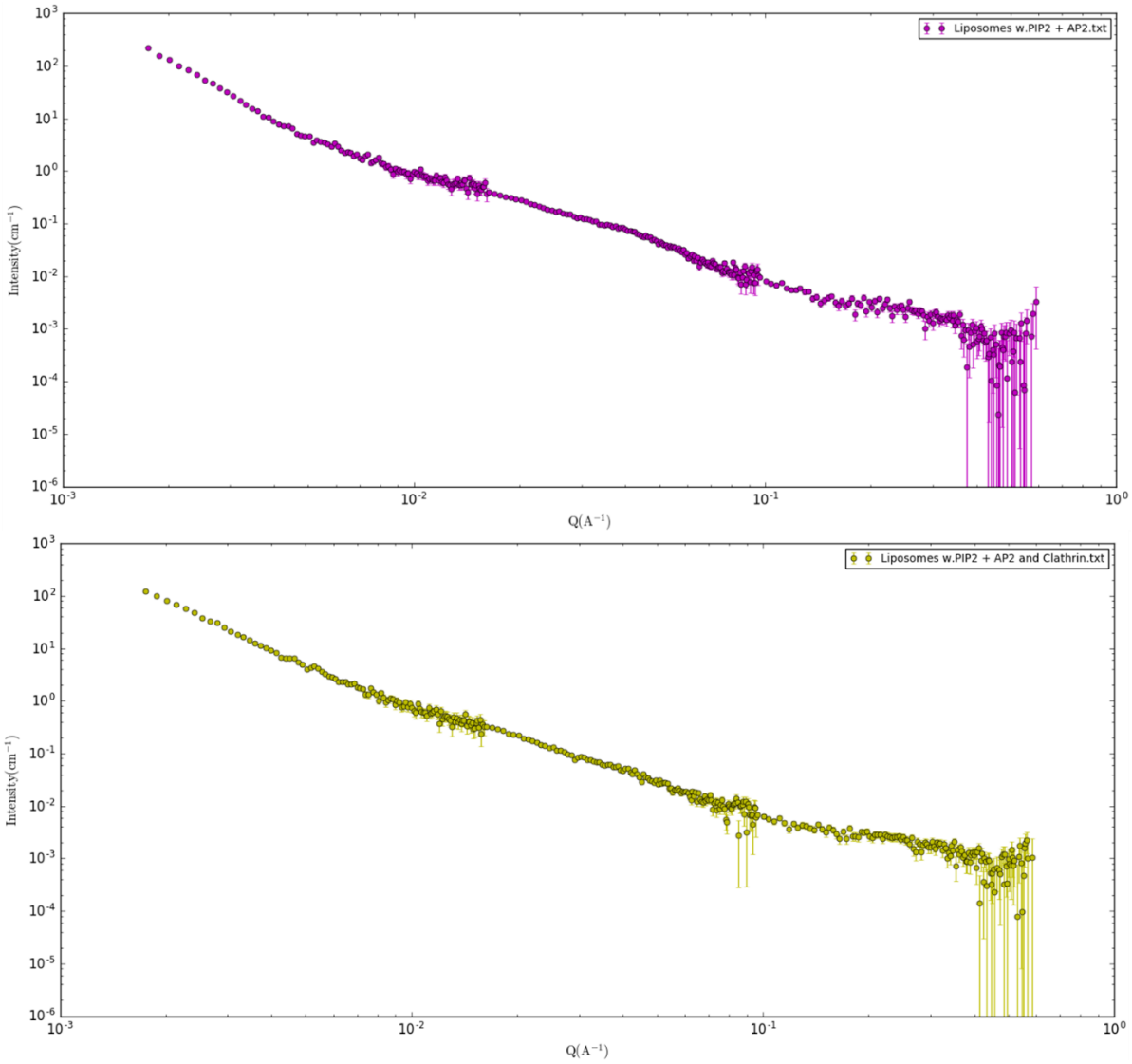

Figure 17: Measured scattering curves of liposomes containing PIP2 lipids incubated with AP2 (top, purple) and AP2 + Clathrin (bottom, yellow). Both liposome solutions were prepared in the same way and are comprised of DOPC:DOPE:PIP2 (7:3:1 molar). The proteins were incubated with the liposomes approximately 24h before SANS experiment.

The partial fitting performed for the high-Q section of the DOPC:DOPE (7:3 molar) vesicles is shown in *figure 18*. The fitted section was set for the Q-range of 0.0180 – 0.5915 $Å^{-1}$. The low-Q section of the data was not included in the fitting due to the lack of a distinct plateau, typical of well-defined vesicle radii. The fitting was performed with a χ_R^2 of 35.22 . The bilayer thickness found for this fitting, 36.15 ± 0.10 Å, is in good agreement with previous works that report similar bilayers thicknesses in DOPC vesicles (37Å) and DOPC:DOPE vesicles (35 Å) at 1:1 molar ratio [104,122]. The differences between the fitted and reported bilayer thicknesses are likely to be related with the amount of DOPE-lipids, which for the case of the liposomes used here was 30% of the overall molar composition.

Additionally, the total dimension of the vesicle, 99.1 nm, is consistent with the hydrodynamic diameter from DLS, 122.0 ± 49.2 nm. One curious feature of the scattered data is the presence of a very tender Bragg peak at Q=0.095 $Å^{-1}$ indicative of multilamellar vesicles. Even though the vesicles were extruded 15x times through a 200 nm pore membrane followed by another 25x through a 100 nm pore membrane the overall lamellarity profile of the vesicles was not homogenous. These observations are concordant with previous works on POPC and DOPC extruded vesicles [104]. Curiously, this behaviour is not observed on DPPC vesicles [104]. It is hypothesized that the increase of multilamellarity in POPC and DOPC vesicles, observed even after extrusion, is related to the formation of multilamellar vesicles, after hydration, with similar sizes as the pores of the extruder membrane [104].

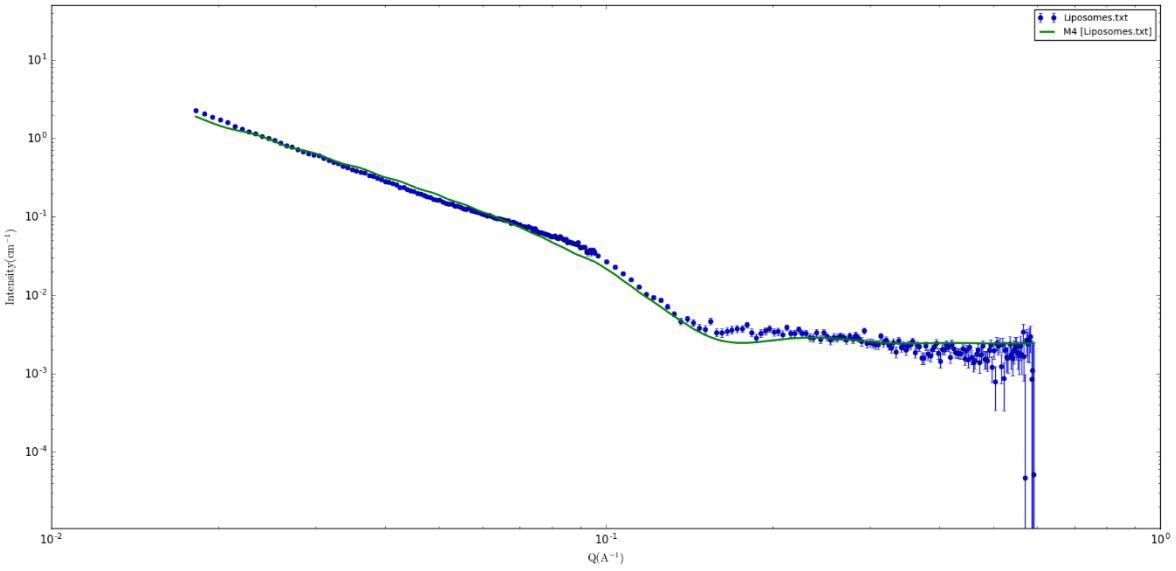

Figure 18: Measured and fitted section of SANS scattering data for DOPC:DOPE (7:3 molar) vesicles, for the Q-range of 0.0180 – 0.5915 $Å^{-1}$. The measured scattering data is shown as blue dots, while the fitted data is shown as a solid green line. The vesicles were extruded 15x through a 200 nm pore membrane followed by another 25x through a 100 nm pore membrane. The best-fit parameters indicate a bilayer thickness of 36.15 ± 0.10 Å and an overall vesicle diameter of 99.1 nm.

The lack of a good fitting on the remaining samples is likely to be correlated with the aggregation problems observed during the formulation of the liposomes (see *Appendix B*). All these liposomes share a common trait; they have PIP2 lipids in their composition. Some reports in the literature have already addressed the aggregation potential of PIP2 in membranes with some studies suggesting that PIP2 headgroups can form hydrogen-bond networks [123,124]. Additionally, some reports observed macromolecular aggregates of PIP2

induced by divalent cations like Mg^{2+} and Ca^{2+} [125]. Indeed, the deuterated HKM buffer used for the vesicle formulation had 5mM Magnesium Acetate ($Mg(CH_3COO)_2$) in its composition which is likely related with the aggregation observed. Additionally, the presence of DOPE also might contribute to the macroscopic lipid flocculation observed in *figure S3 – Appendix B*. DOPE has a tendency to self-aggregate and flocculate which is a common behaviour in PE-lipids. This is related to the negative curvature of these lipids which form, preferentially, aggregate structures with a negative curvature *e.g.* inverted hexagonal phases H_{II} [126,127].

Even though the data provided from the small-angle neutron scattering did not render the expected results, it was important to highlight some crucial aspects of sample preparation that deserve future attention. Indeed, the execution of this SANS experiment during a test-day was meant to be a preliminary test to access the behaviour of the different components of the experimental system in order to optimize the protocol for future measurements. However, due to the ongoing COVID19 pandemic, both the access to the instrument and the reactor cycles were deeply affected, preventing any further SANS measurements. Still, the observations from these samples highlight the importance to adapt the sample preparation and methodologies to suit the particularities of each analytical technique. As it was discussed above, the components chosen to the liposome formulation gave rise to inhomogeneous liposomes. For future work, is important to rethink the lipid composition of the liposome vesicles, with DPPC being a possible solution since it is less prone to residual multilamellar contributions [104]. Additionally, the composition of the buffer also needs to be optimized with respect to the presence of divalent cations, in order to avoid flocculation of lipid material.

4.3. QCM-D results

4.3.1. Vesicle adsorption and fusion kinetics

The supported lipid bilayer systems studied under QCM-D are formed by vesicle adsorption and fusion into a functionalized solid support. The liposomes vesicles formulation protocol was optimized as discussed in *Appendix C*. Many aspects have been discussed to influence the SLB formation by vesicle fusion such as the vesicle size and concentration, lipid composition, pH, ionic type and strength, temperature, substrate type, amongst many others [128]. One notable feature commonly observed regards the specificity of

the optimal experimental conditions, which are dependent on the type of vesicle composition and lipid ratios [128]. Indeed, one of the aspects under discussion is the role of divalent cations in the vesicle adsorption and fusion kinetics.

Considering the above, the formation of the SLB by vesicle fusion of liposomes suspended in two different buffers was monitored by QCM-D, as shown in *figure 19*. Similar studies have already been performed for POPC vesicles [129] and DOPC [76], however no studies are found for DOPC/DOPE lipid mixtures, neither vesicles containing PIP2 lipids. The HKM and HKT buffers (Section 3.1.4) share the same bulk composition, diverging just in the presence or absence of Magnesium Acetate ($Mg(CH_3COO)_2$), respectively. Both these buffers are routinely used in Adaptor Protein 2 studies.

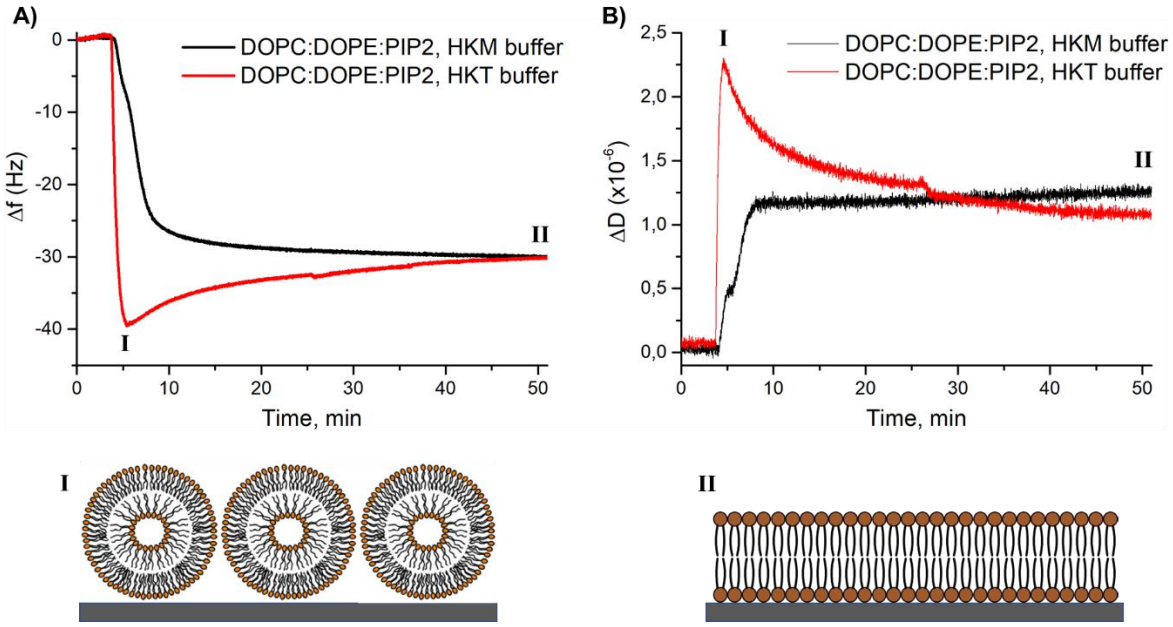

Figure 19: Vesicle adsorption and fusion kinetics in the presence or absence of the divalent cation Mg^{2+}. The frequency (A) and dissipation (B) plots shows a distinct profile between both SLB prepared with HKM (black line) and HKT buffer (red line). While for HKT buffer, the adsorption and fusion kinetics exhibits a common two-step SLB formation, illustrated by the step I (bottom left) and step II (bottom right), for HKM buffer the formation of the SLB is characterized by one-step process, where the vesicle is adsorbed and ruptured instantaneously into a SLB (II).

The adsorption and fusion kinetics of the vesicles exhibit distinct behaviours in the presence and absence of Mg^{2+}. The SLB formed by HKT buffer (*figure 19*, red line) shows the common two-step formation where, first, a critical concentration of vesicle surface coverage is reached (identified by "I"), followed by vesicle rupture and fusion giving rise to a planar SLB (identified by "II"). The critical concentration of vesicles adsorbed in the QCM-D sensor is illustrated by the minimum and maximum points observed in the *figure*

19A and *figure 19B*, respectively. After reaching the vesicle critical concentration (identified by "I") a decrease on ΔD and an increase in Δf is observed, highlighting the dynamic process of vesicle rupture and fusion on the solid support. While the frequency increase is caused by the vesicle rupture with respective release of the large amount of buffer trapped inside its lumen, the progressive dissipation decrease is caused by the release of the buffer trapped inside the vesicles and formation of a more rigid and organized structure on the surface of the QCM-D sensor. The stabilization of both these parameters highlights the formation of a planar SLB (identified by "II"). The formation of SLB with high surface coverage typically exhibit Δf = - 27 ± 3 Hz [128], which is consistent with the values observed in *figure 19*. On the other hand, the SLB formed with HKM buffer (*figure 19*, black line) exhibits a much faster adsorption and fusion process, characterized by a one-step SLB formation where the vesicles adsorb and rupture instantaneously into the functionalized solid support, bypassing the initial step observed for HKT buffer where a critical concentration of vesicle surface coverage is reached (step "I").

The plots shown on *figure 19* highlight the role of the divalent cation Mg^{2+} as a fusogenic agent, rendering faster adsorption and fusion kinetics. Similar observations were previously done for SLB with different composition [76,129]. The fusogenic character of divalent cations is associated with its role in the mediation of vesicle-substrate interactions by charge bridging. In fact, these interactions were shown to be more pronounced between negatively charged lipids headgroups and negatively charged substrates [130]. These observations are in good agreement with the results shown in *figure 19*, where Mg^2 mediated charged bridging, likely with PIP2-lipids due to its negatively charged nature, lead to much faster adsorption and fusion kinetics. Additionally, the stabilization of QCM-D parameters (f and D) was also much faster for HKM (20-30 min) than for HKT buffer (>50 min). Another relevant point that deserves to be highlighted concerns the presence of vesicles trapped in the middle of the bilayer. Since HKM buffer render a one-step SLB formation where the vesicles are adsorbed and ruptured instantaneously, the likelihood of vesicles getting trapped into patches of the bilayer is highly reduced in comparison to HKT buffer.

Altogether, these observations showcase the beneficial role of HKM buffer (or the divalent cation Mg^{2+}) providing not only faster adsorption and fusion rates, but also the formation of more efficient and less prone to defects supported lipid bilayers. Considering these observations, HKM buffer was used on the following QCM-D experiments.

These findings provide a useful comparison with the already studied POPC [129], DOPC [76] and DOPC/DOPS [130] lipid system. However it remains to be seen how other commonly used divalent cations *e.g.* Ca^{2+} and Sr^{2+}, can influence the adsorption and fusion of the DOPC:DOPE:PIP2 vesicles.

4.3.2. Supported lipid bilayer viscoelastic properties

In order to study the binding of AP2 into the membrane, different SLBs were produced. The rationale for the production of the SLBs consisted in varying the different anchoring points; SLBs were produced with PIP2 lipids, cargo molecules (TGN38 and CD4), PIP2 and cargo molecules together, and without both PIP2 and cargo molecules, as a control.

The formation of the different SLBs was monitored by QCM-D. The parameters Δf and ΔD were recorded over time. In order to extract valuable information, the QCM-D raw data was fitted according to the Voigt-Voinova model (Section 2.3.1.4) [86]. Voigt-Voinova model was used instead of Sauerbrey model (Section 2.3.1.2) due to lack of overlapping between the different harmonics, $\Delta D > 0$ and $\Delta D_n/\Delta f_n$ ratios greater than 1.0×10^{-8} Hz^{-1}. All these characteristics are indicative of viscoelastic films. The parameters kept fixed during the fitting were fluid density (1000 kg/m^3), fluid viscosity (0.001 kg/ms), and layer density (1100 kg/m^3). Viscosity, shear modulus and thickness were fitted for the QCM-D parameters Δf and ΔD, recorded over six different overtones (n=3,5,7,…,13).

For the fitting, two different sections of the plots Δf and ΔD vs. time were selected in order to evaluate which provide better fit to the Voigt-Voinova model and more stable modelled parameters. The sections for the fitting of the SLB were chosen before (*Section A*) and after (*Section B*) buffer wash, as shown in *figure 20*. The fitted parameters, presented in *figure S7* and *S8 – Appendix D*, shown a clear difference between *Section A* and *Section B*. The fitting generated from *Section B* provided better parameters indicating a more stable system. The buffer wash is responsible for removing the remaining unfused vesicles from the QMC-D microfluid chamber and, therefore, allowing a better stabilization of the system. This rationale was kept for the fitting of all SLBs produced.

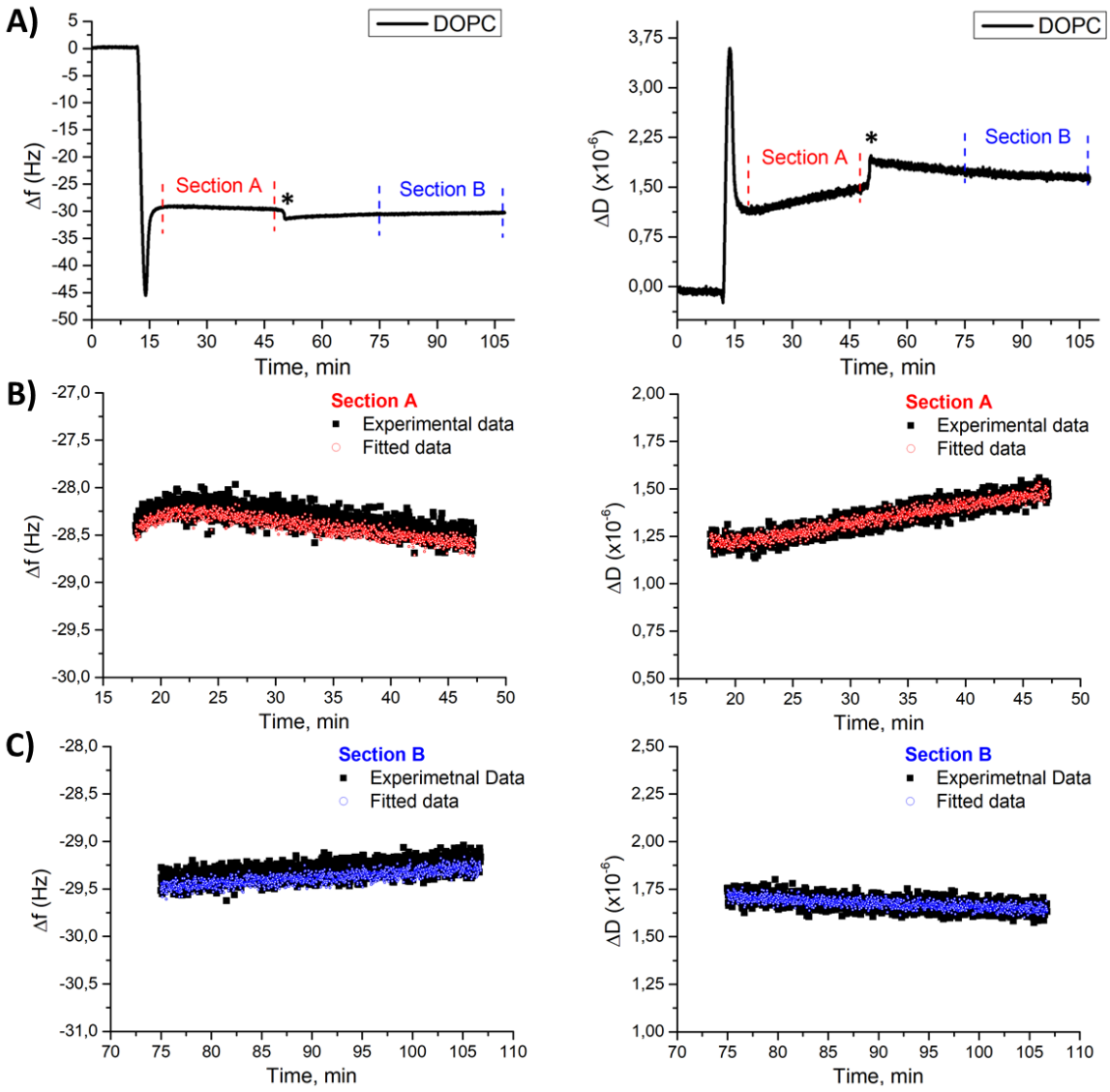

Figure 20: Experimental and fitted data for the formation of DOPC supported lipid bilayer monitored by QCM-D. The formation of the DOPC supported lipid bilayer was monitored by QCM-D and the raw data is shown in the plots Δf vs time and ΔD vs time (A). The fitting of the SLB was performed through the Voigt-Voinova model in two distinct zones, before (Section A, red) and after buffer wash (Section B, blue). The fitted parameters are shown in *figure S7* and *figure S8 – Appendix D*. The buffer wash is identified by *.

The different SLBs produced across this work were fitted, according to the previous description, and are summarize in *figure 21* which correlates their viscoelastic properties, shear modulus and viscosity. One can observe a close similarity between the SLBs comprised of DOPC and DOPC:DOPE (8:2 molar). The insertion of PIP2 into the SLB is translated into an increase on both shear modulus and viscosity, compared to the simple SLBs formulated just with DOPC or DOPC/DOPE. Following the same trend, the insertion of both cargo molecules, TGN38 and CD4, also exhibited an increase in both viscosity and shear modulus. However, the increase of these parameters was much more dramatic for the

insertion of cargo molecules than for PIP2. Unexpectedly, when combined together, PIP2 and CD4, shown a similar behaviour to the one observed for the insertion of PIP2, however the values for viscosity and shear modulus are slightly smaller than those observed for PIP2 insertion.

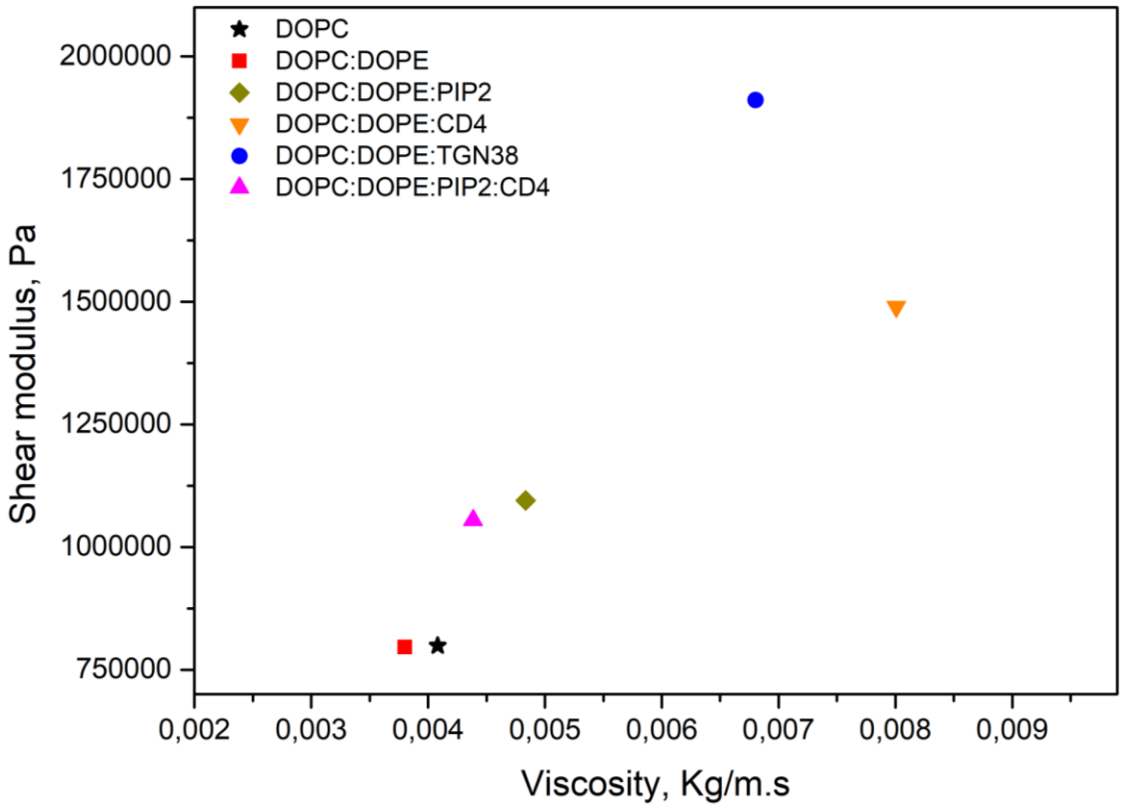

Figure 21: Supported lipid bilayers viscoelastic properties. The viscoelastic contributions of each component used for the production of the SLBs is highlighted by the correlation of shear modulus and viscosity.

The values of shear modulus and viscosity found for the DOPC supported lipid bilayer are in good agreement with previous reports of POPC [131]. Even though not many studies are found where the relation between the viscoelastic properties of the SLB and the insertion of different components is explored, similar observations to the ones described above have been reported for cholesterol [132]. Al-Rekabi and collaborators observed by AFM that increasing concentrations of cholesterol lead to increased viscoelasticity of DPPC supported lipid bilayers. As the concentration of cholesterol increases, the system exhibits increased elasticity and viscosity [132]. While on one hand the structure and mechanism of insertion of cholesterol are quite distinct from both the PIP2-lipids and cargo molecules, on the other hand, the insertion of all these components into the SLB seems to drive the same viscoelastic modifications. It is hypothesized that the increase of elasticity and viscosity of

the SLB by both PIP2 and cargo molecules can be related with the bulkiness and the charge of these components, likely with the latter playing a role in intermolecular bonding. However, this point deserves future work with optimized rheological techniques *e.g.* AFM.

As denoted above, surprisingly, the combination of PIP2 and CD4 in the SLB exhibited a rather unexpected viscoelastic profile. The observed values of shear modulus and viscosity show viscoelastic properties similar to those observed for SLBs with PIP2 lipids. This behaviour is quite distinct from the one observed for the insertion of CD4 or TGN38. One possible explanation for this behaviour might be related with the opposite charge of these structures. While PIP2 is a negatively charged lipid, the CD4 peptide is positively charged. The opposing charge of these components might lead to aggregation processes, between PIP2 lipids and CD4, preventing the insertion of CD4 into the SLB and decreasing the levels of PIP2 available at the surface of the SLB. In the next section, another observation seems to suggest the possibility of aggregation processes between PIP2 and CD4.

Even though supported lipid bilayers produced with both PIP2 and TGN38 are not featured here, studies were carried with these components. Vesicles produced with both PIP2 and TGN38 exhibited an unexpected behaviour. When inserted into the QCM-D microfluid chamber, the vesicles were adsorbed into the sensor however no rupture was observed, as shown in *figure S9 – Appendix E*. Different approaches to promote the fusion of the vesicles with the sensor were tried *e.g.* temperature variation or osmotic shock, however, no vesicle fusion was observed. These observations highlight the necessity to better understand how PIP2 lipids and cargoes interact with each other, since unexpected behaviour was observed both when PIP2 was combined with TGN38 or CD4. Neutron reflectometry is a powerful technique that can resolve the interaction between PIP2-lipids and cargo molecules.

4.3.3. AP2 binding dynamics

As described in the previous section, SLBs were produced with different anchoring points to study the docking of AP2 into the membrane and its dependence on the different anchoring points. The experimental layout followed for the protein studies is presented in *figure 22*.

The addition of protein into the system was only performed after the SLB was stable and the parameters Δf and ΔD were not evolving anymore. AP2 was suspended in HKM buffer and inserted into the system. The protein was added into the system in a ratio of

approximately 20:1, considering a binding stoichiometry of 1:1 for both AP2-cargoes and AP2-PIP2. As shown in *figure 22*, the docking of AP2 into the SLBs containing PIP2-lipids, is almost instantaneous, producing a major frequency shift just a couple of second after being introduced into the QCM-D microfluid chamber.

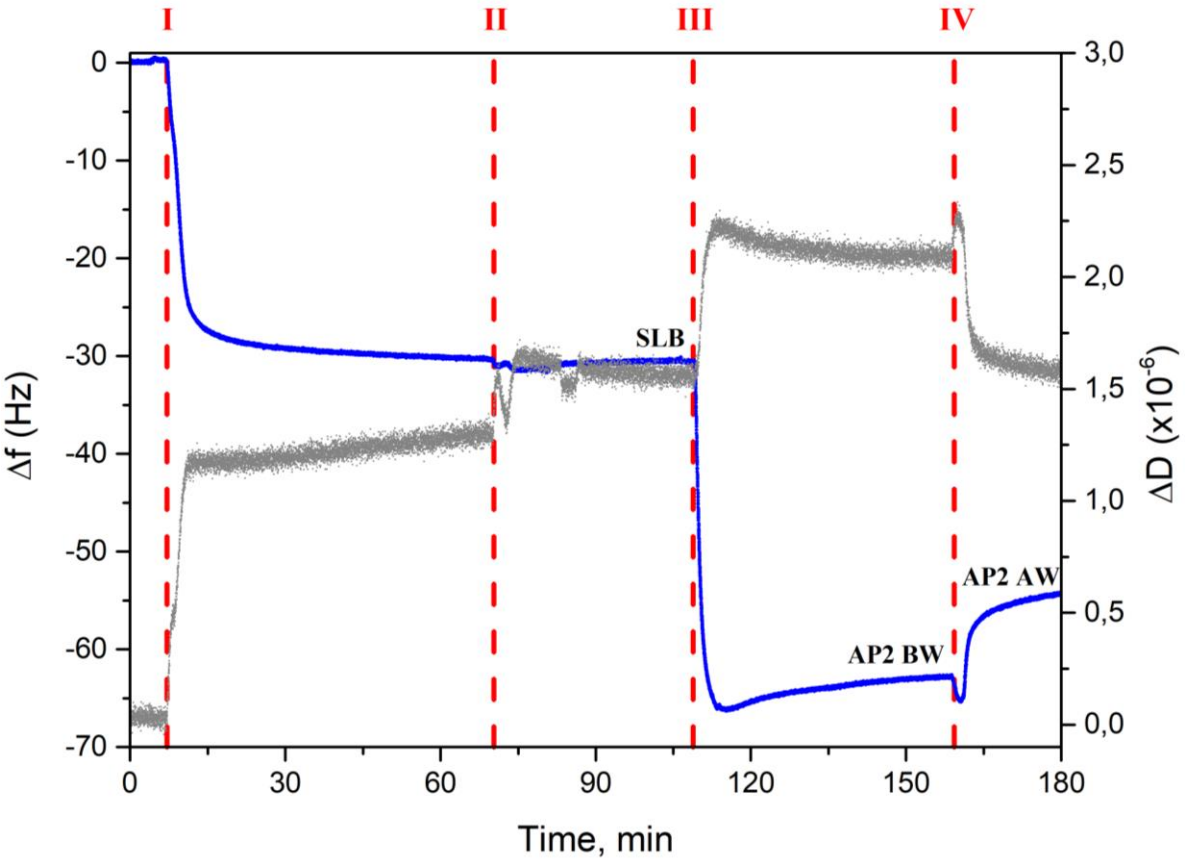

Figure 22: Schematic representation of the experimental layout followed for the protein studies. The QCM-D experiment is divided into four steps: I - loading of liposomes; II - buffer wash; III – loading of AP2; IV – buffer wash. SLB, AP2 BW and AP2 AW indicate the zones of interest for the calculation of protein binding. The QCM-D parameters Δf and ΔD are show as blue and grey, respectively. The plotted data is relative to a SLB comprised of DOPC:DOPE:PIP2 (7:2:1, molar) with the addition of AP2-protein in a ratio of approximately 20:1 (AP2:PIP2).

The frequency shifts relative to the binding of protein were calculated as shown in *equation 13* and *equation 14*,

$$\Delta f_{before\ wash} = \Delta f_{AP2\ BW} - \Delta f_{SLB} \quad (13)$$

$$\Delta f_{after\ wash} = \Delta f_{AP2\ AW} - \Delta f_{SLB} \quad (14)$$

where, Δf_{SLB} is the frequency relative to the formation of the SLB, right before addition of protein, $\Delta f_{AP2\ BW}$ is the frequency of AP2 before the buffer wash and $\Delta f_{AP2\ AW}$ is the frequency of AP2 before after wash. The contributions of the supported lipid bilayer were

subtracted to the protein frequency shifts in order to normalize the frequency relative to AP2 binding.

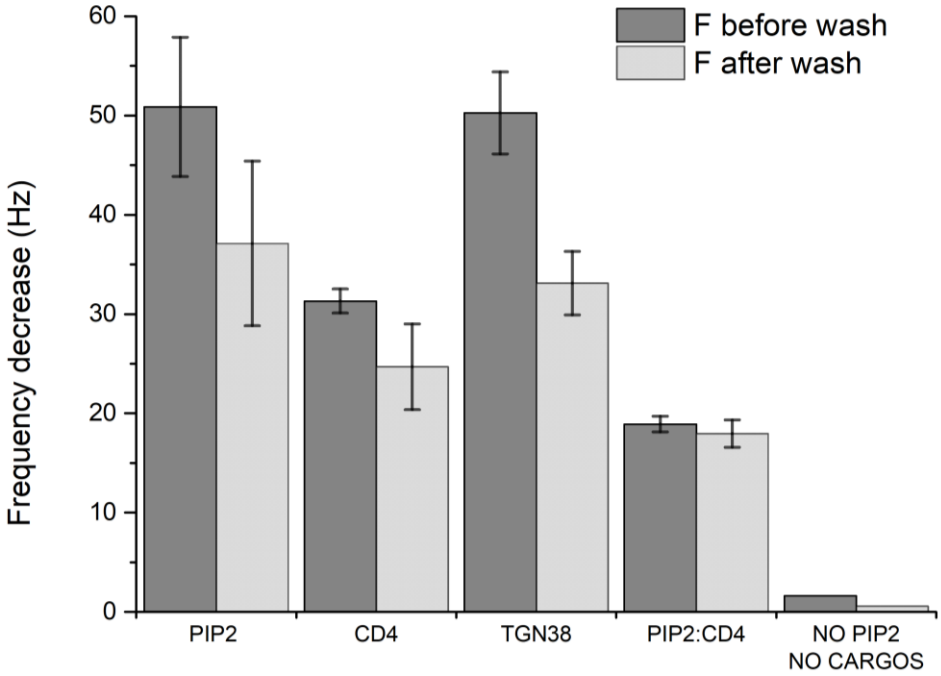

Figure 23: Frequency shifts, monitored by QCM-D, for AP2 docking into the SLB. Supported lipid bilayer functionalized with anchoring points (PIP2, cargo molecules (TGN38 and CD4) or both) were produced to access the binding efficiency of AP2 with each of these components. The frequency shift produced by AP2 is shown before (dark grey) and after buffer wash (light grey).

Figure 23 shows the frequency shifts for AP2 docking into the SLB functionalized with different anchoring points. The bigger frequency shift was observed for the binding of AP2 with SLBs functionalized with PIP2 lipids, which exhibit frequency shifts of 50.87 ± 7.02 and 37.10 ± 8.29 Hz before and after buffer wash, respectively. Following a similar trend, SLBs functionalized with TGN38 show similar frequency shifts with 50.26 ± 4.13 and 33.11 ± 3.20 Hz before and after buffer wash, respectively. On the other hand, SLBs functionalized with CD4 exhibited much tender frequency shifts with 31.30 ± 1.21 and 24.68 ± 4.31 Hz before and after buffer wash, respectively. Unexpectedly, the AP2 binding with SLBs functionalized with both PIP2 and CD4 displayed the smaller frequency shifts observed across all the SLB batches prepared, with 18.91 ± 0.79 and 17.95 ± 1.38 Hz before and after buffer wash, respectively. The binding of AP2 with a common DOPC/DOPE supported lipid bilayer (8:2 molar) was also tested and no binding was observed.

The bigger frequency shifts, observed for the binding of AP2 with SLBs functionalized with PIP2 lipids, is in good agreement with previous reports [31]. AP2 is known

to have two major conformations, one closed and one open [33]. The first step of AP2 activation and conformational change from close to open conformation is induced by the binding of PIP2-lipids. The closed conformation of AP2 has two binding pockets for PIP2 on α and β2 subunits. A third binding pocket for PIP2 on C-μ2, hidden in the close conformation, is revealed after AP2 undergoing into its conformational change, induced by the attaching to the membrane via α and β2 subunits [33]. The presence of three binding sites for PIP2 can justify the higher values of AP2 binding, observed on SLBs functionalized with PIP2-lipids.

The frequency shifts observed for the binding of AP2 with SLBs functionalized with cargo molecules, either TGN38 or CD4, are unexpected and inconsistent with previous reports. According to the model proposed by David J. Owen and collaborators, the recognition of cargoes dileucine and tyrosine motifs, CD4 and TGN38 respectively, is only possible in the open conformation [30,32,33]. In the locked (or closed) conformation of AP2 the peptide-binding sites are hidden and, therefore, unable for recognition. As described before, the mechanism that drives the conformational change from close to open is PIP2-dependent. Contrary to this, the frequency shifts observed from QCM-D are inconsistent with David J. Owen model, showing binding of AP2 to cargo molecules in the absence of PIP2-lipids. These observations seem to suggest that analogous to the different conformational changes, AP2 might have different binding mechanisms according to the anchoring points available at the surface of the membrane. Additionally, the higher allosteric activation of AP2 in the presence of TGN38, compared to CD4, has already been reported in previous studies [31,33,34]. This also seems to be the case on the QCM-D observations, where TGN38 systematically shown increased AP2 binding frequency shifts over CD4.

The insertion of PIP2 and CD4 into the SLB shown frequency shifts, for the binding of AP2, smaller than those observed for both PIP2 and cargoes alone. These observations were not anticipated. Conversely, since the number of anchoring points for AP2 was increased it was expected to see a frequency shift bigger than those observed for either PIP2 or CD4 alone. This behaviour can be explained in agreement with the viscoelastic observations described, for this SLB batch, under Section 4.3.2. It is likely that PIP2-lipids and CD4 might be engaging in aggregation processes due to its opposite charges, therefore, preventing the insertion of CD4 into the SLB and decreasing the levels of PIP2 available at the surface of the SLB. The decreased levels of both PIP2 and CD4 at the surface of SLB are translated in smaller AP2 binding frequency shifts.

Overall, these observations suggest that the interplay between AP2 and its anchoring points into the membrane it is not fully understood. Even though, AP2 binding of cargoes in the absence of PIP2 was observed under the QCM-D experiments performed in this work, the presence of PIP2 lipids is absolutely necessary for CCP maturation, with CME pathways being highly impaired under acute depletion of these lipids [26,27]. While the importance of PIP2-lipids for CME pathways is not questioned here, the binding mechanism of AP2 into the plasmatic membrane is challenged. Indeed, the observations provided in this work seem to suggest that AP2 might have different binding mechanisms according to the anchoring points available at the surface of the membrane. More importantly, these observations highlight the importance of using membrane mimetic systems to study protein-lipid interactions in a native-like environment. As it was stressed across this dissertation, the initial work plan was seriously impacted by the COVID19 pandemic and, therefore, these observations were not confirmed with other techniques. Additional works are needed to confirm and explore these observations. Particularly, the combination of neutron reflectometry and solid-state NMR seems to be the most solid approach to provide mechanistic and structural information to fully disclose the AP2 interaction with the different membrane anchoring points.

5

Conclusions and Future Work

5. Conclusion and Future work

5.1. Main Conclusions

The main aim of this dissertation was the study through a multi-technique approach of the early steps of CME pathways, specially focusing in the atomic characterization of the interaction interfaces of AP2 with PIP2 lipids and cargo molecules, and clarifying the binding mechanisms of AP2 into the plasmatic membrane. Even though, the proposed multi-technique approach (Section 2.3) was not fully implemented, pertinent observations were obtained from the techniques used and discussed above (Section 4).

In this work, QCM-D was successfully implemented to study the formation and properties of supported lipid bilayers produced with different components and, also, to study the binding of AP2 into the plasmatic membrane equipped with different anchoring points. The main considerations provided from this technique can be divided into two distinct points: characterization and evaluation of lipid preparations; and mechanistic behaviour of AP2 binding into the plasmatic membrane.

The main conclusions concerning the characterization and evaluation of the lipid preparations highlight:

1. The divalent cation Mg^{2+} acts as a fusogenic agent rendering faster adsorption and fusion kinetics and mediating the formation of SLBs that are less prone to defects.
2. The insertion of PIP2 in the SLB has tender effects in the overall viscoelastic properties while, on the other hand, the insertion of cargo molecules exhibits more dramatic effects.
3. The simultaneous insertion of PIP2 and TGN38 or CD4 in the SLB induced unexpected behaviours, preventing the formation of the SLB or decreasing the binding of AP2, respectively.

Concerning the mechanistic behaviour of AP2 binding into the plasmatic membrane, a major observation was done:

1. The AP2 binding results shown that AP2 could bind to SLBs functionalized with TGN38 or CD4 in the absence of PIP2. This major observation seems to suggest that AP2 might have different binding mechanisms according to the anchoring points available at the surface of the membrane.

The experimental results provided from ellipsometry and small-angle neutron scattering experiments did not allow taking major conclusions, since these data sets were incomplete and were still in the initial stages. Nevertheless, important considerations have been made regarding the methodology and sample preparation, which will be important to overcome some of the limitations found in these techniques during this work.

5.2. Future Work

As highlighted across this dissertation, the results presented here are very preliminary and, therefore, many aspects of this work merits future attention. Indeed, many of the points referred on this topic were meant to be addressed during the original work plan for this dissertation. However these points were postponed and should be addressed in the future.

In concerns of ellipsometric measurements, it is still necessary to evaluate the effectiveness of this technique under the experimental set-up described in Section 4.1.2. Indeed, ellipsometric measurements of SLB in-situ might be a very useful way to acquire information that can greatly complement QCM-D data sets but also a suitable technique to characterize and access the quality of SLB films before ssNMR analysis.

Small-angle neutron scattering experiments revealed some fragilities in the sample preparation currently being used for liposome formulation. These observations highlighted the importance to optimize the protocol and sample preparation for similar experiments carried in the future. This technique requires homogenous liposome samples and, therefore, buffer composition and lipid composition need to be carefully chosen and handled.

In regards of vesicle adsorption and fusion kinetics, it is relevant to study the influence of different divalent cations in the formation kinetics of supported lipid bilayers with PIP2 lipids embedded. PIP2 are known to form aggregates in the presence of divalent cations, however, this effect is ion dependent. A better knowledge of the vesicle adsorption and fusion kinetics with different divalent cations can potentially lead to protocol optimization, by precisely picking divalent cation that render better vesicle adsorption and fusion kinetics and have reduced aggregation effects on PIP2.

In concerns of AP2 binding, the observations presented and discussed during this dissertation still need to be confirmed through more powerful and resolved techniques. Neutron reflectometry and ssNMR are suitable techniques that can help clarify these observations. Additionally, is it equally necessary to carry the same type of experiments with

different buffers to access the possible influence of buffers in the AP2 binding dynamics and conformational state.

The relationship between PIP2 and cargo molecules combined exhibited unexpected behaviours. These observations highlight the necessity to better understand how PIP2 and cargoes interact with each other. Neutron reflectometry is a powerful technique that can resolve the interaction between PIP2 lipids and cargo molecules, and lead to optimized protocols to produce SLBs with both components embedded.

Finally, the atomic characterization of AP2 interaction interfaces with both PIP2 and cargo molecules embedded in a native-like environment by means of solid-state NMR and dynamic nuclear polarization (DNP) will contribute to a better understanding at the atomic-level of the binding mechanism between AP2 and membrane anchoring points.

6

Bibliography

6. Bibliography

1. Doherty, G. J. & McMahon, H. T. Mechanisms of Endocytosis. *Annu. Rev. Biochem.* **78**, 857–902 (2009).
2. Canton, I. & Battaglia, G. Endocytosis at the nanoscale. *Chem. Soc. Rev.* **41**, 2718–2739 (2012).
3. Kaksonen, M. & Roux, A. Mechanisms of clathrin-mediated endocytosis. *Nat. Rev. Mol. Cell Biol.* **19**, 313–326 (2018).
4. Yarwood, R., Hellicar, J., Woodman, P. G. & Lowe, M. Membrane trafficking in health and disease. *Dis. Model. & Mech.* **13**, 043448 (2020).
5. Azarnia Tehran, D., López-Hernández, T. & Maritzen, T. Endocytic Adaptor Proteins in Health and Disease: Lessons from Model Organisms and Human Mutations. *Cells* **8**, (2019).
6. Maib, H., Smythe, E. & Ayscough, K. Forty years on: clathrin-coated pits continue to fascinate. *Mol. Biol. Cell* **28**, 843–847 (2017).
7. Traub, L. M. Regarding the amazing choreography of clathrin coats. *PLoS Biol.* **9**, e1001037–e1001037 (2011).
8. Sorkin, A. & von Zastrow, M. Endocytosis and signalling: intertwining molecular networks. *Nat. Rev. Mol. Cell Biol.* **10**, 609–622 (2009).
9. Grant, B. D. & Donaldson, J. G. Pathways and mechanisms of endocytic recycling. *Nat. Rev. Mol. Cell Biol.* **10**, 597–608 (2009).
10. Conner, S. D. & Schmid, S. L. Regulated portals of entry into the cell. *Nature* **422**, 37–44 (2003).
11. Mukherjee, S., Ghosh, R. N. & Maxfield, F. R. Endocytosis. *Physiol. Rev.* **77**, 759–803 (1997).
12. McMahon, H. T. & Boucrot, E. Molecular mechanism and physiological functions of clathrin-mediated endocytosis. *Nat. Rev. Mol. Cell Biol.* **12**, 517–533 (2011).
13. Wu, F. & Yao, P. J. Clathrin-mediated endocytosis and Alzheimer's disease: An update. *Ageing Res. Rev.* **8**, 147–149 (2009).
14. Lakadamyali, M., Rust, M. J. & Zhuang, X. Endocytosis of influenza viruses. *Microbes Infect.* **6**, 929–936 (2004).
15. Tourdot, R. & Radhakrishnan, R. Clathrin Mediated Endocytosis and its Role in Viral Entry. *Atlas Genet. Cytogenet. Oncol. Haematol.* **17**, 583–588 (2013).
16. Inoue, Y. *et al.* Clathrin-Dependent Entry of Severe Acute Respiratory Syndrome Coronavirus into Target Cells Expressing ACE2 with the Cytoplasmic Tail Deleted. *J. Virol.* **81**, 8722 LP – 8729 (2007).
17. Wang, H. *et al.* SARS coronavirus entry into host cells through a novel clathrin- and caveolae-independent endocytic pathway. *Cell Res.* **18**, 290–301 (2008).
18. Yang, N. & Shen, H.-M. Targeting the Endocytic Pathway and Autophagy Process as a Novel Therapeutic Strategy in COVID-19. *Int. J. Biol. Sci.* **16**, 1724–1731 (2020).
19. Mercer, J., Schelhaas, M. & Helenius, A. Virus Entry by Endocytosis. *Annu. Rev. Biochem.* **79**, 803–833 (2010).
20. Flannagan, R. S., Jaumouillé, V. & Grinstein, S. The Cell Biology of Phagocytosis. *Annu. Rev. Pathol. Mech. Dis.* **7**, 61–98 (2012).

21. Lim, J. P. & Gleeson, P. A. Macropinocytosis: an endocytic pathway for internalising large gulps. *Immunol. Cell Biol.* **89**, 836–843 (2011).
22. Kirchhausen, T., Owen, D. & Harrison, S. C. Molecular structure, function, and dynamics of clathrin-mediated membrane traffic. *Cold Spring Harb. Perspect. Biol.* **6**, a016725–a016725 (2014).
23. McLaughlin, S., Wang, J., Gambhir, A. & Murray, D. PIP2 and Proteins: Interactions, Organization, and Information Flow. *Annu. Rev. Biophys. Biomol. Struct.* **31**, 151–175 (2002).
24. Li, Z., Venable, R. M., Rogers, L. A., Murray, D. & Pastor, R. W. Molecular Dynamics Simulations of PIP2 and PIP3 in Lipid Bilayers: Determination of Ring Orientation, and the Effects of Surface Roughness on a Poisson-Boltzmann Description. *Biophys. J.* **97**, 155–163 (2009).
25. Cremona, O. & De Camilli, P. Phosphoinositides in membrane traffic at the synapse. *J. Cell Sci.* **114**, 1041 LP – 1052 (2001).
26. Boucrot, E., Saffarian, S., Massol, R., Kirchhausen, T. & Ehrlich, M. Role of lipids and actin in the formation of clathrin-coated pits. *Exp. Cell Res.* **312**, 4036–4048 (2006).
27. Zoncu, R. *et al.* Loss of endocytic clathrin-coated pits upon acute depletion of phosphatidylinositol 4,5-bisphosphate. *Proc. Natl. Acad. Sci.* **104**, 3793 LP – 3798 (2007).
28. He, K. *et al.* Dynamics of phosphoinositide conversion in clathrin-mediated endocytic traffic. *Nature* **552**, 410–414 (2017).
29. Pearse, B. M. F., Smith, C. J. & Owen, D. J. Clathrin coat construction in endocytosis. *Curr. Opin. Struct. Biol.* **10**, 220–228 (2000).
30. Kelly, B. T. & Owen, D. J. Endocytic sorting of transmembrane protein cargo. *Curr. Opin. Cell Biol.* **23**, 404–412 (2011).
31. Höning, S. *et al.* Phosphatidylinositol-(4,5)-Bisphosphate Regulates Sorting Signal Recognition by the Clathrin-Associated Adaptor Complex AP2. *Mol. Cell* **18**, 519–531 (2005).
32. Kelly, B. T. *et al.* A structural explanation for the binding of endocytic dileucine motifs by the AP2 complex. *Nature* **456**, 976–979 (2008).
33. Jackson, L. P. *et al.* A Large-Scale Conformational Change Couples Membrane Recruitment to Cargo Binding in the AP2 Clathrin Adaptor Complex. *Cell* **141**, 1220–1229 (2010).
34. Kadlecova, Z. *et al.* Regulation of clathrin-mediated endocytosis by hierarchical allosteric activation of AP2. *J. Cell Biol.* **216**, 167–179 (2016).
35. Collins, B. M., McCoy, A. J., Kent, H. M., Evans, P. R. & Owen, D. J. Molecular Architecture and Functional Model of the Endocytic AP2 Complex. *Cell* **109**, 523–535 (2002).
36. Fotin, A. *et al.* Molecular model for a complete clathrin lattice from electron cryomicroscopy. *Nature* **432**, 573–579 (2004).
37. ter Haar, E., Musacchio, A., Harrison, S. C. & Kirchhausen, T. Atomic Structure of Clathrin: A β Propeller Terminal Domain Joins an α Zigzag Linker. *Cell* **95**, 563–573 (1998).
38. Kelly, B. T. *et al.* AP2 controls clathrin polymerization with a membrane-activated switch. *Science (80-.).* **345**, 459 LP – 463 (2014).

39. Mettlen, M., Chen, P.-H., Srinivasan, S., Danuser, G. & Schmid, S. L. Regulation of Clathrin-Mediated Endocytosis. *Annu. Rev. Biochem.* **87**, 871–896 (2018).
40. Wrobel, A. G. *et al.* Temporal Ordering in Endocytic Clathrin-Coated Vesicle Formation via AP2 Phosphorylation. *Dev. Cell* **50**, 494-508.e11 (2019).
41. Maxfield, F. R. Role of Endosomes and Lysosomes in Human Disease. *Cold Spring Harb. Perspect. Biol.* **6**, (2014).
42. Nair, P. Brown and Goldstein: The Cholesterol Chronicles. *Proc. Natl. Acad. Sci.* **110**, 14829 LP – 14832 (2013).
43. Goldstein, J. L., Anderson, R. G. W. & Brown, M. S. Coated pits, coated vesicles, and receptor-mediated endocytosis. *Nature* **279**, 679–685 (1979).
44. Harold, D. *et al.* Genome-wide association study identifies variants at CLU and PICALM associated with Alzheimer's disease. *Nat. Genet.* **41**, 1088–1093 (2009).
45. Jun, G. *et al.* Meta-analysis Confirms CR1, CLU, and PICALM as Alzheimer Disease Risk Loci and Reveals Interactions With APOE Genotypes. *Arch. Neurol.* **67**, 1473–1484 (2010).
46. Raj, T. *et al.* Integrative transcriptome analyses of the aging brain implicate altered splicing in Alzheimer's disease susceptibility. *Nat. Genet.* **50**, 1584–1592 (2018).
47. Miranda, A. M. *et al.* Excess Synaptojanin 1 Contributes to Place Cell Dysfunction and Memory Deficits in the Aging Hippocampus in Three Types of Alzheimer's Disease. *Cell Rep.* **23**, 2967–2975 (2018).
48. Haass, C., Kaether, C., Thinakaran, G. & Sisodia, S. Trafficking and Proteolytic Processing of APP. *Cold Spring Harb. Perspect. Med.* **2**, (2012).
49. Schmid, S. L. Reciprocal regulation of signaling and endocytosis: Implications for the evolving cancer cell. *J. Cell Biol.* **216**, 2623–2632 (2017).
50. Sorkin, A. & Goh, L. K. Endocytosis and intracellular trafficking of ErbBs. *Exp. Cell Res.* **315**, 683–696 (2009).
51. Grandal, M. V. & Madshus, I. H. Epidermal growth factor receptor and cancer: control of oncogenic signalling by endocytosis. *J. Cell. Mol. Med.* **12**, 1527–1534 (2008).
52. Caswell, P. T., Vadrevu, S. & Norman, J. C. Integrins: masters and slaves of endocytic transport. *Nat. Rev. Mol. Cell Biol.* **10**, 843–853 (2009).
53. Mellman, I. & Yarden, Y. Endocytosis and Cancer. *Cold Spring Harb. Perspect. Biol.* **5**, (2013).
54. Di Fiore, P. P. & von Zastrow, M. Endocytosis, Signaling, and Beyond. *Cold Spring Harb. Perspect. Biol.* **6**, (2014).
55. Wang, M. *et al.* Remdesivir and chloroquine effectively inhibit the recently emerged novel coronavirus (2019-nCoV) in vitro. *Cell research* **30**, 269–271 (2020).
56. Khan, M. S., Dosoky, N. S. & Williams, J. D. Engineering lipid bilayer membranes for protein studies. *Int. J. Mol. Sci.* **14**, 21561–21597 (2013).
57. Clifton, L. A. *et al.* Design and use of model membranes to study biomolecular interactions using complementary surface-sensitive techniques. *Adv. Colloid Interface Sci.* **277**, 102118 (2020).
58. Siontorou, C. G., Nikoleli, G.-P., Nikolelis, D. P. & Karapetis, S. K. Artificial Lipid Membranes: Past, Present, and Future. *Membranes (Basel).* **7**, 38 (2017).
59. Saeui, T. C., Mathew, P. M., Liu, L., Urias, E. & Yarema, J. K. Cell Surface and

Membrane Engineering: Emerging Technologies and Applications. *Journal of Functional Biomaterials* **6**, (2015).

60. Eeman, M. & Deleu, M. From biological membranes to biomimetic model membranes. *Biotechnology, Agronomy and Society and Environment* **14**, 719–736 (2010).
61. Lagny, T. J. & Bassereau, P. Bioinspired membrane-based systems for a physical approach of cell organization and dynamics: usefulness and limitations. *Interface Focus* **5**, 20150038 (2015).
62. Bangham, A. D. & Horne, R. W. Negative staining of phospholipids and their structural modification by surface-active agents as observed in the electron microscope. *J. Mol. Biol.* **8**, 660-IN10 (1964).
63. Bangham, A. D., Hill, M. W. & Miller, N. G. A. Preparation and Use of Liposomes as Models of Biological Membranes BT - Methods in Membrane Biology: Volume 1. in (ed. Korn, E. D.) 1–68 (Springer US, 1974).
64. Sheikhpour, M., Barani, L. & Kasaeian, A. Biomimetics in drug delivery systems: A critical review. *J. Control. Release* **253**, 97–109 (2017).
65. Goñi, F. M. *et al.* Phase diagrams of lipid mixtures relevant to the study of membrane rafts. *Biochim. Biophys. Acta - Mol. Cell Biol. Lipids* **1781**, 665–684 (2008).
66. Velázquez, M. M. Langmuir-Blodgett Methodology: A Versatile Technique to Build 2D Material Films. in (ed. Alejo, T.) Ch. 2 (IntechOpen, 2016).
67. Prudovsky, I., Kumar, T. K., Sterling, S. & Neivandt, D. Protein-Phospholipid Interactions in Nonclassical Protein Secretion: Problem and Methods of Study. *International Journal of Molecular Sciences* **14**, (2013).
68. Dixon, M. C. Quartz crystal microbalance with dissipation monitoring: enabling real-time characterization of biological materials and their interactions. *J. Biomol. Tech.* **19**, 151–158 (2008).
69. Höök, F. & Kasemo, B. The QCM-D Technique for Probing Biomacromolecular Recognition Reactions BT - Piezoelectric Sensors. in (eds. Janshoff, A. & Steinem, C.) 425–447 (Springer Berlin Heidelberg, 2007).
70. Qiao, X., Zhang, X., Tian, Y. & Meng, Y. Progresses on the theory and application of quartz crystal microbalance. *Appl. Phys. Rev.* **3**, 31106 (2016).
71. Sauerbrey, G. Verwendung von Schwingquarzen zur Wägung dünner Schichten und zur Mikrowägung. *Zeitschrift für Phys.* **155**, 206–222 (1959).
72. Nomura, T. & Okuhara, M. Frequency shifts of piezoelectric quartz crystals immersed in organic liquids. *Anal. Chim. Acta* **142**, 281–284 (1982).
73. Keiji Kanazawa, K. & Gordon, J. G. The oscillation frequency of a quartz resonator in contact with liquid. *Anal. Chim. Acta* **175**, 99–105 (1985).
74. Kanazawa, K. K. & Gordon, J. G. Frequency of a quartz microbalance in contact with liquid. *Anal. Chem.* **57**, 1770–1771 (1985).
75. Seantier, B., Breffa, C., Félix, O. & Decher, G. Dissipation-Enhanced Quartz Crystal Microbalance Studies on the Experimental Parameters Controlling the Formation of Supported Lipid Bilayers. *J. Phys. Chem. B* **109**, 21755–21765 (2005).
76. Dacic, M. *et al.* Influence of Divalent Cations on Deformation and Rupture of Adsorbed Lipid Vesicles. *Langmuir* **32**, 6486–6495 (2016).
77. Justesen, P. H., Kristensen, T., Ebdrup, T. & Otzen, D. Investigating porcine pancreatic phospholipase A2 action on vesicles and supported planar bilayers using a

quartz crystal microbalance with dissipation. *J. Colloid Interface Sci.* **279**, 399–409 (2004).

78. Glasmästar, K., Larsson, C., Höök, F. & Kasemo, B. Protein Adsorption on Supported Phospholipid Bilayers. *J. Colloid Interface Sci.* **246**, 40–47 (2002).
79. Buzhynskyy, N. *et al.* Annexin-A6 presents two modes of association with phospholipid membranes. A combined QCM-D, AFM and cryo-TEM study. *J. Struct. Biol.* **168**, 107–116 (2009).
80. Bradshaw, B. L. Understanding piezoelectric quartz crystals. *RF Des.* **23**, 50–59 (2000).
81. Janshoff, A., Galla, H.-J. & Steinem, C. Piezoelectric Mass-Sensing Devices as Biosensors—An Alternative to Optical Biosensors? *Angew. Chemie Int. Ed.* **39**, 4004–4032 (2000).
82. Liu, G. & Zhang, G. Basic Principles of QCM-D. in (eds. Liu, G. & Zhang, G.) 1–8 (Springer Berlin Heidelberg, 2013). doi:10.1007/978-3-642-39790-5_1
83. Edvardsson, M. How does QCM-technology work? *Biolin Scientific Blog* (2019). Available at: https://blog.biolinscientific.com/how-does-qcm-technology-work. (Accessed: 22nd May 2020)
84. Rodahl, M., Höök, F., Krozer, A., Brzezinski, P. & Kasemo, B. Quartz crystal microbalance setup for frequency and Q-factor measurements in gaseous and liquid environments. *Rev. Sci. Instrum.* **66**, 3924–3930 (1995).
85. Arnau, A. A Review of Interface Electronic Systems for AT-cut Quartz Crystal Microbalance Applications in Liquids. *Sensors* **8**, (2008).
86. Voinova, M. V, Rodahl, M., Jonson, M. & Kasemo, B. Viscoelastic Acoustic Response of Layered Polymer Films at Fluid-Solid Interfaces: Continuum Mechanics Approach. *Phys. Scr.* **59**, 391–396 (1999).
87. Papanicolaou, G. C. & Zaoutsos, S. P. 1 - Viscoelastic constitutive modeling of creep and stress relaxation in polymers and polymer matrix composites. in *Woodhead Publishing Series in Composites Science and Engineering* (ed. Guedes, R. M. B. T.-C. and F. in P. M. C. (Second E.) 3–59 (Woodhead Publishing, 2019).
88. Woollam, J. A. *et al.* Overview of variable-angle spectroscopic ellipsometry (VASE): I. Basic theory and typical applications. in *Proc.SPIE* **10294**, (1999).
89. Gonçalves, D. & Irene, E. A. Fundamentals and applications of spectroscopic ellipsometry. *Química Nova* **25**, 794–800 (2002).
90. Losurdo, M. *et al.* Spectroscopic ellipsometry and polarimetry for materials and systems analysis at the nanometer scale: state-of-the-art, potential, and perspectives. *J. Nanoparticle Res.* **11**, 1521–1554 (2009).
91. Kamble, S., Patil, S., Kulkarni, M. & Murthy, A. V. R. Spectroscopic Ellipsometry of fluid and gel phase lipid bilayers in hydrated conditions. *Colloids Surfaces B Biointerfaces* **176**, 55–61 (2019).
92. González-Henríquez, C. M., Villegas-Opazo, V. A., Sagredo-Oyarce, D. H., Sarabia-Vallejos, M. A. & Terraza, C. A. Thermal Response Analysis of Phospholipid Bilayers Using Ellipsometric Techniques. *Biosensors* **7**, (2017).
93. Stroumpoulis, D., Parra, A. & Tirrell, M. A kinetic study of vesicle fusion on silicon dioxide surfaces by ellipsometry. *AIChE J.* **52**, 2931–2937 (2006).
94. Elender, G., Kühner, M. & Sackmann, E. Functionalisation of Si/SiO2 and glass surfaces with ultrathin dextran films and deposition of lipid bilayers. *Biosens.*

Bioelectron. **11**, 565–577 (1996).

95. Miszta, A. *et al.* Combination of ellipsometry, laser scanning microscopy and Z-scan fluorescence correlation spectroscopy elucidating interaction of cryptdin-4 with supported phospholipid bilayers. *J. Pept. Sci.* **14**, 503–509 (2008).
96. Reiter, R., Motschmann, H. & Knoll, W. Ellipsometric characterization of streptavidin binding to biotin-functionalized lipid monolayers at the water/air interface. *Langmuir* **9**, 2430–2435 (1993).
97. Howland, M. C., Szmodis, A. W., Sanii, B. & Parikh, A. N. Characterization of Physical Properties of Supported Phospholipid Membranes Using Imaging Ellipsometry at Optical Wavelengths. *Biophys. J.* **92**, 1306–1317 (2007).
98. Alves, C. Calculation of Small-Angle Scattering Patterns. in (ed. Yokaichiya, C. L. P. O. E.-M. K. K. D. F. E.-F.) Ch. 1 (IntechOpen, 2018).
99. Fanchon, E., Geissler, E., Hodeau, J. L., Regnard, J. R. & Timmins, P. A. *Structure and Dynamics of Biomolecules: Neutron and Synchrotron Radiation for Condensed Matter Studies*. (OUP Oxford, 2000).
100. Baruchel, J., Hodeau, J. L., Lehmann, M. S., Regnard, J. R. & Schlenker, C. *Neutron and Synchrotron Radiation for Condensed Matter Studies: Applications to Solid State Physics and Chemistry*. (Springer Berlin Heidelberg, 2013).
101. Jackson, A. J. Introduction to Small-Angle Neutron Scattering and Neutron Reflectometry. *NIST Cent. Neutron Res.* 1–24 (2008).
102. Grillo, I. Small-Angle Neutron Scattering and Applications in Soft Condensed Matter BT - Soft Matter Characterization. in (eds. Borsali, R. & Pecora, R.) 723–782 (Springer Netherlands, 2008).
103. Cousin, F. Small angle neutron scattering. *EPJ Web Conf.* **104**, (2015).
104. Nele, V. *et al.* Effect of Formulation Method, Lipid Composition, and PEGylation on Vesicle Lamellarity: A Small-Angle Neutron Scattering Study. *Langmuir* **35**, 6064–6074 (2019).
105. Satsoura, D. *et al.* Interaction of the full-length Bax protein with biomimetic mitochondrial liposomes: A small-angle neutron scattering and fluorescence study. *Biochim. Biophys. Acta - Biomembr.* **1818**, 384–401 (2012).
106. Owen, D. J. *et al.* A Structural Explanation for the Binding of Multiple Ligands by the α-Adaptin Appendage Domain. *Cell* **97**, 805–815 (1999).
107. Owen, D. J., Vallis, Y., Pearse, B. M. F., McMahon, H. T. & Evans, P. R. The structure and function of the β2-adaptin appendage domain. *EMBO J.* **19**, 4216–4227 (2000).
108. Zhang, H. Thin-Film Hydration Followed by Extrusion Method for Liposome Preparation BT - Liposomes: Methods and Protocols. in (ed. D'Souza, G. G. M.) 17–22 (Springer New York, 2017).
109. Carrascosa-Tejedor, J., Santamaria, A., Pereira, D. & Maestro, A. Structure of DPPC Monolayers at the Air/Buffer Interface: A Neutron Reflectometry and Ellipsometry Study. *Coatings* **10**, (2020).
110. Jaudzems, K., Polenova, T., Pintacuda, G., Oschkinat, H. & Lesage, A. DNP NMR of biomolecular assemblies. *J. Struct. Biol.* **206**, 90–98 (2019).
111. Bechinger, B. DNP Solid-State NMR of Biological Membranes. *eMagRes* 25–34 (2018).
112. Motschmann, H. & Teppner, R. Ellipsometry in Interface Science. in *Novel Methods*

to Study Interfacial Layers (eds. Möbius, D. & Miller, R. B. T.-S. in I. S.) **11**, 1–42 (Elsevier, 2001).

113. Palik, E. D. *Handbook of Optical Constants of Solids: Volume 1*. (Elsevier Science, 2012).
114. Malitson, I. H. Interspecimen Comparison of the Refractive Index of Fused Silica*,†. *J. Opt. Soc. Am.* **55**, 1205–1209 (1965).
115. Nestler, P. & Helm, C. A. Determination of refractive index and layer thickness of nm-thin films via ellipsometry. *Opt. Express* **25**, 27077–27085 (2017).
116. Kienle, D. F., de Souza, J. V, Watkins, E. B. & Kuhl, T. L. Thickness and refractive index of DPPC and DPPE monolayers by multiple-beam interferometry. *Anal. Bioanal. Chem.* **406**, 4725–4733 (2014).
117. Fischer, A. & Sackmann, E. Electron microscopy and diffraction study of phospholipid monolayers transferred from water to solid substrates. *J. Phys. Fr.* **45**, 517–527 (1984).
118. Cremer, P. S. & Boxer, S. G. Formation and Spreading of Lipid Bilayers on Planar Glass Supports. *J. Phys. Chem. B* **103**, 2554–2559 (1999).
119. Shreve, A. P., Howland, M. C., Sapuri-Butti, A. R., Allen, T. W. & Parikh, A. N. Evidence for Leaflet-Dependent Redistribution of Charged Molecules in Fluid Supported Phospholipid Bilayers. *Langmuir* **24**, 13250–13253 (2008).
120. Bene, M., Billy, D., Hermens, W. T. & Hof, M. Muscovite (Mica) Allows the Characterisation of Supported Bilayers by Ellipsometry and Confocal Fluorescence Correlation Spectroscopy. *Biol. Chem.* **383**, 337–341 (2002).
121. Nieh, M.-P., Kučerka, N. & Katsaras, J. Formation mechanism of self-assembled unilamellar vesiclesSpecial issue on Neutron Scattering in Canada. *Can. J. Phys.* **88**, 735–740 (2010).
122. Salvati, A. *et al.* Small Angle Scattering and Zeta Potential of Liposomes Loaded with Octa(carboranyl)porphyrazine. *J. Phys. Chem. B* **111**, 10357–10364 (2007).
123. Levental, I., Cēbers, A. & Janmey, P. A. Combined Electrostatics and Hydrogen Bonding Determine Intermolecular Interactions Between Polyphosphoinositides. *J. Am. Chem. Soc.* **130**, 9025–9030 (2008).
124. Redfern, D. A. & Gericke, A. pH-dependent domain formation in phosphatidylinositol polyphosphate/phosphatidylcholine mixed vesicles. *J. Lipid Res.* **46**, 504–515 (2005).
125. Carvalho, K., Ramos, L., Roy, C. & Picart, C. Giant Unilamellar Vesicles Containing Phosphatidylinositol(4,5)bisphosphate: Characterization and Functionality. *Biophys. J.* **95**, 4348–4360 (2008).
126. van den Brink-van der Laan, E., Antoinette Killian, J. & de Kruijff, B. Nonbilayer lipids affect peripheral and integral membrane proteins via changes in the lateral pressure profile. *Biochim. Biophys. Acta - Biomembr.* **1666**, 275–288 (2004).
127. Gruner, S. M. Stability of lyotropic phases with curved interfaces. *J. Phys. Chem.* **93**, 7562–7570 (1989).
128. Hardy, G. J., Nayak, R. & Zauscher, S. Model cell membranes: Techniques to form complex biomimetic supported lipid bilayers via vesicle fusion. *Curr. Opin. Colloid Interface Sci.* **18**, 448–458 (2013).
129. Seantier, B. & Kasemo, B. Influence of Mono- And Divalent Ions on the Formation of Supported Phospholipid Bilayers via Vesicle Adsorption. *Langmuir* **25**, 5767–5772

(2009).
130. Rossetti, F. F., Textor, M. & Reviakine, I. Asymmetric Distribution of Phosphatidyl Serine in Supported Phospholipid Bilayers on Titanium Dioxide. *Langmuir* **22**, 3467–3473 (2006).
131. Cho, N.-J., Kanazawa, K. K., Glenn, J. S. & Frank, C. W. Employing Two Different Quartz Crystal Microbalance Models To Study Changes in Viscoelastic Behavior upon Transformation of Lipid Vesicles to a Bilayer on a Gold Surface. *Anal. Chem.* **79**, 7027–7035 (2007).
132. Al-Rekabi, Z. & Contera, S. Multifrequency AFM reveals lipid membrane mechanical properties and the effect of cholesterol in modulating viscoelasticity. *Proc. Natl. Acad. Sci.* **115**, 2658 LP – 2663 (2018).
133. Benga, G. *Structure and properties of cell membranes Volume 3: Methodology and properties of membranes*. (CRC Press Inc, 1985).
134. Grimaldi, N. *et al.* Lipid-based nanovesicles for nanomedicine. *Chem. Soc. Rev.* **45**, 6520–6545 (2016).

7

Appendix

7. Appendix

Appendix A – Thickness of SiO_2 layers and Isotherms of DPPC/DPPE

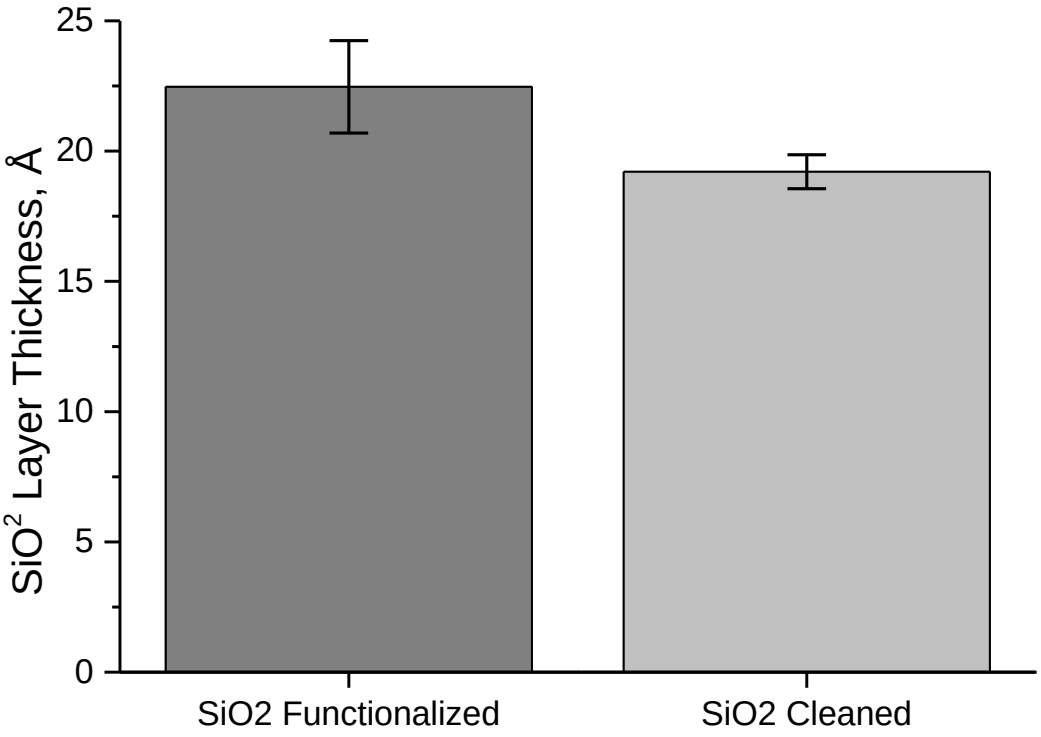

Figure S1: Average thickness of SiO_2 layer present on silicon wafers post-cleaning (shown as light-grey) and post-functionalization (shown as dark-grey).

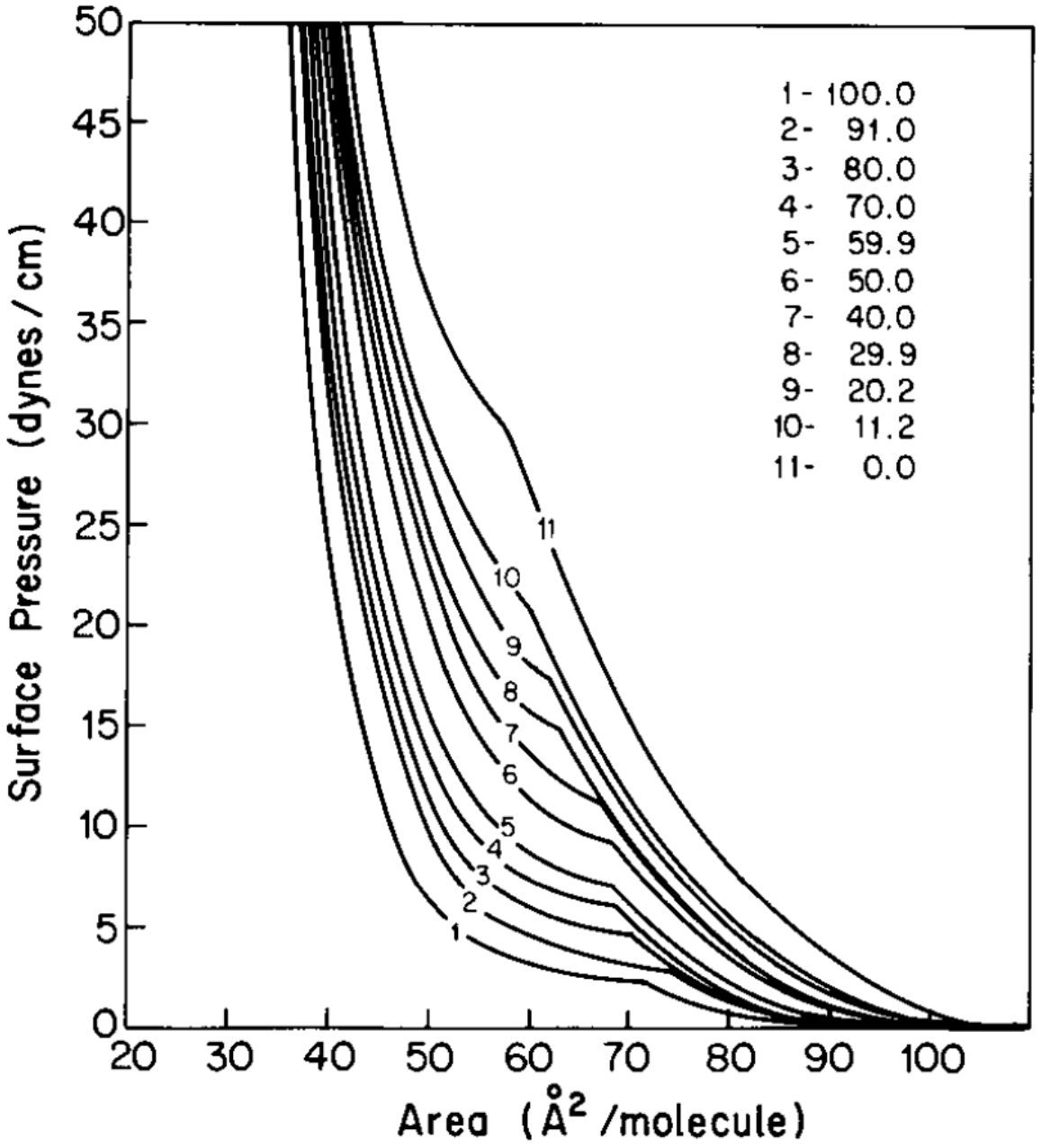

Figure S2: Isotherms of DPPC/DPPE monolayer as a function of molar % of DPPE lipid performed at 37 ºC with water as a pure subphase. Isotherm numbered 11 is relative to a pure DPPC monolayer. Isotherm numbered 9 is relative to a DPPC/DPPE with approximate molar ratio of 8:2. * 1 dyne/cm = 1 mN/m . Image adapted from [133]

Appendix B – Liposome aggregation before SANS analyses

During the formulation of the liposomes, serious aggregation was observed, especially in the liposomes containing PIP2 lipids, as shown in *figure S3A*. The liposome concentration was 1.0 mg/mL, 10-fold higher than the vesicles formulated for QCM-D applications. In order to overcome this issue, the liposome solutions were tip sonicated for 5 minutes and extruded right after. For the extrusion procedure, a two-step procedure was adopted, first, the vesicles were extruded 15x through a 200 nm pore membrane followed by another 25x through a 100 nm pore membrane. After the extrusion cycles, the appearance of the liposome solutions was transparent and no aggregates were observed by naked eye. The DLS profiles of the liposomes were registered and are shown in *figure S3B*, where sample 1 is comprised of DOPC:DOPE (7:3, molar) and sample 2, 3 and 4 is comprised of DOPC:DOPE:PIP2 (7:2:1, molar). The detailed DLS report with size distribution and polydispersity index can be found in *figure S4.*

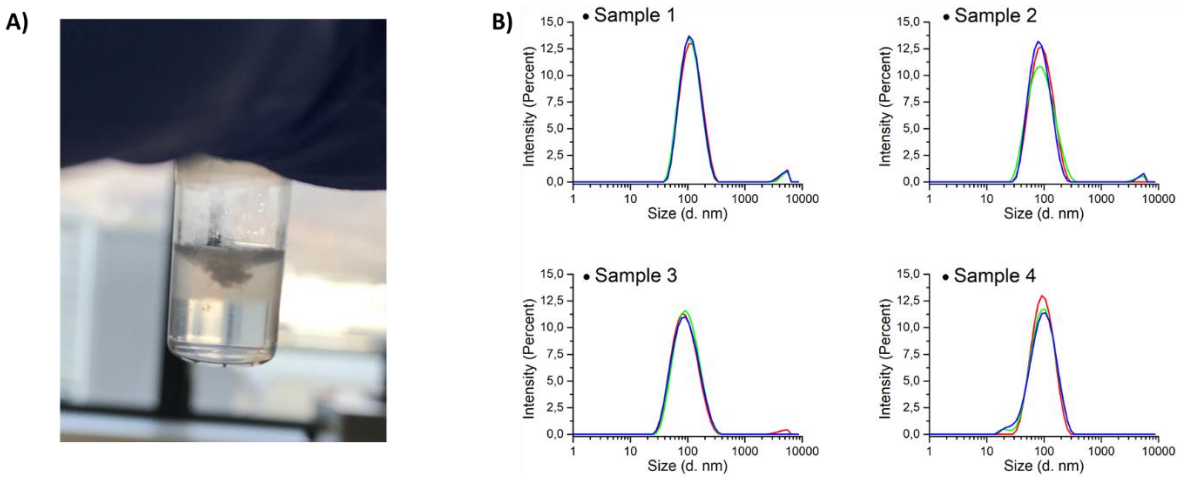

Figure S3: Appearance of the liposome aggregates before-extrusion (A) and DLS profiles after-extrusion (B). The appearance solution changed from milky (A) to transparent after 15x extrusions through 200 nm pore membrane followed by another 25x through a 100 nm pore membrane. The DLS profile of the aliquots of liposome solution used for each sample (B) shows a size distribution ranging ~100 nm of diameter. Curiously, Sample 1, 2 and 3 exhibits a small peak relative to structures with approximately 5000 nm (see *figure S4*), which are likely caused by aggregates that remain in the sample and are difficult to see with the naked eye.

- **Sample 1**

	Size (d. nm):	% Intensity:	St Dev (d. nm)	PdI
Peak 1:	122,0	97,2	49,24	
Peak 2:	4833	2,8	702,3	0,227
Peak 3:	0,000	0,0	0,000	

- **Sample 2**

	Size (d. nm):	% Intensity:	St Dev (d. nm)	PdI
Peak 1:	97,29	100,0	41,66	
Peak 2:	0,000	0,0	0,000	0,189
Peak 3:	0,000	0,0	0,000	

- **Sample 3**

	Size (d. nm):	% Intensity:	St Dev (d. nm)	PdI
Peak 1:	98,77	98,5	48,64	
Peak 2:	4548	1,5	852,7	0,204
Peak 3:	0,000	0,0	0,000	

- **Sample 4**

	Size (d. nm):	% Intensity:	St Dev (d. nm)	PdI
Peak 1:	102,2	100,0	42,45	
Peak 2:	0,000	0,0	0,000	0,175
Peak 3:	0,000	0,0	0,000	

Figure S4: Size and polydispersity index, measured through DLS, of the liposomes aliquots used for SANS experiments, where sample 1 is comprised of DOPC:DOPE (7:3, molar) and sample 2, 3 and 4 is comprised of DOPC:DOPE:PIP2 (7:2:1, molar).

Appendix C – Protocol optimization for QCM-D liposomes formulation

For the production of the SLBs small unilamellar vesicles (SUVs) with size ranging 100 nm were used. The liposome vesicles were produced through the thin film hydration method (*figure S5A*). This method gives rise to multilamellar vesicles (MLVs), however for vesicle fusion applications (described under Section 2.2.2) SUVs are generally used because they tend to yield better performances [57]. The steps to transform MLVs into SUVs are well known and comprise freeze/thaw cycles, extrusion and sonication [134]. To optimize the protocol for the production of the liposome vesicles, each of these steps was performed and monitored by DLS (*figure S5B* and *figure S6*).

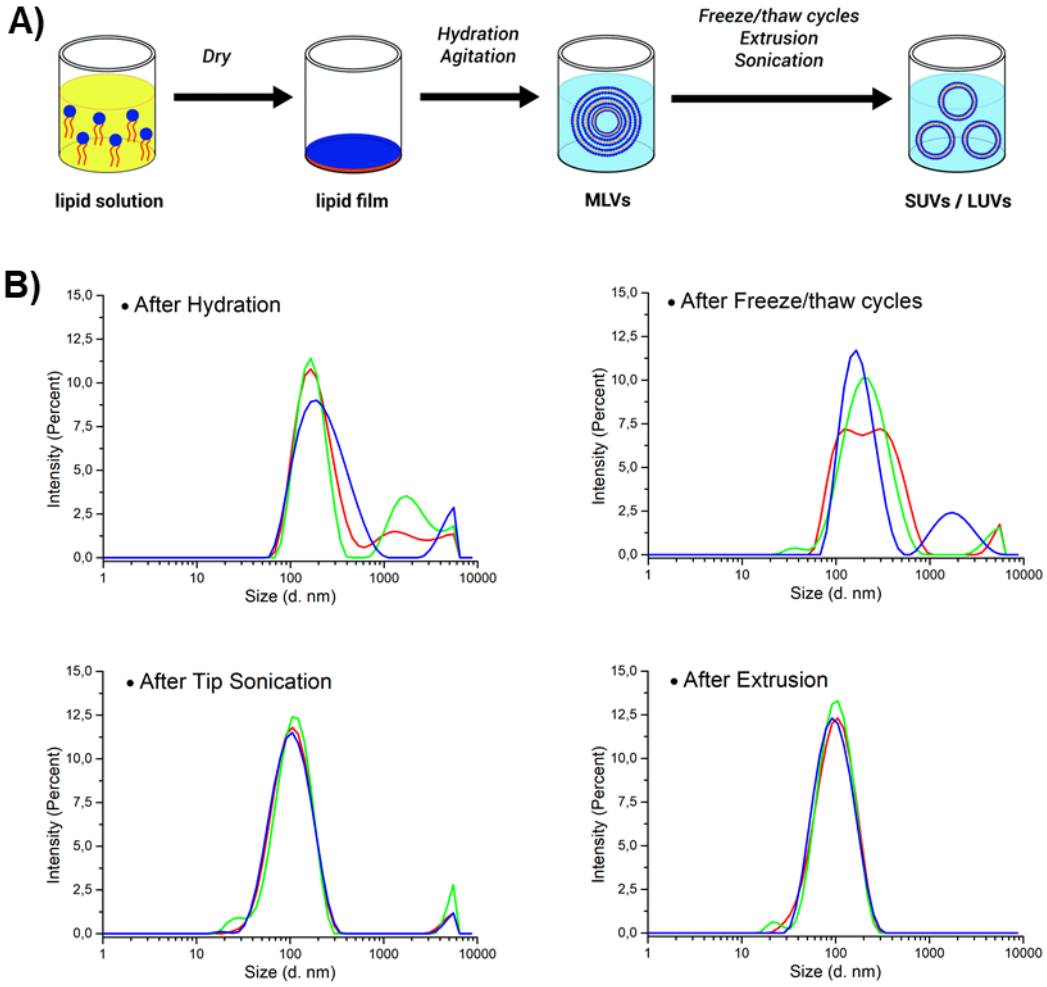

Figure S5: Schematic representation of the thin film hydration method (A) and DLS profile for each step of the transformation of MLVs into SUVs (B). The common steps for the transformation of MLVs into SUVs comprise freeze/thaw cycles, sonication and extrusion. Each of these steps was monitored by DLS for a liposome sample of DOPC:DOPE (8:2, molar). The film was hydrated

overnight (~8 h), submitted to 10 freeze and thaw cycles on liquid nitrogen and ice/water bath, respectively, tip sonicated for 15 min. and extruded 25 times through a 100 nm pore membrane. The DLS profile was recorded immediately after each step. (A) adapted from [134].

The detailed DLS report with size distribution and polydispersity index (PdI) for each of the steps shown in *figure S5B* can be found in *figure S6*. As expected, after hydration the overall size distribution is very broad and far from homogenous, with an overall PdI of 0.359. Curiously, the freeze/thaw cycles shown very tender effects in the overall size distribution of the vesicles. On the other hand, tip sonication shown high effect on the overall size distribution of the vesicles, dramatically reducing the vesicles with higher sizes (>200 nm) and producing a vesicle population with an overall PdI of 0.241. Still, after tip sonication, it was observed the coexistence of two distinct peaks corresponding to sizes of approximately 112 and 4812 nm. However, after 25 extrusion cycles through a 100 nm pored membrane the overall size distribution and PdI correspond to a monodisperse vesicle solution comprised of SUVs, with size of approximately 106 nm and a PdI of 0.163.

The protocol for the production of the vesicles was optimized based on the DLS profiles shown in *figure S5* and *S6*. The thin film hydration method protocol was followed as presented in *figure S5A* and the steps to transform MLVs into SUVs were optimized by excluding the freeze/thaw cycles. Adding to the fact that the freeze/thaw cycles shown minor effects in the overall size population and PdI, this step is generally very time consuming. Thus, only the tip sonication and extrusion steps were performed for producing the SUVs. This rationale was used to produce all the liposome vesicles used in QCM-D studies, presented and discussed in the Section 4.3. In general, these steps were able to produce similar results with different formulation of liposomes. As a troubleshoot, prior to any QCM-D experiment the liposome vesicles were monitored by DLS and if the size or the PdI was not identical to the ones shown here (DLS profile entitled “After Extrusion”), more extrusion cycles were performed until the desirable values were observed.

- **After Hydration**

	Size (d. nm):	% Intensity:	St Dev (d. nm)	PdI
Peak 1:	195,6	80,8	92,95	
Peak 2:	1466	12,4	593,6	0.359
Peak 3:	4090	6,8	996,8	

- **After Freeze/Thaw cycles**

	Size (d. nm):	% Intensity:	St Dev (d. nm)	PdI
Peak 1:	353,6	52,8	144,0	
Peak 2:	128,7	44	37,65	0,354
Peak 3:	5042	3,3	586,2	

- **After Tip Sonication**

	Size (d. nm):	% Intensity:	St Dev (d. nm)	PdI
Peak 1:	112,5	97,0	50,34	
Peak 2:	4812	3,0	718,4	0,241
Peak 3:	0,000	0,0	0,000	

- **After Extrusion**

	Size (d. nm):	% Intensity:	St Dev (d. nm)	PdI
Peak 1:	**106,6**	100,0	46,96	
Peak 2:	0,000	0,0	0,000	**0,163**
Peak 3:	0,000	0,0	0,000	

Figure S6: Size and polydispersity index, measured through DLS, for each step carried to transform MLVs into SUVs. The ideal values, obtained after extrusion, are shown in bold green.

Appendix D – Parameters fitted for Section A and Section B

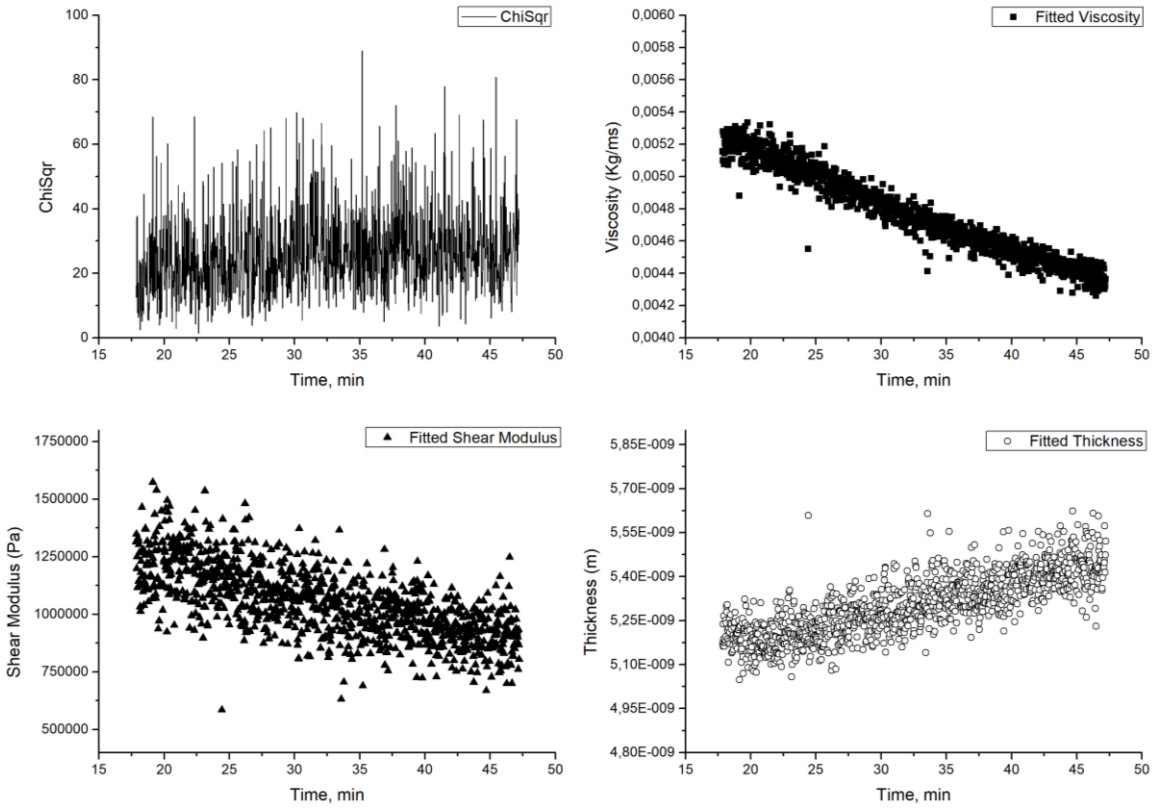

Figure S7: Fitted parameters for the SLB zone identified as Section A. The Section A is relative to the formation of the bilayer before performing the buffer wash step. The returned parameters exhibit a trend which highlight that these parameters are still evolving and therefore the overall structure of the SLB is not stabilized yet.

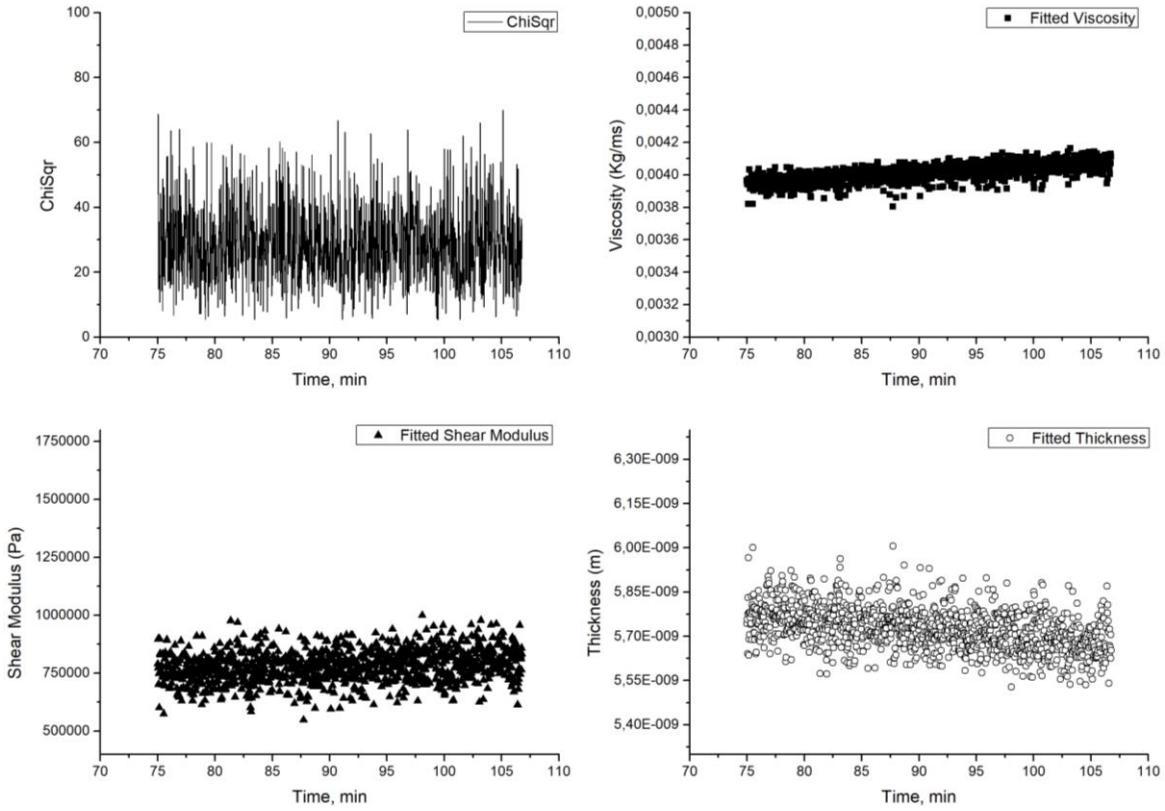

Figure S8: Fitted parameters for the SLB zone identified as Section B. The Section B is relative to the formation of the bilayer after performing the buffer wash step. The returned parameters exhibit a trend which highlight that these parameters are not evolving and therefore the overall structure of the SLB is stabilized.

Appendix E – QCM-D profile of liposomes formulated with TGN38 and PIP2

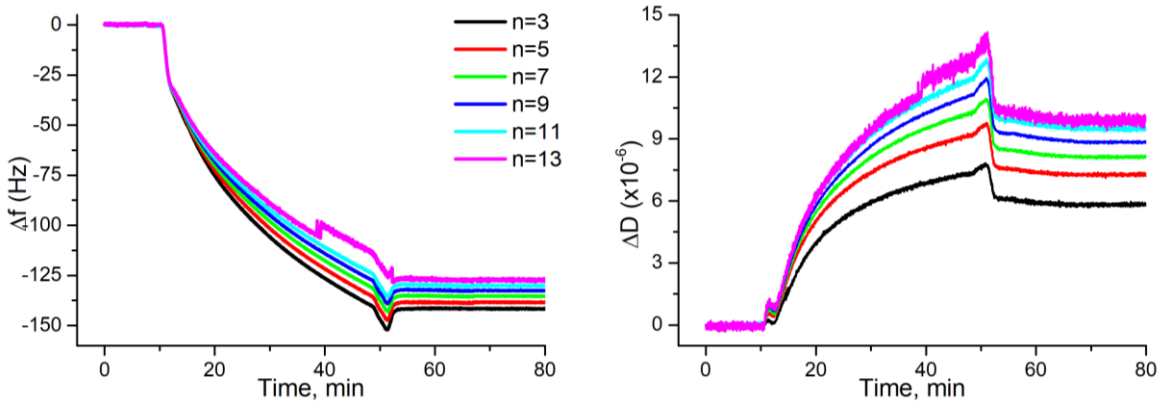

Figure S9: Monitored Δf and ΔD over time for liposomes containing both PIP2-lipids and TGN38. The high values observed for ΔD and frequency decrease are indicative of vesicle adsorption to the surface of the QCM-D sensor. Contrary to the behaviour of vesicles formulated with different components, these liposomes did not rupture and fuse with the sensor.